

AFWL-TR-75-342, Vol. I

2
J. Na
AFWL-TR-
75-342
Vol. I

AD A032453



LASER BEAM TARGET INTERACTION

Volume I

2.8 Microns Wavelength

The Boeing Company
Seattle, WA 98124

July 1976

Final Report



Approved for public release; distribution unlimited.

Prepared for

ADVANCED RESEARCH PROJECTS AGENCY
1400 Wilson Blvd.
Arlington, VA 22209

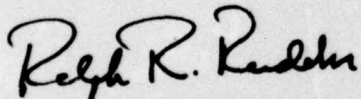
AIR FORCE WEAPONS LABORATORY
Air Force Systems Command
Kirtland Air Force Base, NM 87117

This final report was prepared by The Boeing Company, Seattle, Washington, under Contract F29601-73-A-0038-0002, Job Order 19051006, with the Air Force Weapons Laboratory, Kirtland Air Force Base, New Mexico. Dr. Ralph R. Rudder (PGV) was the Laboratory Project Officer-in-Charge.

When US Government drawings, specifications, or other data are used for any purpose other than a definitely related Government procurement operation, the Government thereby incurs no responsibility nor any obligation whatsoever, and the fact that the Government may have formulated, furnished, or in any way supplied the said drawings, specifications, or other data, is not to be regarded by implication or otherwise, as in any manner licensing the holder or any other person or corporation, or conveying any rights or permission to manufacture, use, or sell any patented invention that may in any way be related thereto.

This report has been reviewed by the Information Office (OI) and is releasable to the National Technical Information Service (NTIS). At NTIS, it will be available to the general public, including foreign nations.

This technical report has been reviewed and is approved for publication.

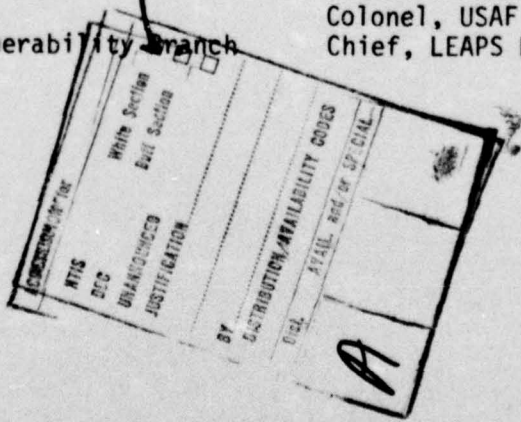


RALPH R. RUDDER
Project Officer

FOR THE COMMANDER

for *David Evans Cpt USAF*
HECTOR REDE
Major, USAF
Chief, Effects and Vulnerability Branch

James H. Bernasconi
LOUIS H. BERNASCONI
Colonel, USAF
Chief, LEAPS Division



DO NOT RETURN THIS COPY. RETAIN OR DESTROY.

UNCLASSIFIED

SECURITY CLASSIFICATION OF THIS PAGE (When Data Entered)

REPORT DOCUMENTATION PAGE		READ INSTRUCTIONS BEFORE COMPLETING FORM
1. REPORT NUMBER AFWL-TR-75-342, Vol. I	2. GOVT ACCESSION NO.	3. RECIPIENT'S CATALOG NUMBER
4. TITLE (and Subtitle) LASER BEAM TARGET INTERACTION : Volume I. 2.8 Microns Wavelength,		5. TYPE OF REPORT & PERIOD COVERED Final Report, 31 Mar '74 - 15 Jun '76,
6. AUTHOR R. B. Hall, W. E. Maher, J. D. McClure, D. B. Nichols, C. R. Pond		7. CONTRACT OR GRANT NUMBER F29601-73-A-0038-0002, ARPA Order-1905
8. PERFORMING ORGANIZATION NAME AND ADDRESS The Boeing Aerospace Company P. O. Box 3999 Seattle, WA 98124		9. PROGRAM ELEMENT, PROJECT, TASK AREA & WORK UNIT NUMBERS 62301E 19051006
10. CONTROLLING OFFICE NAME AND ADDRESS Advanced Research Projects Agency 1400 Wilson Blvd. Arlington, VA 22209		11. REPORT DATE Jul 1976
12. MONITORING AGENCY NAME & ADDRESS(if different from Controlling Office) Air Force Weapons Laboratory (PGV) Kirtland Air Force Base, NM 87117		13. NUMBER OF PAGES 114
14. DISTRIBUTION STATEMENT (of this Report) Approved for public release; distribution unlimited.		15. SECURITY CLASS. (of this report) UNCLASSIFIED
16. DISTRIBUTION STATEMENT (of the abstract entered in Block 20, if different from Report) D180-19256-1		17. DECLASSIFICATION/DOWNGRADING SCHEDULE 1905 / 10 /
18. SUPPLEMENTARY NOTES		
19. KEY WORDS (Continue on reverse side if necessary and identify by block number) Laser Beam Target Interaction Spectroscopic and interferometric diagnostics HF chemical laser Plasma ignition Beam intensities LSD waves Target plasmas		
20. ABSTRACT (Continue on reverse side if necessary and identify by block number) This report is the first of two volumes on the subject of Laser Beam Target Interaction. Laser beam-target interactions for solid surfaces have been investigated at 2.8 microns wavelength with a 150 J photoinitiated pulsed HF chemical laser. Laser-supported detonation wave propagation was studied at beam intensities up to 160 MW/cm ² . Information about target plasmas was obtained by means of spectroscopic and interferometric diagnostics. Ignition thresholds for laser-supported absorption waves were measured both by (over)		

UNCLASSIFIED

SECURITY CLASSIFICATION OF THIS PAGE(When Data Entered)

ABSTRACT (cont'd)

observation of plasma luminosity and by measuring the laser power transmitted through a small hole in the target. Measurements were made of thermal and impulse coupling occurring under plasma ignition conditions.

UNCLASSIFIED

SECURITY CLASSIFICATION OF THIS PAGE(When Data Entered)

Preface

This report was prepared by the Boeing Aerospace Company under Contract F29601-73-A-0038-0002. The research was performed under Project F29601-74-10066, and was funded by the Advanced Research Projects Agency under ARPA Order 1905.

Inclusive dates of research were March 31, 1974 to January 15, 1976.

The authors wish to thank the following for their advice and assistance: L. Alexander, D. Botz, D. J. Nelson, P.S.P. Wei, and C. Wachupe.

The contractor report number is D180-19256-1.

CONTENTS

Section	Page
I. INTRODUCTION	1
1. Objective	1
2. Approach	1
II. THE PULSED HF CHEMICAL LASER	2
1. Background	2
2. Experimental Method	2
3. Intensity Time Profile	4
4. Parameter Variation	12
5. Far Field Beam Profile	14
6. Beam Divergence	14
7. Repeatability	14
8. Laser Efficiencies	16
9. Beam Attenuation	16
10. Holographic Spectroscopy	21
11. Wet-Air Absorption	25
III. PULSED HF CHEMICAL LASER EFFECTS	28
1. LSD Wave Propagation Studies	28
a. Analytic Approximations to the Focal Energy Distribution and the Power-Time Dependence	28
b. Propagation of Laser-Supported Detonation (LSD) Waves	33
2. Spectroscopic Diagnostics of Laser-Supported Absorption Waves at 2.8 Microns	43
3. Ignition Thresholds for LSA Waves Produced by HF Laser Radiation	49
4. Impulse Measurements with HF Laser Radiation	58
a. Impulse Produced on Metal Targets	61
b. Impulse Production with Insulator Targets	65
5. Thermal Coupling of Pulsed 2.8 Micron Radiation to Metal Targets	65
6. Interferometric Diagnostics of Effects Produced by HF Laser Radiation	70
a. Experimental Layout	72
b. Ruby Laser Shadowgraphs and Interferometry	76
c. Interpretation of Interferograms	89
Summary	101
References	102

ILLUSTRATIONS

Figure	Page
1 Diagram of Principal HF Laser Components	3
2 Diagram of the Photo-Initiated HF Laser. Half of the Symmetric Mechanical Assembly is Shown; The Other End Includes the Optical Output Coupler	5
3 View of Pulsed Chemical Laser Inside the Hood Room	6
4 Control Area for Pulsed Chemical Laser	7
5 Gas Handling Area Including Gas Supplies, Gas Mixing Apparatus Vacuum Equipment, and Ballast Tank	8
6 Pulsed Chemical Laser Effects Target Room. Mach-Zehnder Interferometer is in Place, with Q-Switched Ruby Laser and Power Supplies	9
7 Floor Plan for HF Pulsed Chemical Laser Effects Laboratory. Beam Folding Mirror (In Beam Enclosure 19) Directs the Beam Into the Laser Effects Area	10
8 Time relationships between (1) the Current Profile for a 30 kV Discharge Through a Flashlamp, (2) the Associated UV Time Profile, and (3) the Resulting HF Laser Output Pulse	11
9 Far Field Beam Profiles Measured with an Apertured Calori- meter in the Focal Plane of an $f = 164$ cm Mirror	15
10 Absolute Magnitude of Laser Energy on a Target 5.7 Meters from the Laser, for Several Sequential Shots in Which H_2-F_2 Mixing was Done at Room Temperature	17
11 Schematic Diagram of Laboratory Optical Arrangement	20
12 HF Laser Beam Attenuation Curves Showing Availability of Laser Pulsed in the Range 0-75% of Full Energy Using Teflon Sheets or Metal Screening at Various Transmission Angles	22
13 Hologram Recording Setup	23
14 Hologram Reconstruction Setup	24
15 Second Order Spectrum from a 1 cm^2 Hologram. Sample Situated 3 cm From the HF Laser Axis	26
16 "Exact" and Approximate Pulsed Chemical Laser Pulse Shape	29
17 Analytic Fit to Far-Field HF Laser Beam Profile	31
18 Framing Camera Data Showing the Progression of an LSD Wave at 0.5 μsec Intervals from an Aluminum Surface	34

19	Laser Supported Detonation Wave Position as a Function of Time for $0 < t < 4.56 \mu\text{sec}$	37
20	Streak Photograph of the First 4 μsec of an LSD Wave Formed by a 64-J HF Laser Pulse Focussed to 0.4 cm Diameter spot on Aluminum 6061 Alloy	40
21	HF Laser Pulse Amplitude, and LSD Wave Front Position, Plotted on the Same Time Scale.	41
22	Six Framing Camera Images Taken at 0.5 μsec Intervals, Using Two Separate Laser Shots. The Plasma is Viewed Along the Beam Direction to Show Radial Development of LSD Waves. Oscillograms Show Framing Camera Image Times Relative to Laser Pulse Time Profile	42
23	Sections of the Emission Spectra Observed at 4mm in Front of an Al-Plate Target. The HF Laser Total Target Energy is Indicated in the Parentheses	44
24	The LSA Wave Continuum Emission Observed at Several Distances in Front of the Target. The Arrows Designate the Onset of Light. A Laser Pulse Shape is Included for Comparison	45
25	A Correlation of the Distance and Time for the LSA Wave-front. An Average Speed is Obtained from the Slope of a Straight-Line Fit	47
26	Temporal Behavior of Four Kinds of Emission Lines from the Plasma Produced by a 45-J Pulse from an Al-Plate	48
27	Time Profile for HF Laser Pulse Transmitted Through a Stainless 321 Target Pinhole (Upper) Compared to the Complete Laser Pulse (Lower). For this Case Pinhole Transmission was Cut Off when the Integrated Fluence Reached 82% of the 46 J/cm^2 Total	51
28	I/E Values Shown as a Function of Target Diameter for Aluminum at 2.8μ	62
29	I/E Values Shown as a Function of Target Diameter for Titanium at 2.8μ	63
30	I/E Values Shown as a Function of Target Diameter for 304 Stainless Steel at 2.8μ	64
31	I/E Values Shown as a Function of Target Diameter for Lexan at 2.8μ	66

32	I/E Values Shown as a Function of Target Diameter for Lucite at 2.8 μ	67
33	Thermal Coupling Coefficient as a Function of HF Laser Beam Energy for 1.6 cm Diameter Titanium Targets. A New Target Was Used for Each Data Point. Beam Spot Area Was 0.20 cm^2 .	69
34	Thermal Coupling Coefficient as a Function of HF Laser Beam Energy for 1.6 cm Diameter Aluminum 6061 Alloy Targets. A New Target was Used for Each Data Point. The Fluence and Irradiance Scales Assume a Uniform Beam Spot Area of 0.20 cm^2 and 3.2 usec FWHM Laser Pulse	71
35	Schematic Diagram of Ruby Interferometer Setup	73
36	Photograph of Mach-Zehnder Interferometer Used to Study LSD Waves	74
37	Schematic Diagram of Circuitry Used to Make Interferograms	75
38	Shadowgrams of LSD Waves Ignited from a Large Target	77
39	Shadowgrams of LSD Waves	78
40	Interferograms of LSD Waves	80
41	Interferograms of LSD Waves	81
42	Interferograms of LSD Waves	82
43	Shadowgraphs of Propagating Laser-Supported Detonation Waves. $E_{inc} = 49.8$ Joules, Target is 6061 Aluminum	83
44	Shadowgraphs of HF-LSD Waves. Target is 6061 Aluminum	84
45	Shadowgraphs of HF-LSD Waves. Target is 6061 Aluminum	85
46	Interferograms of Laser Interaction with Ablators. $E_{inc} = 48.5$ Joules	87
47	Interferograms of Laser-Produced Blast Wave. $E_{inc} = 55.4$ Joules	88
48	Fringe Shift as a Function of Radius	90
49	Refractivity of Laser-Produced Blast Wave	91
50	Abel Inversion of Linearly Modified Fringe Data	93
51	Enlarged View of Boundary Region of Interferogram of Figure 47	96
52	Analytical Fit of Fringe Shift Data to Square Root Dependence. First Two Data Points Excluded. Average Error of Original Data is 4.42 Fringes	97
53	"Square-Root" Modified Fringe Shift Data for HF-LSD Wave	98
54	Computed Density Profiles of Laser Produced Blast Waves	99

TABLES

<u>Table</u>		<u>Page</u>
1 Variation of Laser Output as a Function of Laser Conditions.		13
2 Variation of Laser Energy out as a Function of Energy Stored in the Flashlamp Capacitor Bank.		18
3 Luminosity Thresholds for Ignition of LSA Waves on Aluminum		52
4 Large Spot Pinhole Transmission Thresholds for Ignition of LSA Waves on Three Metals		53
5 Small Spot Pinhole Transmission Thresholds for Ignition of LSA Waves		54
6 LSA Ignition Thresholds for Three Nonmetals		55
7 Comparison of Threshold Values of Laser Pulse Peak Irradiance q_p for 2.8 Micron and 10.6 Micron Radiation		59
8 Comparison of Threshold Values of Laser Pulse Total Fluence e_t for 2.8 Micron and 10.6 Micron Radiation.		60
9 Original Fringe Shift Data as a Function of Radius. $z = 1.44$ cm.		95
10 Blast Wave Radius Versus Density Ratio		100

SECTION I INTRODUCTION

1. OBJECTIVE

A large number of previous studies has shown that the ignition of plasmas and laser-supported absorption waves can have very important consequences for the coupling of energy to the target surface. These plasmas absorb the incident laser energy and diverge the beam path in much the same way as a lens. This work was undertaken to examine 2.8 micron wavelength laser effects in the irradiance region where plasmas are ignited. One of the important objectives was a comparison with previous studies at other wavelengths.

2. APPROACH

A pulsed HF chemical laser was constructed and used in a series of laser effects studies. A discussion of the design, construction, physical layout, and operation of the pulsed chemical laser is given in Section II. The energy density profile at the focus of a mirror was measured and a determination of the pulse shape was made. This HF laser produced up to 152 joules of energy in a 4 usec pulse, however, typical effects experiments used about 40 joules. A holographic spectroscopic technique provided a determination of the actual lines present in the pulsed HF laser output. Laser effects experiments performed using the pulsed HF laser are considered in Section III. These experiments include measurements made with an image converter camera of properties of laser-supported detonation (LSD) waves. Additional experiments include spectroscopic measurements of the properties of these LSD waves. Data are also presented showing plasma ignition thresholds, impulse coupling as measured with a linear velocity transducer (LVT), and thermal coupling results. An interferometer was used to obtain interferograms and shadowgrams of LSD waves and other laser-produced events. An analysis of some of these is presented.

SECTION II

THE PULSED HF CHEMICAL LASER

1. BACKGROUND

Several methods for initiating HF pulsed chemical lasers have been under study recently. For lasers fueled by F_2 , the initiating fluorine dissociation has been accomplished by electric pin-discharge (Ref. 1), electric discharges with UV preionization, (Ref. 2), electric discharges with electron beam preconditioning, (Ref. 3), direct e-beam dissociation, (Ref. 4), and flashlamp photolysis, (Ref. 5,6). In addition, frequency-doubled ruby laser initiation has also been used (Ref. 7,8). A continuing interest has been shown in extending several of these schemes to larger devices. In this section, energy and beam quality measurements obtained from a 10-liter device are presented. This laser, which has produced larger output energies than other previously reported photoinitiated HF lasers, was used in a series of laser effects measurements at 2.8 micron wavelength.

2. EXPERIMENTAL METHOD

Figure 1 shows the major components of the facility comprising a flashlamp discharge capacitor bank, the gas mixing apparatus, and the laser assembly which is shown in some mechanical detail. Figure 2 is a simplified schematic of the photo-initiated HF laser, which is generally characterized by (1) a carefully designed gas mixer and mixing procedure, (2) a transverse path for photolysing UV flashlamp radiation of about 9 cm, and (3) isolation of optical cavity components by an inert buffer gas.

The contact time between H_2 and F_2 , and hence prereaction, is minimized by mixing the gases during the time they are being loaded into the reactor; the filling procedure takes about 30 seconds. Gas mixture composition is defined by needle valves and mass flow meters, and all gas flow is controlled remotely. Fluorine is supplied and stored as a 10% mixture, diluted in the present case with nitrogen. Further diluent and oxygen are added and allowed to mix completely with the fluorine

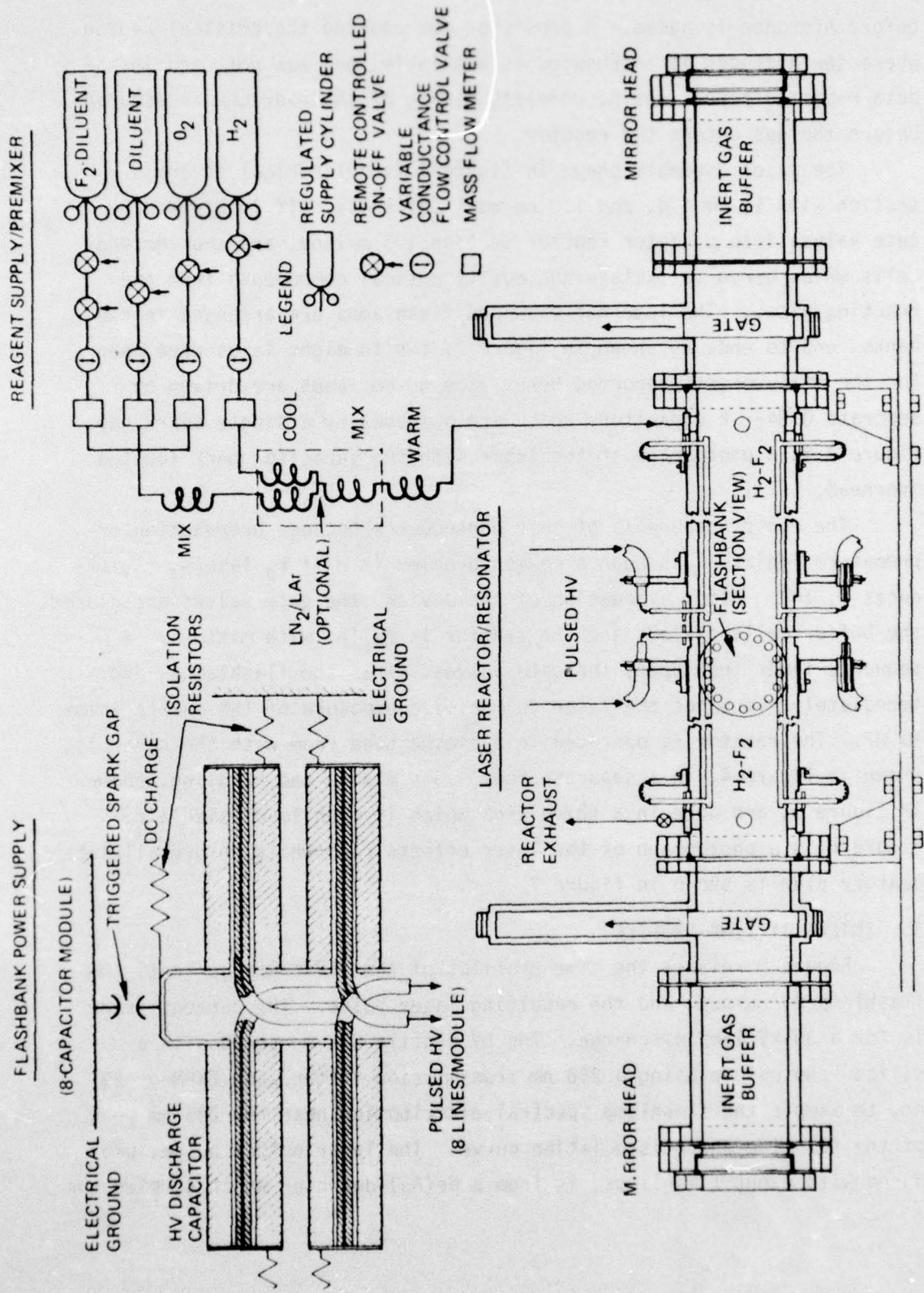


Figure 1. Diagram of Principal HF Laser Components

before hydrogen is added. A provision for cooling the critical region where the hydrogen is introduced is available, but was not used in the data reported here. Again, complete mixing of the hydrogen is assured before the gas enters the reactor.

The laser assembly shown in figure 2 is cylindrical in cross section with 14 cm i.d. and 1.0 cm wall thickness. It is divided by gate valves into a center reactor section 1.5 m long, and shorter end cells which serve to isolate the cavity optical components from the reacting gases. The internal U-shaped flashlamps are arranged in two banks, end to end, as shown in figure 2; two to eight lamps were used for the measurements reported here. The 60-cm lamps are driven by separate 0.84- μ F capacitors which are switched by a single spark gap. Figure 3 is a photograph of the laser with the capacitor bank located overhead.

The run procedure is of some consequence because prereaction or premature ignition has been a common problem in $H_2 + F_2$ lasers, (References 9, 10). After evacuation of the device, the gate valves are closed, the buffer cells filled, and the reactor is filled with mixture. A sequence timer then opens the gate valves, fires the flashlamps, and immediately evacuates the laser to minimize exposure of the quartz lamps to HF. The reactor is operated in a closed hood room with the controls, shown in figure 4, in a separate room. Gas mixing and handling, shown in figure 5, are done in a third area which is open to outside air. Figure 6 is a photograph of the laser effects room while an overall laboratory plan is shown in figure 7.

3. INTENSITY TIME PROFILE

Figure 8 relates the time profiles of the flashlamp current, the flashlamp UV output, and the resulting laser pulse. The current trace is for a 30-kV lamp discharge. The UV profile was measured with a silicon photodiode using a 288 nm transmission filter with FWHM of 23 nm, to sample the flashlamp spectral distribution near the 285 nm peak of the fluorine photodissociation curve. The laser output pulse, produced with eight flashlamps, is from a Ge(Au) detector which samples the

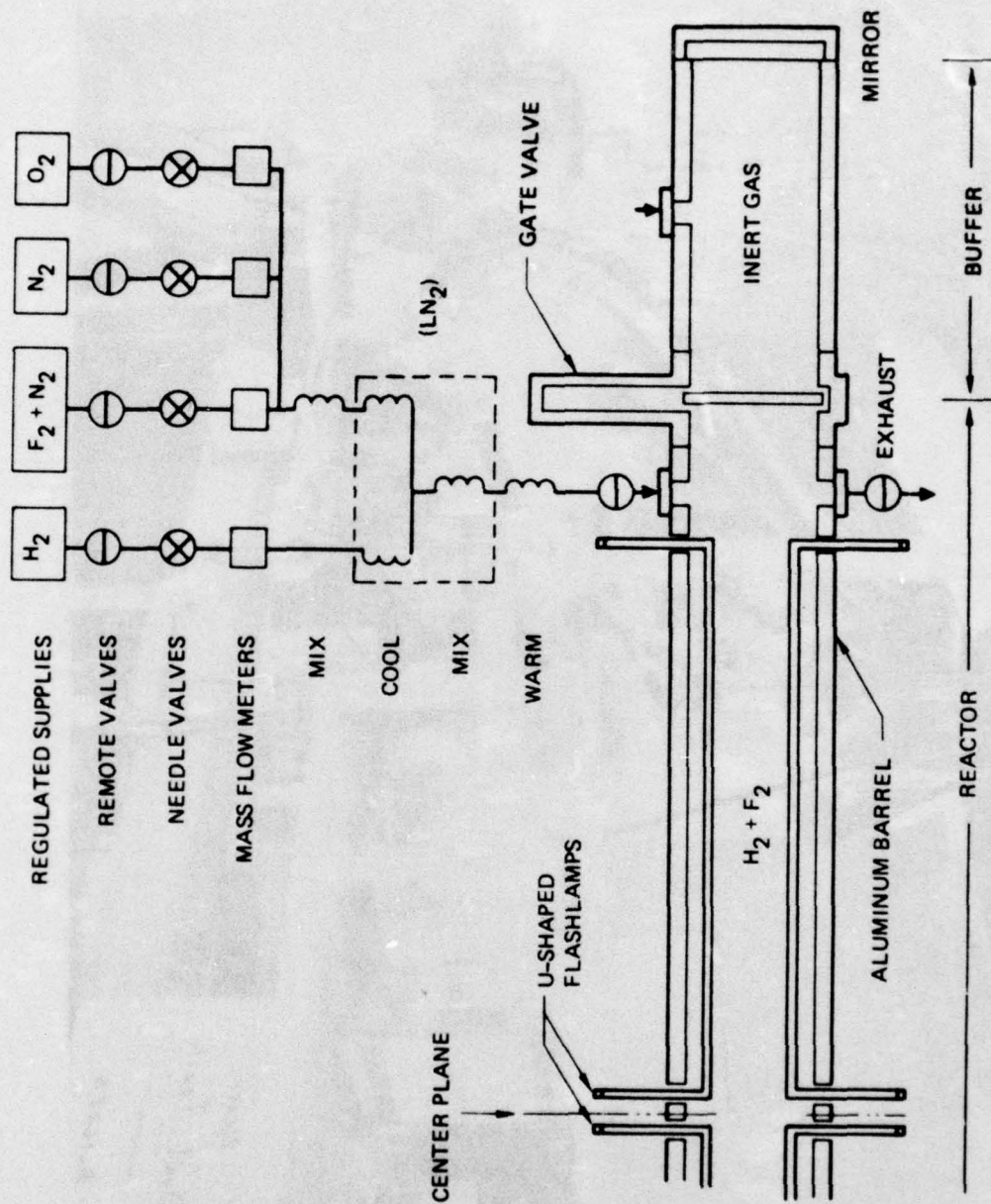


Figure 2. Diagram of the Photo-Initiated HF Laser.
Half of the Symmetric Mechanical Assembly is Shown:
The Other End Includes The Optical Output Coupler

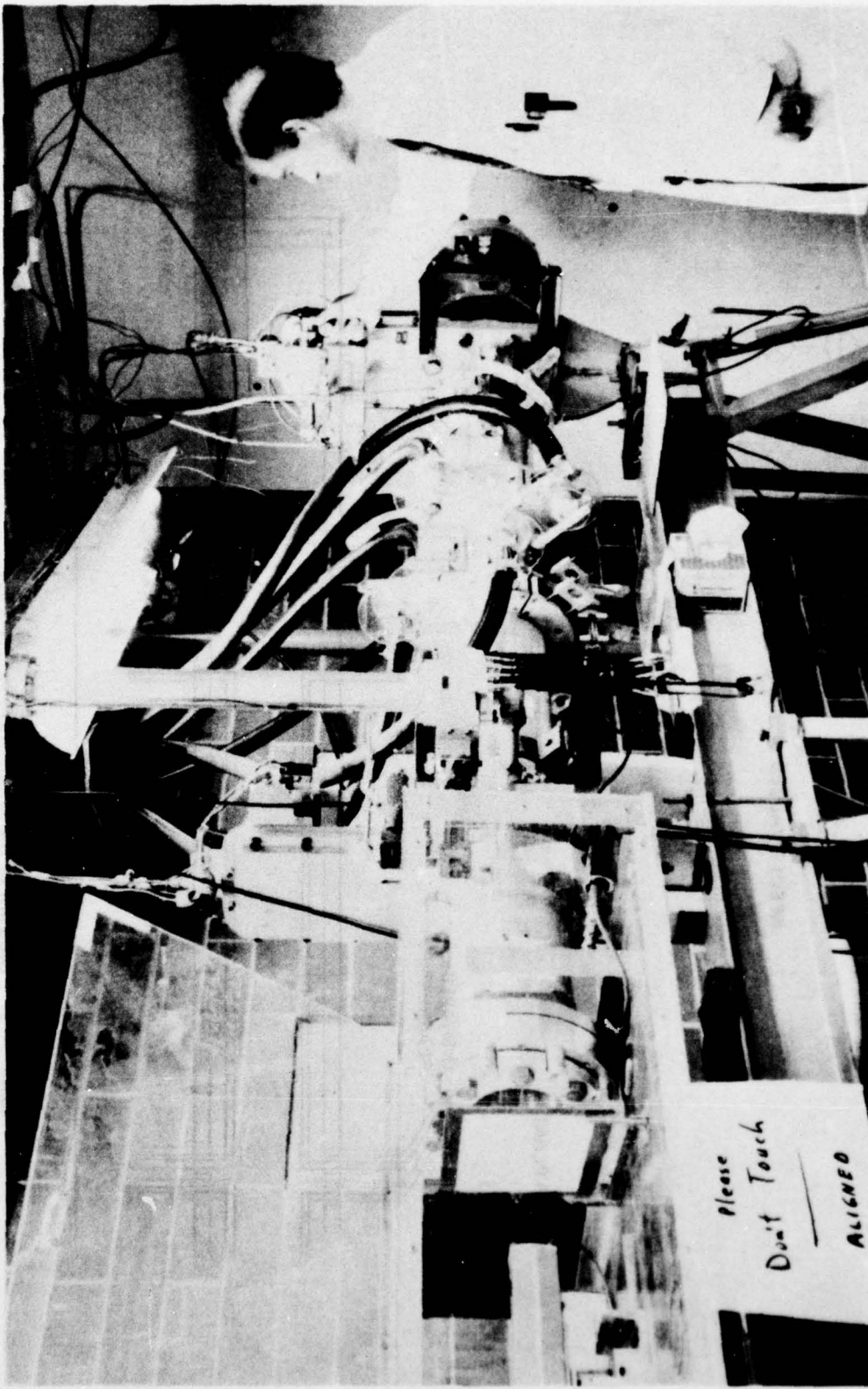


Figure 3 View of Pulsed Chemical Laser Inside the Hood Room

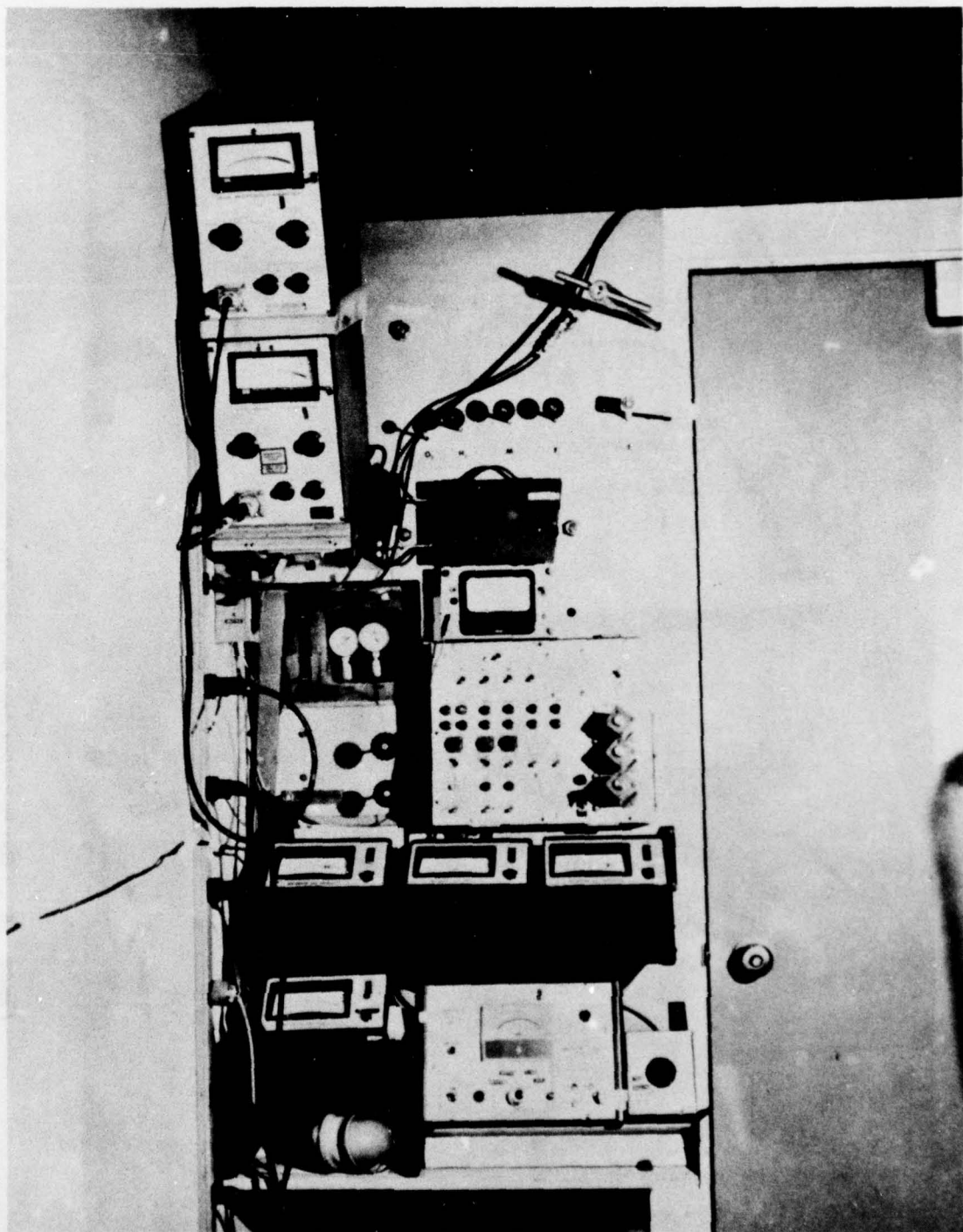


Figure 4 Control Area for Pulsed Chemical Laser

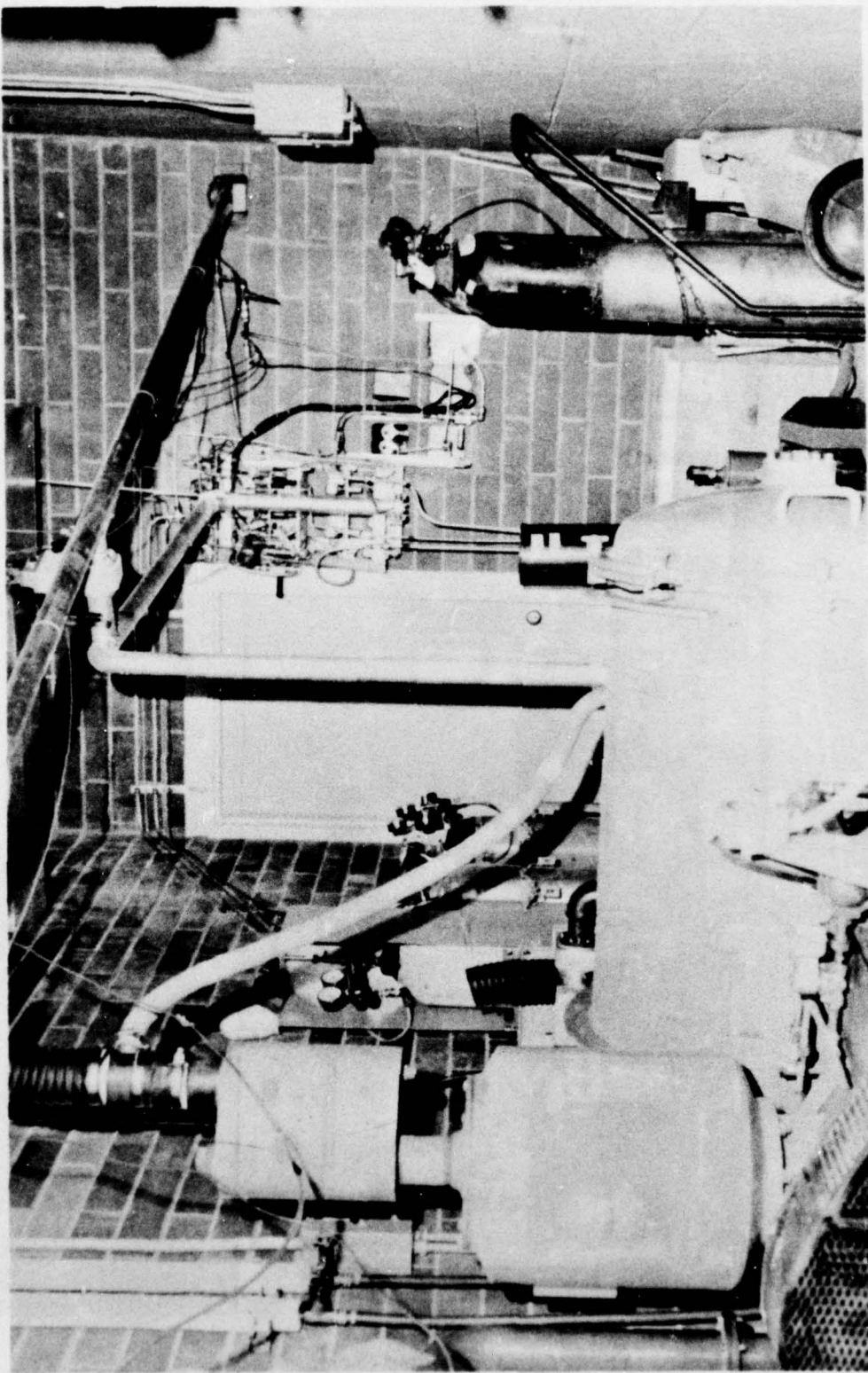
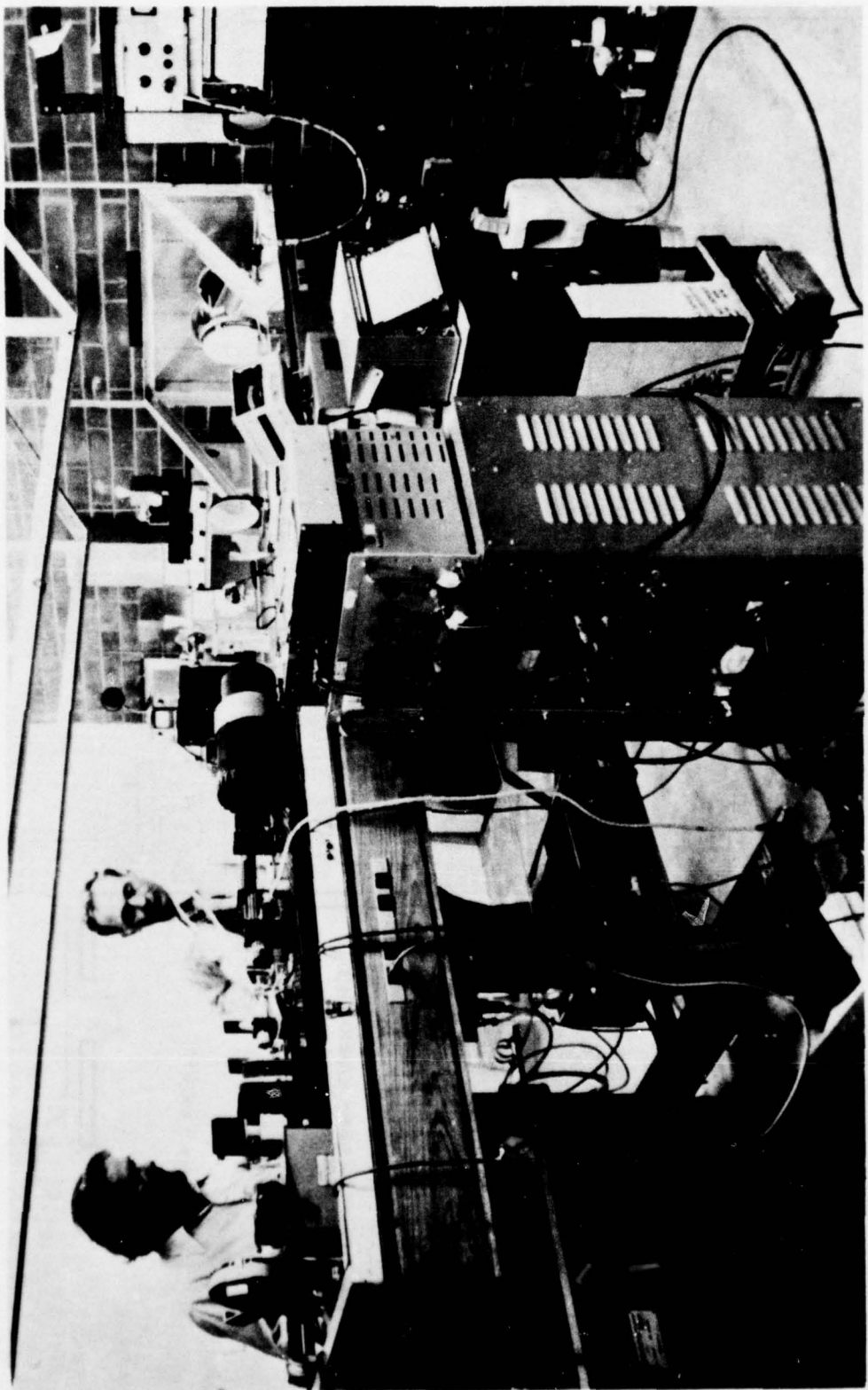


Figure 5 . Gas Handling Area Including Gas Supplies, Gas Mixing Apparatus, Vacuum Equipment, and Ballast Tank

Figure 6 . Pulsed Chemical Laser Effects Target Room.
Mach-Zehnder Interferometer is in Place, With
Q-Switched Ruby Laser and Power Supplies



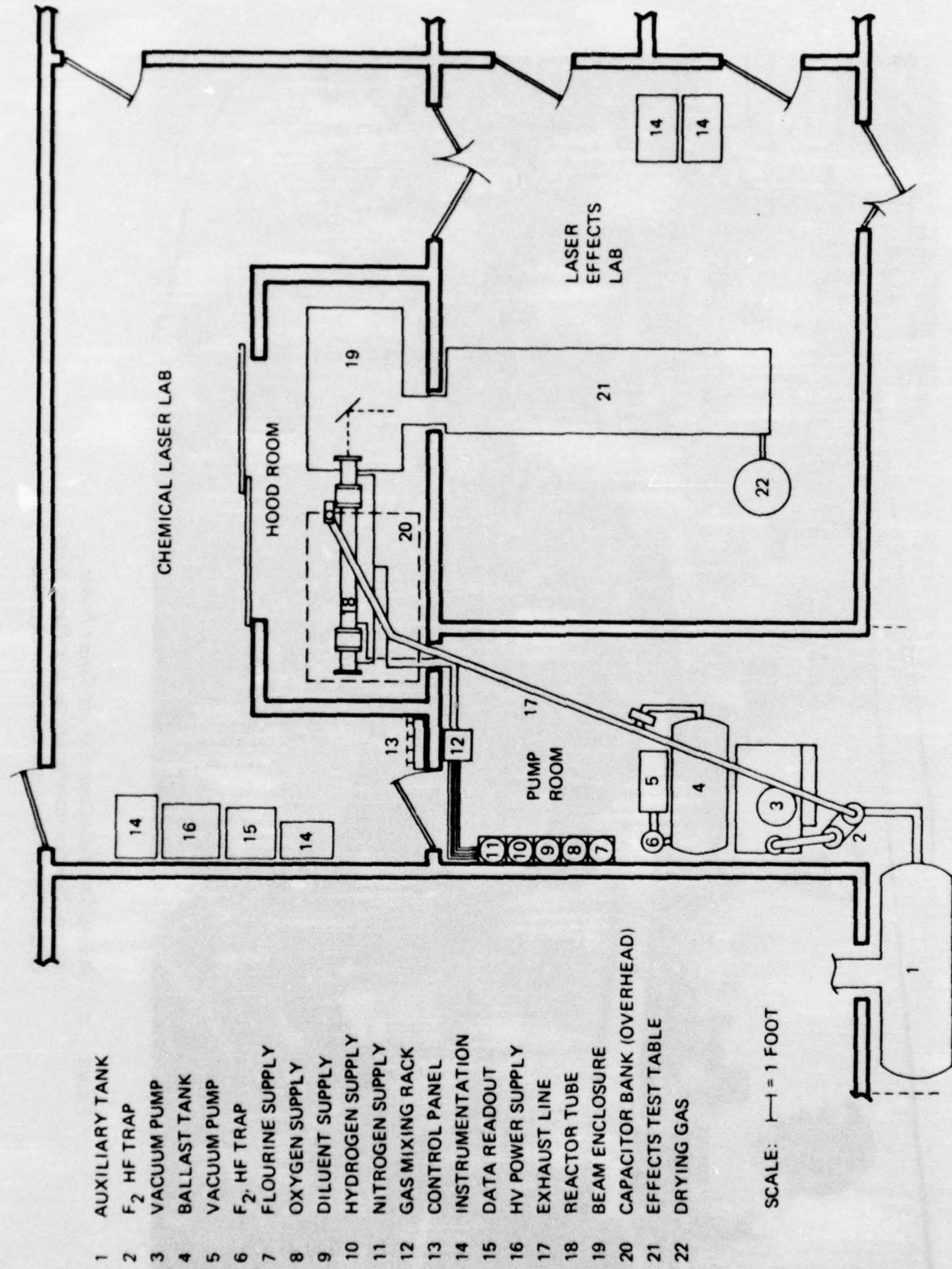


Figure 7. Floor Plan for HF Pulsed Chemical Laser Effects Laboratory. Beam Folding Mirror (in Beam Enclosure 19) Directs the Beam Into the Laser Effects Area.

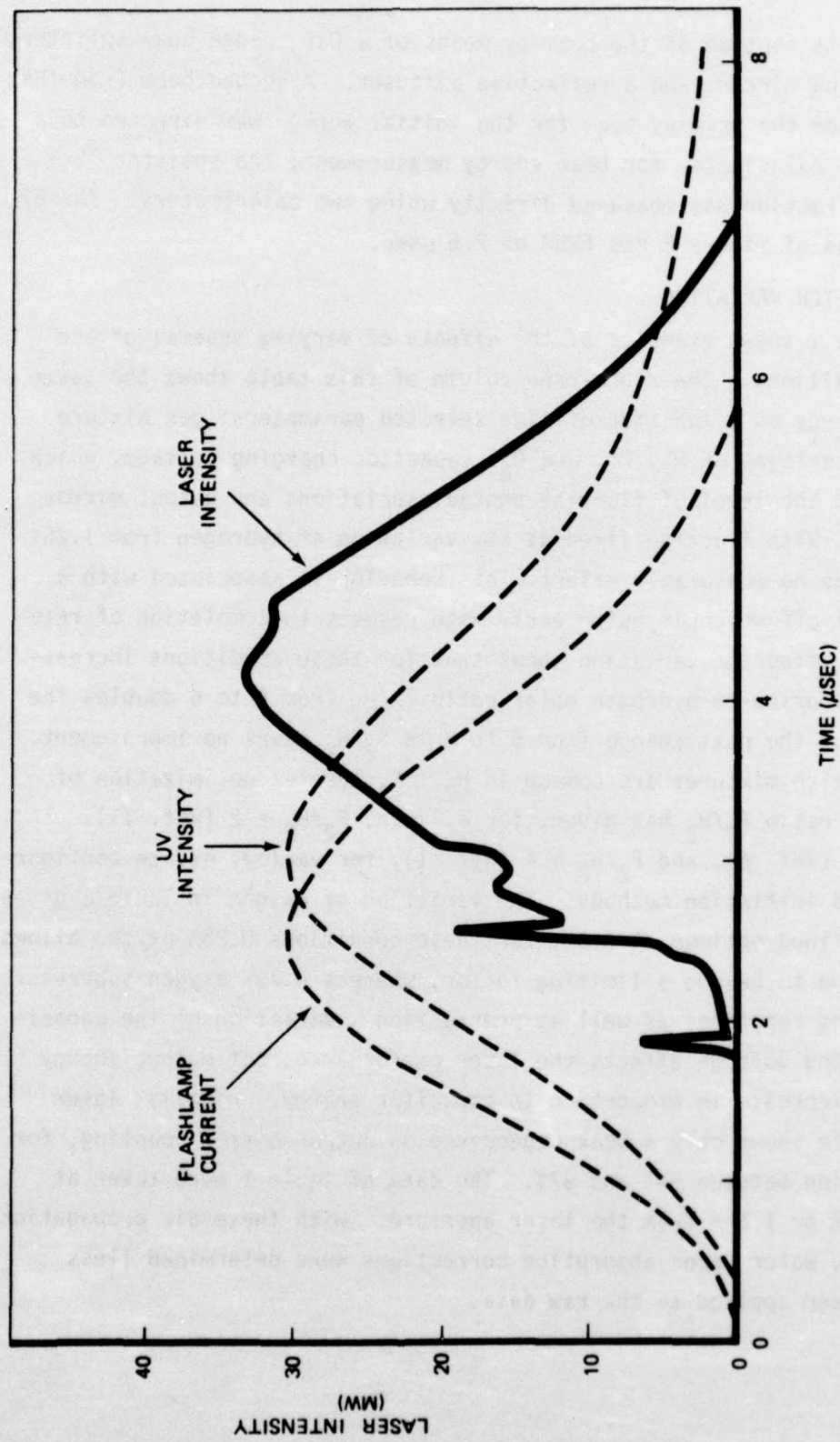


Figure 8. Time Relationships Between (1) the Current Profile for a 30-KV Discharge Through a Flashlamp, (2) the Associated UV Time Profile, and (3) the Resulting HF Laser Output Pulse

entire cross section of the beam by means of a CaF_2 wedge beam splitter, a collecting mirror, and a reflective diffuser. A second beam from the splitter (or the primary beam for the initial work) was directed to a thermopile calorimeter for beam energy measurement; the splitter sampling fraction was measured directly using two calorimeters. The 87 J laser pulse of figure 8 has FWHM of 2.6 μsec .

4. PARAMETER VARIATION

Table I shows examples of the effects of varying several of the laser conditions. The right-hand column of this table shows the laser output energy as a function of five selected parameters: gas mixture molar percentages of H_2 , F_2 , and O_2 ; capacitor charging voltage, which determines the level of fluorine photodissociation; and output mirror coupling. With fluorine fixed at 5%, variation of hydrogen from 1.25% to 2.5% has no measurable effect. This behavior is associated with a lasing cut-off which is quite early with respect to completion of reaction. The fluorine variation shows that for these conditions increasing the fluorine-to-hydrogen molar ratio F_2/H_2 from 4 to 6 doubles the output, but the next change from 6 to 8 in F_2/H_2 gives no improvement. Fluorine-rich mixtures are common in $\text{H}_2 + \text{F}_2$ lasers; optimization of the molar ratio F_2/H_2 has given, for example, $\text{F}_2/\text{H}_2 = 2$ (Ref. 11), $\text{F}_2/\text{H}_2 = 3$ (Ref. 6), and $\text{F}_2/\text{H}_2 = 4$ (Ref. 1), for various device configurations and initiation methods. The variation of oxygen in Table I gives a well-defined optimum at 0.5%; for these conditions 0.25% oxygen allows prereaction to become a limiting factor, whereas 0.75% oxygen suppresses the pumping reactions as well as prereaction. Variation of the capacitor charging voltage affects the laser performance, but output energy does not increase in proportion to capacitor energy. Finally, laser performance shows only a weak dependence on output mirror coupling, for transmission between 54% and 87%. The data of Table I were taken at either 0.8 or 1.6 m from the laser aperture. With these air propagation distances, water vapor absorption corrections were determined (less than 7%) and applied to the raw data.

TABLE 1
VARIATION OF LASER OUTPUT AS A FUNCTION OF LASER CONDITIONS.

%H ₂	%F ₂	%O ₂	Capacitor Voltage (kV)	Mirror Transmission (%)	Laser Output (J)
1.25	5.0	0.5	30	87	61
1.9	5.0	0.5	30	87	63
2.5	5.0	0.5	30	87	61
1.25	5.0	0.5	30	87	52
1.25	7.5	0.5	30	87	110
1.25	10.0	0.5	30	87	109
1.25	7.5	0.25	30	87	75
1.25	7.5	0.5	30	87	104
1.25	7.5	0.75	30	87	82
1.25	7.5	0.5	30	87	104
1.25	7.5	0.5	36	87	130
1.25	7.5	0.5	30	87	107
1.25	7.5	0.5	30	75	98
1.25	7.5	0.5	30	54	98

NITROGEN, NOT SHOWN AMONG THE GAS MOLAR PERCENTAGES, MAKES UP THE REMAINDER OF EACH GAS MIXTURE. THESE DATA ARE FOR ROOM TEMPERATURE GAS MIXING, 1 ATM TOTAL PRESSURE, AND FOR INITIATION BY FOUR FLASH-LAMSP.

5. FAR-FIELD BEAM PROFILE

The far-field beam characteristics are of particular interest in beam-target interaction measurements. With a 164-cm focal length mirror, burn patterns were observed as a function of mirror-to-target distance with the minimum spot size defining the focus. In that focal plane the energy profile of the beam was measured for the case of 8 lamps installed. Scanning across the diameter of the beam in both the vertical and the horizontal directions with a calorimeter apertured to 0.25-cm diameter gave the results shown in figure 9. Almost all of the energy falls within a central area which is 1.7 cm diameter (FWHM) and is quite uniform in energy density. Some asymmetry is expected from the aberration incurred in focussing the beam off-axis. The central spot of 1.7 cm FWHM was also observed as a well-defined high-intensity zone in burn patterns taken in this target plane. A less symmetric beam profile was utilized in some of the laser effects experiments. In these cases, the laser was operated with only four flashlamps and produced an elliptical spot of .4 x .6 cm dimensions at the focus of a 37.5 cm focal length mirror.

6. BEAM DIVERGENCE

For the data of figure 9 there were eight flashlamps in the reactor which limited the effective clear aperture of the laser to about 10 cm diameter. The far-field divergence expected from a cavity of large Fresnel number in high-order mode operation has been approximated by Fortin (Ref. 12) under the assumption of equipartition of energy among transverse modes. The predicted full angle divergence to the 30% - intensity point $\theta = 1.06 w / \sqrt{IR}$. With 10 cm as waist diameter w , cavity length $l = 229$ cm, and mirror radius $R = 40$ m, $\theta = 11.1$ milliradians. The measured 30% - intensity spot diameter of 1.8 cm (figure 9) and the mirror focal length give a measured divergence of $1.8 \text{ cm} / 164 \text{ cm} = 11.0$ milliradians.

7. REPEATABILITY

Lasers using mixed hydrogen and fluorine are sometimes erratic in behavior or require cryogenic gas mixing temperatures (Ref. 1). For this laser, however, the shot-to-shot repeatability is excellent.

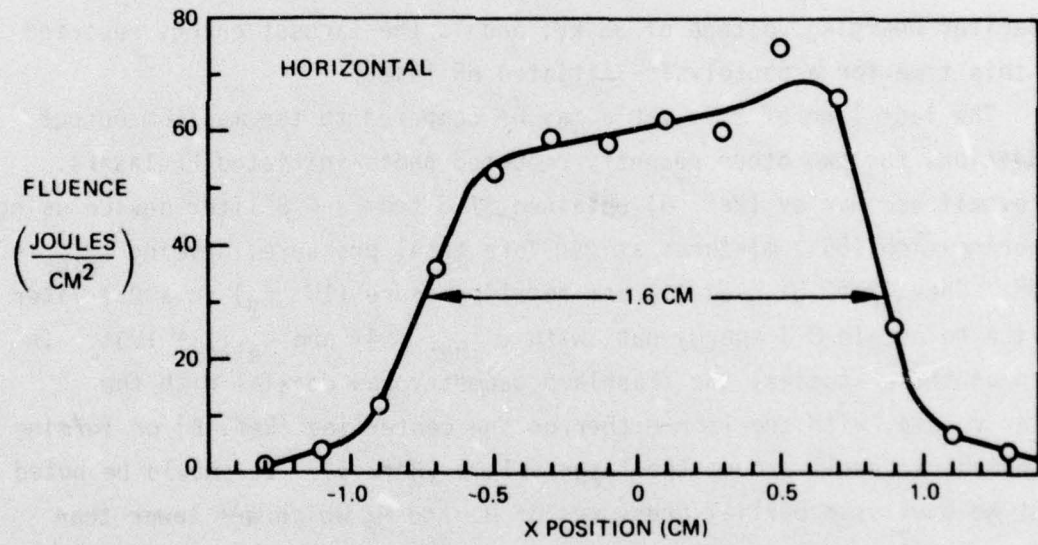
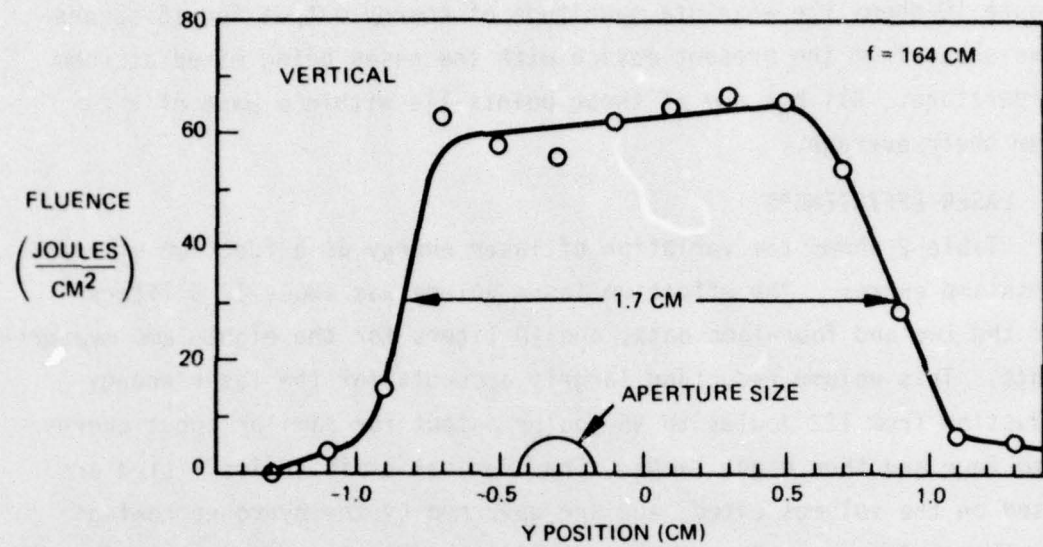


Figure 9 . Far-Field Profiles Measured With an Apertured Calorimeter in the Focal Plane of an $f = 164 \text{ cm}$ Mirror

Figure 10 shows the absolute magnitude of energy output for 15 successive shots from the present device with the gases being mixed at room temperature. All but one of these points lie within a band of $\pm 2\%$ from their average.

8. LASER EFFICIENCIES

Table 2 shows the variation of laser energy as a function of input flashlamp energy. The effective laser volume was about 12.8 liters for the two and four-lamp data, and 10 liters for the eight-lamp measurements. This volume reduction largely accounts for the laser energy reduction from 122 joules to 95 joules output for similar input energy into four and then eight lamps. The chemical efficiencies listed are based on the volumes cited, and are governed by the hydrogen content for these mixtures. The electrical efficiencies are based on the total electrical energy stored in the flashlamp capacitor bank, E_{IN} . The last output energy shown in this table is 152 J, corresponding to a capacitor charging voltage of 36 kV, and is the largest energy reported at this time for a photolysis-initiated HF laser.

The last line of this table may be compared to the maximum output conditions for two other recently reported photo-initiated HF lasers. Batovskii and Gur'ev (Ref. 6) obtained 37 J from a 4.5 liter device using fluorine-rich (55%) mixtures at 250 Torr total pressure, giving $\epsilon_{elec} = 3.9\%$. Chen (Ref. 5) used 1.1 atm total pressure (10% F_2) in a 0.1 liter device to obtain 8 J energy out, with $\epsilon_{chem} = 4\%$ and $\epsilon_{elec} = 1.3\%$. In both of these studies, the flashlamp geometry was coaxial with the laser volume, with the lamp either on the centerline (Ref. 6) or forming a concentric shell around the laser volume (Ref. 5). It should be noted that we have used partial pressures of H_2 and F_2 which are lower than those of other photolysis devices, and much lower than those of e-beam initiated $H_2 + F_2$ lasers (Refs. 4, 13, 14).

9. BEAM ATTENUATION

Applications of this laser call for target-delivered laser pulses having variable total energy and absolute intensity, but a constant relative pulse shape in time. This control is particularly important in

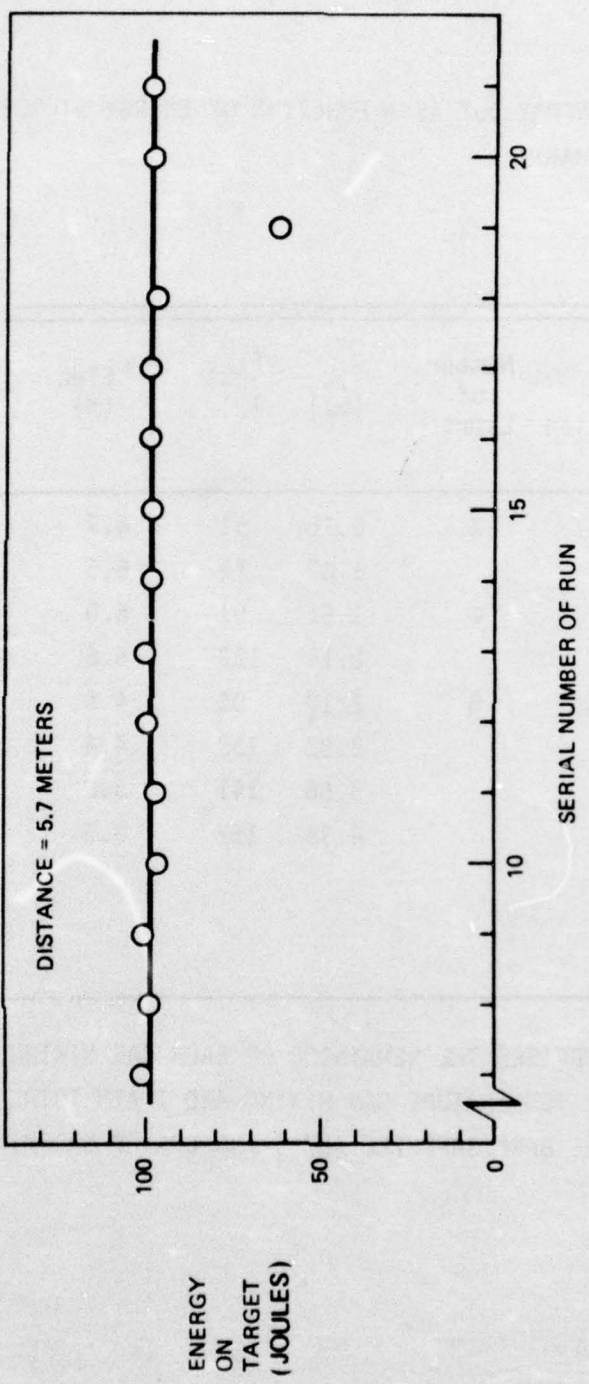


Figure 10. Absolute Magnitude of Laser Energy on a Target 5.7 Meters from the Laser for Several Sequential Shots in Which H₂-F₂ Mixing was Done at Room Temperature

TABLE 2

VARIATION OF LASER ENERGY OUT AS A FUNCTION OF ENERGY STORED IN THE FLASHLAMP CAPACITOR BANK.

Molar Percentages of $H_2/F_2/O_2$	Output Mirror Transmission	Number of Lamps	E_{IN} (kJ)	E_{OUT} (J)	ϵ_{Elec} (%)	ϵ_{Chem} (%)
2.5/5.0/0.25	87%	2	0.76	51	6.7	0.7
			1.09	71	6.5	1.0
		4	1.51	91	6.0	1.3
			2.18	122	5.6	1.7
1.25/7.5/0.5	75%	8	2.10	95	4.5	3.4
			3.02	132	4.4	4.7
			3.66	141	3.9	5.0
			4.36	152	3.5	5.4

NITROGEN DILUENT COMPRIMES THE REMAINDER OF EACH GAS MIXTURE. THESE DATA ARE FOR AMBIENT TEMPERATURE GAS MIXING AND 1 ATM TOTAL PRESSURE. THE TWO COUPLERS WERE BARE SAPPHIRE (87%) AND COATED SAPPHIRE (75%).

the ignition threshold measurements discussed in Section III.3. As indicated earlier, the laser beam energy and pulse shape are monitored by reflections from a CaF_2 wedge shown in figure 11. All attenuation of the incident laser beam was accomplished, for the experiments reported here, before the beam entered the wedge. Two energy variations readily available are those due either to changes in laser gas mixture or changes in flashlamp discharge energy and hence fluorine photo-dissociation level. However, either of these methods will in general produce changes in the output pulse time profile as well as more subtle changes in laser output wavelength as the relative strength of individual vibration-rotation transitions change. It is preferable therefore, to operate the laser with nearly constant conditions and do the beam energy variation externally as an attenuation procedure. Again the attenuation procedure should be free of effects which would either attenuate some of the discreet wavelengths more than others or alter the spatial profile of the target-delivered pulse.

A number of infrared beam attenuation schemes have been reported in references 15 to 18. Several of these satisfy the two criteria mentioned above, but lack simplicity of construction and operation, or could not be adapted to our large aperture (~ 14 cm diam) requirement.

Two beam attenuation schemes were used in the present work. The first, designated the sector attenuator, consisted of two aluminum discs with four sector-shaped apertures, arranged so that relative rotation of the discs varied the size of the open sectors. The device was inserted in the near field region of the beam and had sand-blasted surfaces to minimize feedback into the laser. Far field beam patterns were observed for several attenuator settings varying from 100% to 1.5% of a 60 J laser pulse in steps of 1/2. These patterns were compared with a similar burn series in which the beam energy was reduced by changing gas mixture composition. These burn patterns consisted of a central high intensity zone surrounded by a low energy halo which consisted of a small part of the total laser energy. Comparing the burn patterns from the two methods of beam reduction, the central

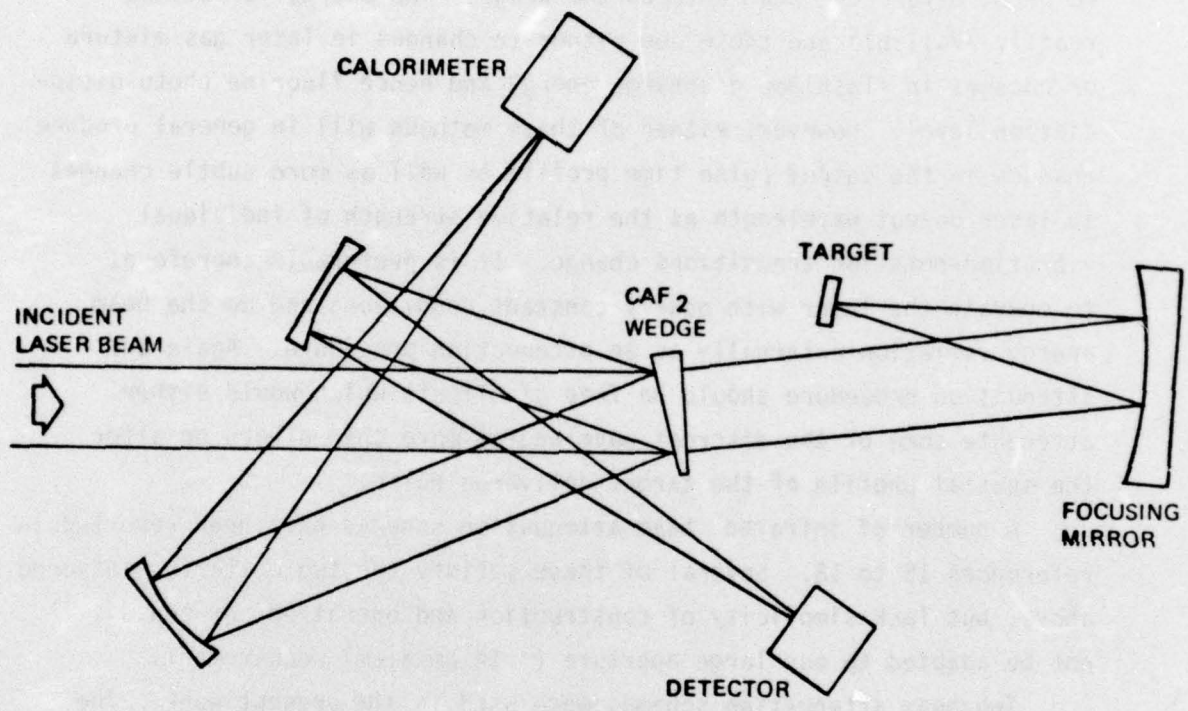


Figure 11. Schematic Diagram of Laboratory Optical Arrangement

high-intensity zone of the beams were indistinguishable at all energy levels; the central zone obtained with the sector attenuator retained its shape and uniformity down to 1% transmission. The only evidence of the sector apertures in the far field occurred in a low-level halo of larger diameter.

The second attenuation scheme consisted of a frame by which one of three attenuating materials intercepted the near-field beam at a variable angle. The interchangeable materials were (1) 0.7 mm thick aluminum with 1 mm diameter perforations spaced about 0.4 mm apart, (2) 0.13 mm teflon sheet, and (3) 0.26 mm teflon sheet. Figure 12 shows the resulting beam energies, expressed as percent of the full attenuated beam. Over this entire range, the pulse time-profile shows little or no change in shape. Spectral composition has not been explicitly studied as a function of attenuation, but since different lines are known to lase at different times within the total pulse in devices of this type (Ref. 5) a total pulse shape which is invariant with respect to attenuation is taken to imply the absence of any major wavelength shifts due to that attenuation. This attenuator device (or scheme) also preserves the far-field beam spatial pattern and uniformity.

10. HOLOGRAPHIC SPECTROSCOPY

A holographic technique (Ref. 19) has been applied to measurement of the near-field, time-integrated, space-resolved spectrum of the HF pulsed chemical laser. Figure 13 shows the optical arrangement for formation of a phase hologram by the angular superposition of two near-field beams on gelatine. The beams are generated by amplitude division, and the paths are matched carefully to preserve mutual temporal coherence at the hologram plane. Distinct wavelength contributions to the hologram are then separated in the reconstruction arrangement shown in figure 14. Illumination of the hologram by coherent light with wavelength different from the writing HF wavelengths results in angular separation of the spectral components by diffraction. Data were observable primarily in the first three orders. Illumination by the

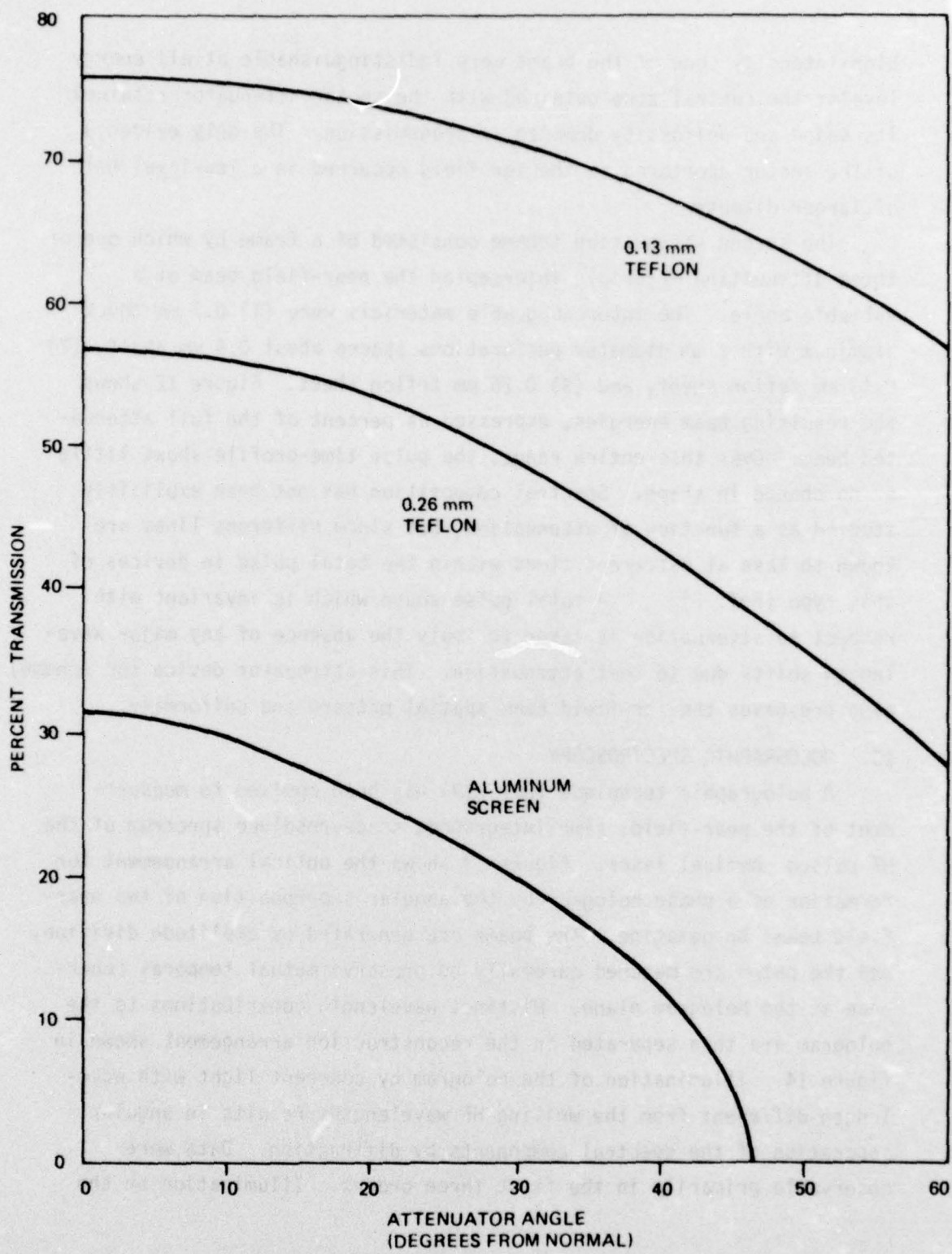


Figure 12. HF Laser Beam Attenuation Curves Showing Availability of Laser Pulses in the Range 0-75% of Full Energy Using Teflon Sheets or Metal Screening at Various Transmission Angles.

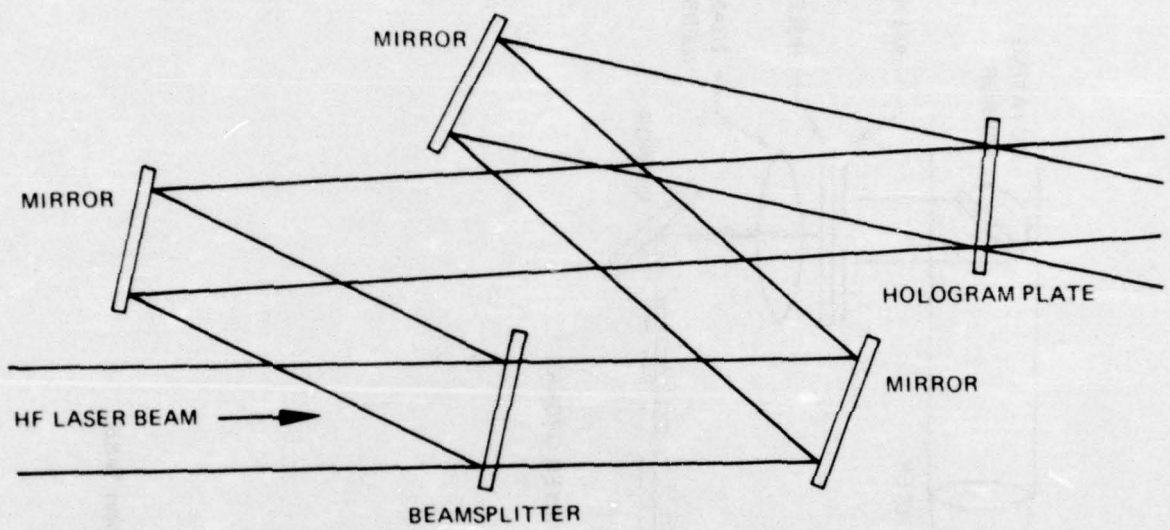


Figure 13 . Hologram Recording Setup

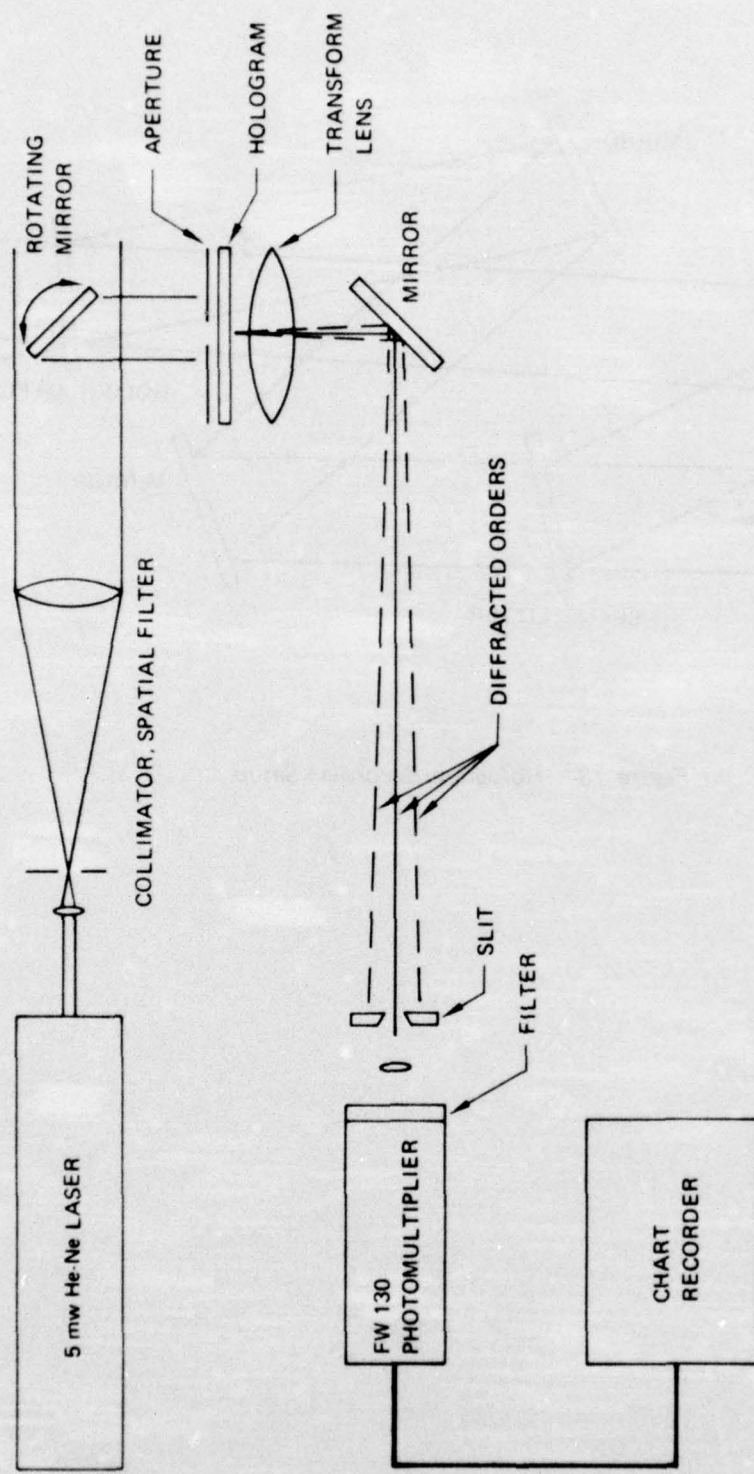


Figure 14. Hologram Reconstruction Setup

He-Ne laser of a particular zone within the 10 cm diameter hologram then provides spectral analysis of that particular spatial zone in the HF near-field beam. Figure 15 is an example of the output of the recording apparatus of figure 14. Linearity of response is not assured, but the general order of importance of the major HF transitions may be inferred. The major lines appearing in figure 15, taken near the HF laser axis, persist in the other spatial zones of the laser for this hologram, with some variations in relative amplitudes. These data were from a 4-lamp laser test corresponding to 43 J at the target. It may be noted that the six lines designated in figure 15 belong to only two cascade series:

$$\begin{aligned} P_3(5) &\rightarrow P_2(6) \rightarrow P_1(7), \text{ and} \\ P_3(6) &\rightarrow P_2(7) \rightarrow P_1(8). \end{aligned}$$

All of these six lines were observed by Chen (Ref. 5) for similar HF lasing conditions. Previous HF laser spectroscopy at Boeing (Ref. 7) with a small device showed the strongest single transition to be $P_2(6)$, as it is for the present device.

11. WET-AIR ABSORPTION

The energy of the pulsed HF laser beam, transmitted over a totally enclosed 572 cm path length, was measured with eight lamps installed for (1) partial pressure of water vapor $P_w = 9.5$ Torr in ambient laboratory air, and (2) flowing dry nitrogen with a steady state $P_w = 1.0$ Torr. Water vapor content of the gases was measured by dew point. The measurements were made during a uniform series of laser shots and several tests were made under each condition to average out small shot-to-shot laser energy variations. Beam optics and total pressure (1 atm) were not changed between (1) and (2). The measured ratio of energies delivered through these two gas media was 0.82. If this attenuation is entirely attributed to the measured difference in water vapor, then a single-exponential approximation to the water vapor effect gives an effective absorption coefficient of $k_{\text{eff}} = 4 \times 10^{-5} P_w \text{ cm}^{-1}$, where P_w is the water vapor pressure in Torr.

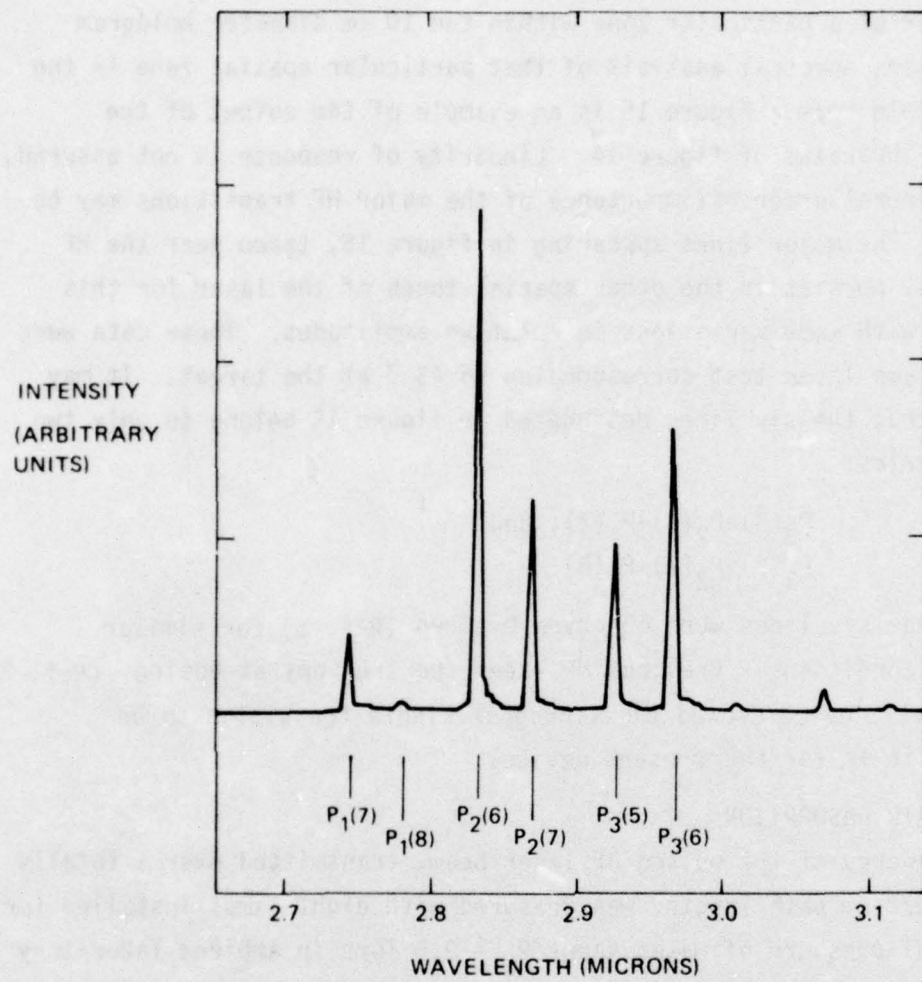


*Figure 15. Second Order Spectrum From a 1 cm² Hologram.
Sample Situated 3 cm From the HF Laser Axis*

This measurement may be compared to results expected from the HF absorption calculations of McClatchey and Selby (Ref. 20). To make this comparison, we make use of the HF laser spectral composition reported in Section III.10 which was measured for a four-lamp laser configuration. The six lines which are identified in figure 14 have expected absorption coefficients ranging from $k_{\text{eff}} = 9.45 \times 10^{-5} P_w \text{ cm}^{-1}$ for $P_1(8)$ to $k_{\text{eff}} = 1.67 \times 10^{-7} P_w \text{ cm}^{-1}$ for $P_3(6)$. The measured K_{eff} above lies within this range. To test the correlation of our result with reference 20, we made an approximate calculation of the attenuation factor expected. We assume (1) an approximate set of relative transmitted line strengths based on the holographic results of Section III.10, and (2) that the relative line strengths are similar for the 4-lamp laser configuration, for which spectral composition is known, and the 8-lamp arrangement for which the wet-air attenuation was measured. The six lines are discussed as an ordered set, as listed in figure 14 for increasing wavelength:

$$P_1(7), P_1(8), P_2(6), P_2(7), P_3(5), P_3(6).$$

Approximate relative line strengths from figure 14 are taken as $u_i = (1, 0, 7, 3, 2, 4)$. Absorption coefficients of reference 20 along with P_w and path length l_w then imply relative line strengths $v_i = (1.16, 0, 9.18, 3.02, 2.02, 4.00)$ before wet air attenuation and at the laser aperture. From these v_i and the actual water vapor pressure P_w and path length l_w appropriate to the above measured ratio of delivered energies, one obtains a predicted set of line strengths, $w_i = (0.92, 0, 5.82, 2.98, 1.98, 4.00)$. The predicted attenuation factor is then $f = (\sum w_i / \sum v_i) = 15.68/19.38 = 0.81$ which compares well with the measured value of 0.82.

SECTION III

PULSED CHEMICAL LASER EFFECTS STUDIES

1. LSD WAVE PROPAGATION STUDIES

The pulsed chemical laser described in Section II was used in a series of laser effects studies. These studies included: 1) ignition threshold measurements of laser-supported absorption waves, 2) thermal coupling to solid targets, 3) impulse coupling, and 4) physical property measurements using spectroscopy and interferometry. It was one of the goals in these experiments to compare the results with those previously obtained at 1.06, 5, and 10.6 microns wavelength. In order to make these comparisons, it was necessary to make a fairly good characterization of the temporal and spatial properties of the laser beam. The far-field intensity pattern and time dependence of the pulsed HF laser was indicated in Section II. In order to make simple calculations, however, it is extremely useful to approximate that basic data by simple analytical approximations.

a. Analytical Approximations to the Focal Energy Distribution and the Power Time Dependence

Figure 16 shows a typical laser pulse shape, for an eight lamp configuration, and a simple triangular approximation to the pulse. The two small "spikes" of laser power occurring at the beginning of the laser pulse are usually of the magnitude indicated. Occasionally, however, these amplitudes are slightly increased or decreased as the exact operating conditions of the laser vary. The indicated "triangular" approximation to the laser power, $p(t)$, is defined by:

$$p(t) = \begin{cases} \frac{t}{2.17} & 0 < t < 2.17 \text{ } \mu\text{sec} \\ \frac{4.56-t}{2.39} & 2.17 < t < 4.56 \text{ } \mu\text{sec} \\ 0 & t > 4.56 \text{ } \mu\text{sec} \end{cases} \quad (1)$$

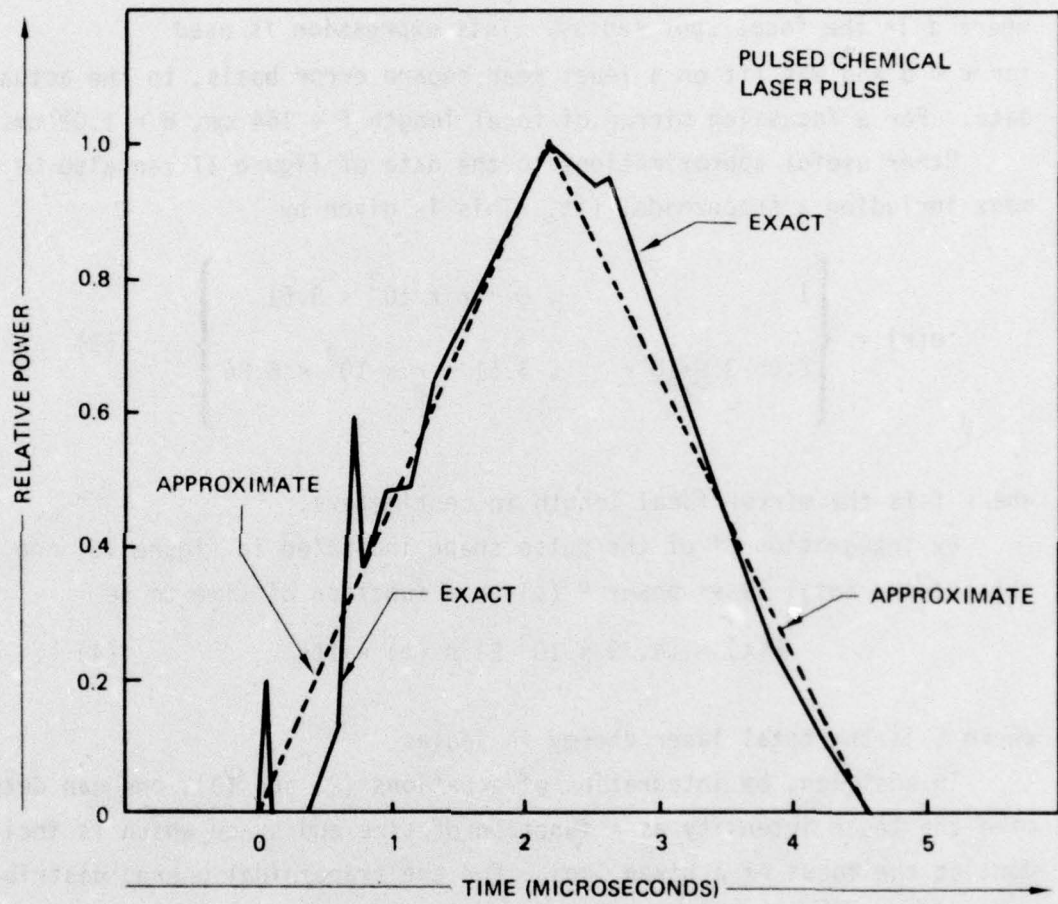


Figure 16. "Exact" and Approximate Pulsed Chemical Laser Pulse Shape

where t is in μsec and $p(t)$ is normalized to the peak power occurring at $t = 2.17 \mu\text{sec}$.

Figure 17 shows the normalized energy distribution as first shown in the upper curve in Figure 9. An appropriate analytical approximation is given by

$$e(r) = 1 - \frac{r^4}{d^4} \quad (2)$$

where d is the focal spot radius. This expression is used for $r < d$ and was fit on a least mean square error basis, to the actual data. For a focussing mirror of focal length $f = 164 \text{ cm}$, $d = 1.02 \text{ cm}$.

Other useful approximations to the data of figure 17 can also be made including a trapezoidal fit. This is given by

$$e(r) = \begin{cases} 1 & , 0 < \frac{r}{f} \times 10^3 < 3.51 \\ \frac{2.05 - 3.0 \times 10^2 r}{f} & , 3.51 < \frac{r}{f} \times 10^3 < 6.86 \end{cases} \quad (3)$$

where f is the mirror focal length in centimeters.

By integration of the pulse shape indicated in figure 16, one obtains the total laser power $P(t)$ as a function of time to be

$$P(t) = (4.39 \times 10^5 E) p(t) \text{ watts} \quad (4)$$

where E is the total laser energy in joules.

In addition, by integration of equations (2) and (3), one can determine the laser intensity as a function of time and space which is incident at the focus of a given lens. For the trapezoidal energy distribution (indicated by equation (3)), one obtains

$$q(r,t) = \left\{ e(r)p(t) \right\} \frac{5.02 \times 10^9 E}{f^2} \text{ watts/cm}^2 \quad (5)$$

on the other hand, for the r^4 approximation given by equation 2, one obtains,

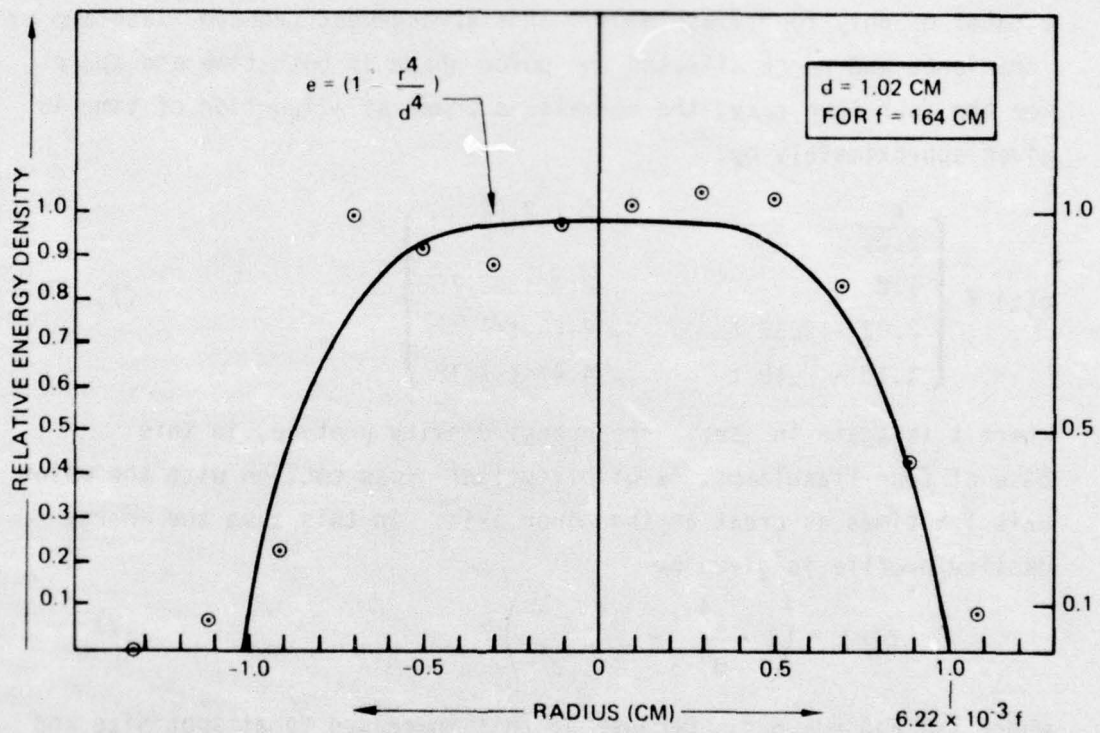


Figure 17. Analytic Fit to Far-Field HF Laser Beam Profile

$$q(r,t) = \left\{ e(r)p(t) \right\} \frac{5.42 \times 10^9}{f^2} E \text{ watts/cm}^2 \quad (6)$$

It should be noted that equations (5) and (6) apply, strictly speaking, to only that data obtained using eight flashlamps in the laser. The closeness of the numerical values given by equations (5) and (6) shows that the estimates of laser intensity are not very sensitive to the exact approximations used.

For a large number of experiments, to be reported later, we used a total of only four flashlamps. This arrangement reduced flashlamp uv irradiance and hence affected the pulse shape in both time and space. For the four-lamp case, the normalized power as a function of time is given approximately by,

$$p(t) = \begin{cases} \frac{t}{2.01} & , 0 < t < 2.02 \\ 1.0 & , 2.02 < t < 2.76 \\ 2.02 - 0.37 t & , 2.76 < t < 4.47 \\ 1.10 - .15 t & , 4.47 < t < 7.18 \end{cases} \quad (7)$$

where t is again in μsec . The energy density profile, in this case of four flashlamps, is of elliptical cross section with the major axis 1.5 times as great as the minor axis. In this case the energy density profile is given by

$$e(r) = \left(1 - \frac{x^4}{d^4} - \frac{y^4}{1.5^4 d^4} \right) \quad (8)$$

where $x < d$ and $y < 1.5 d$. Because of this increased focal spot size and because of the increased pulse length, the peak laser intensity produced by a fixed amount of energy is reduced. As previously found, $d = 1.02$ for $f = 164 \text{ cm}$. In this case, the laser intensity at the lens focus is given by

$$q(r,t) = \left\{ e(r)p(t) \right\} \frac{2.37 \times 10^9}{f^2} E \text{ watts/cm}^2 \quad (9)$$

It should be noted that using these analytical approximations, the peak laser intensity (for the case of four flashlamps) is reduced by a factor of 2.29 compared to the standard 8-flashlamp operating conditions.

For a delivered laser energy of 35 joules and for $f = 37.5$ cm, equation 9 leads to a peak laser irradiance of

$$q_{\max} = 5.90 \times 10^7 \text{ watts/cm}^2 \quad (10)$$

b. Propagation of Laser-Supported Detonation (LSD) Waves

Laser-supported absorption (LSA) waves are produced in gases whenever at least two conditions are satisfied. First of all, an initial ionization must be produced which ignites the laser-supported absorption wave. In some cases, this initial ionization may be produced by target vaporization itself. In other cases, artificial ignition of wave can occur by the production of an electrical spark. The second condition for producing an LSA wave is that the laser intensity be large enough to supply the power required by the wave. At the lower laser intensities ($q < 10^5$ watts/cm²), for example, the LSA waves propagate at subsonic velocities. At laser intensities of 10^7 watts/cm² and for a wavelength of 10 microns, the LSA wave propagation velocity approaches 5×10^5 cm/sec in air. Because of the well known similarity of these high Mach number waves with chemical detonation waves, these supersonic LSA waves are called laser-supported detonation (LSD) waves (Refs. 21 and 22).

If only the first of the above two conditions is satisfied, a plasma is produced at a solid surface which is confined to the immediate vicinity of the surface. When LSD waves are ignited and maintained, there is an extended brilliant white-blue flash and a loud explosion-like noise.

Figure 18 shows examples of LSD wave photographs obtained

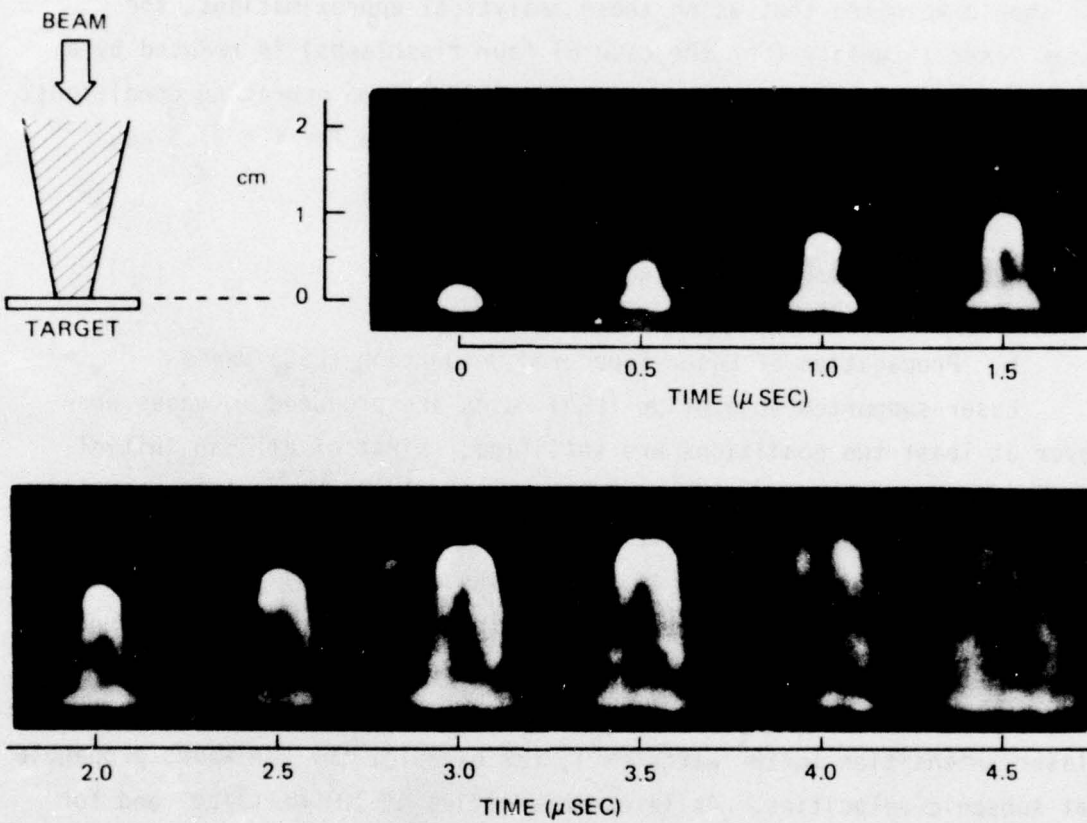


Figure 18. Framing Camera Data Showing the Progression of an LSD Wave at 0.5 - μ sec Intervals From an Aluminum Surface

with a TRW image converter camera. All the times indicated in the figure are with respect to the ignition time t_i of the LSD wave and not with respect to the laser pulse time itself. An estimate of t_i is obtained from the image converter camera electronic monitor which indicates when the optical pickup triggers the camera. For an incident energy of 56 joules on a 6061 Al. alloy target the ignition time was

$$t_i \approx 0.95 \text{ usec} \quad (11)$$

The theoretical velocity v of a propagating LSD wave is well-known to be (Ref. 22):

$$v = \left[2(\gamma^2 - 1) \frac{q}{\rho_0} \right]^{1/3} \quad (12)$$

where $\gamma \approx 1.18$ is the ratio of specific heats and $\rho_0 \approx 1.22 \text{ Kg/m}^3$ is the mass density of atmospheric pressure air at 20°C . For a collimated laser beam with a time varying intensity given by equation 5, one obtains the maximum LSD velocity as a function of time for $f = 37.5 \text{ cm}$ to be

$$v = 2.2 \times 10^7 (Et)^{1/3} \text{ cm/sec} \quad (13)$$

(for times such that $0 < t < 2.17 \text{ usec}$). For the conditions of figure 17, ($E = 56 \text{ joules}$) one obtains

$$v = 8.4 \times 10^7 t^{1/3} \text{ cm/sec.} \quad (14)$$

Thus at the time of ignition, $t_i = 0.95 \text{ usec.}$, one finds

$$v(t_i) = 8.3 \times 10^5 \text{ cm/sec} \quad (15)$$

The actual propagation of LSD waves depends, of course, on the laser intensity at the instantaneous position of the wave. An

approximate expression for the laser intensity as a function of distance z away from the focus is

$$q(z,r,t) = \frac{q(r,t)}{\left[1 + \left(\frac{Rz}{fd}\right)^2\right]} \quad (16)$$

where $q(r,t)$ is the laser intensity at the focus ($z = 0$) and given by equations 5, 6, or 9. In equation 16, R is the radius of the laser beam at the focussing mirror of focal length f . For $R = 7.6$ cm and $f = 37.5$ cm, one obtains from equation 5, 13, and 16

$$\frac{dz}{dt} = 2.84 \times 10^5 \left\{ \frac{Ep(t)}{(1 + .76 z^2)} \right\}^{1/3} \text{ cm/sec} \quad (17)$$

Figure 19 shows the results of integrating equation 17 using equation 1 for $p(t)$ and $t = .95 \mu\text{sec}$ for the ignition time t_i .

The actual laser irradiance at the position of the front of the LSD wave is also indicated on figure 19. For this case, the laser intensity is nearly constant as a combined result of the rising laser power and the increasing laser spot size as the LSD wave propagates. This leads, as indicated by figure 19, to an almost constant LSD wave velocity. The ignition time of $t_i = 0.95 \mu\text{sec}$ is surprisingly long at these intensities. The actual absorbed peak energy density at the target (before ignition on the rising part of the pulse) is

$$E_{\text{absorbed}} = 8.2 \times 10^{11} \alpha Et^2 \text{ joules/cm}^2 \quad (18)$$

which for $E = 56.6$ joules and $t_i = 0.95 \mu\text{sec}$ leads to

$$E_{\text{absorbed}} = 42.0 \alpha \text{ joules/cm}^2 \quad (19)$$

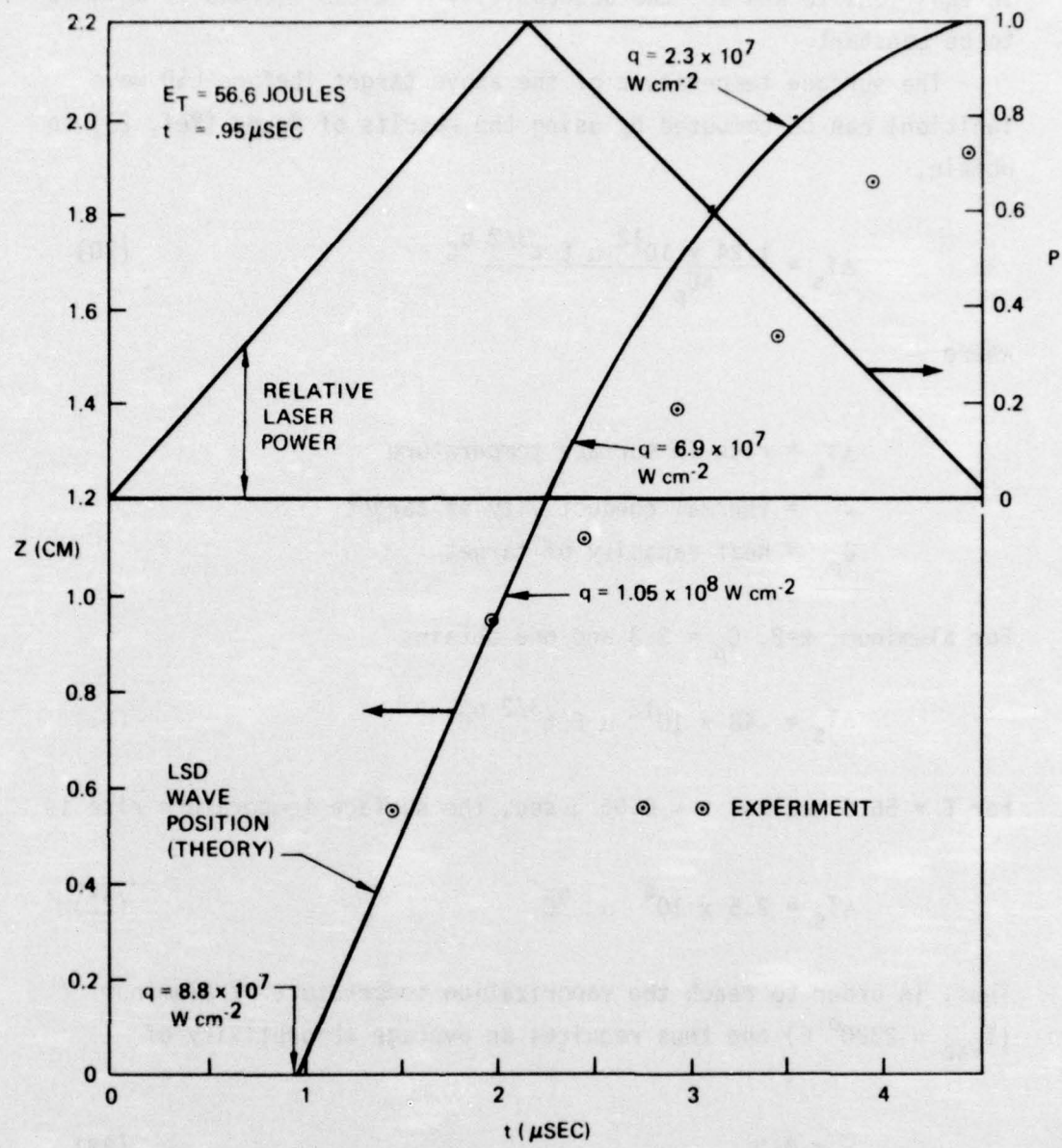


Figure 19. Laser-Supported Detonation Wave Position as a Function of Time for $0 < t < 4.56 \mu\text{sec}$

In equations 18 and 19, the absorptivity α at 2.8 microns is assumed to be constant.

The surface temperature of the above target (before LSD wave ignition) can be computed by using the results of Ready (Ref. 23) to obtain,

$$\Delta T_s = \frac{1.24 \times 10^{12} \alpha E t^{3/2}}{kC_p} {}^{\circ}\text{C} \quad (20)$$

where

ΔT_s = rise in surface temperature

k = thermal conductivity of target

C_p = heat capacity of target

For aluminum, $k=2$, $C_p = 3.3$ and one obtains

$$\Delta T_s = .48 \times 10^{12} \alpha E t^{3/2} {}^{\circ}\text{C} \quad (21)$$

For $E = 56.6$ joules, $t = 0.95 \mu\text{sec}$, the surface temperature rise is

$$\Delta T_s = 2.5 \times 10^4 \alpha {}^{\circ}\text{C} \quad (22)$$

Thus, in order to reach the vaporization temperature of aluminum ($T_{vap} \approx 2520 {}^{\circ}\text{C}$) one thus requires an average absorbtivity of

$$\bar{\alpha} = 0.1 \quad (23)$$

at a wavelength of 2.8 microns. It should be noted, however, that the surface temperature computed here corresponds to an ideal surface. As noted by Walters (Ref. 24) ignition of LSD waves is most likely caused by vaporization of small flakes of surface material. In this

case, the temperature rises much faster and ignition occurs at lower fluences.

Figure 20 is a streak photograph of the propagation of an LSD wave taken through a 1/4 mm slit with a TRW image converter camera. The laser was again operating with eight flashlamps and used a 37.5 cm focal length mirror. In this case, the focal plane irradiance given by equations 5 or 6 is valid. This streak photograph shows that during the ignition stage of the LSD wave, a relatively low velocity plasma ($V \approx 2 \times 10^5$ cm/sec) is moving away from the target surface. At LSD wave ignition, approximately 0.6 μ sec, the plasma velocity increases to about 10^6 cm/sec. A careful data analysis showing both the position of the LSD wave front and the laser pulse shape is shown in figure 21. The maximum propagation velocity is $V = 1.3 \times 10^6$ cm/sec. A comparison of the theory of equation 17 and experiment yields very good agreement if a constant additional displacement of 0.15 cm is added to the theoretical prediction. This displacement of the initial plasma corresponds to the observed low velocity plasma at the ignition time of 0.6 μ sec. For the results of figure 21, the absorbed energy fluence and surface temperature at ignition are

$$E_{\text{absorbed}} = 18.9 \alpha \text{ joules/cm}^2 \quad (24)$$

$$\Delta T_s = 1.42 \times 10^4 \alpha^0 \text{ K}$$

Figure 22 shows the near-threshold radial (as contrasted to the axial) growth of plasma ignition at the surface. Since the focal length was approximately 97 cm, in this case, and the laser energy was 62 joules, equation 6 determines the peak laser intensity to be $q_{\text{max}} \approx 3.6 \times 10^7$ watts/cm². Under these near-threshold conditions, one can clearly observe LSD waves being ignited from isolated spots within the focal diameter rather than from the entire focal pattern as reported in reference 24.

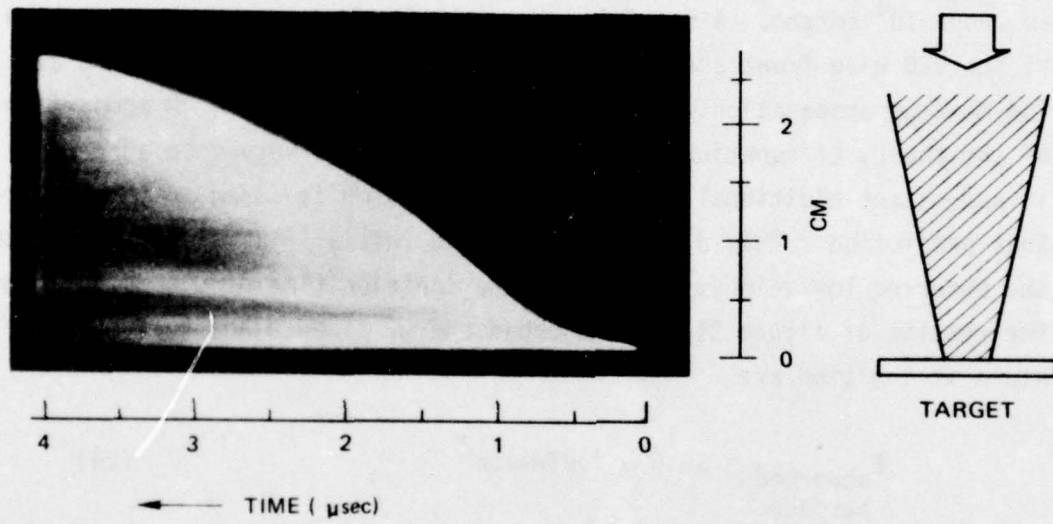


Figure 20. Streak Photograph of the First 4 μsec of an LSD Wave Formed by a 64-J HF Laser Pulse Focused to 0.4 cm Diameter Spot on Aluminum 6061 Alloy

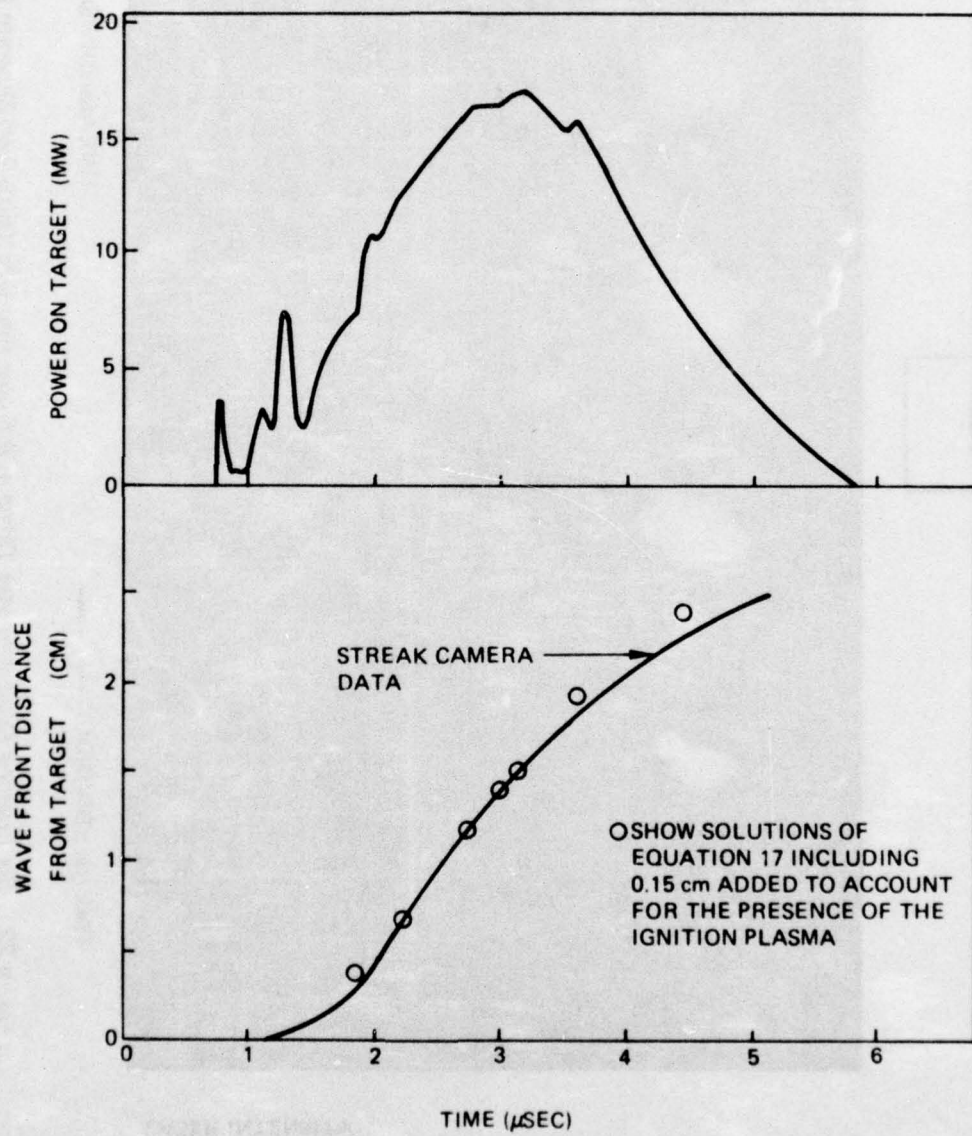


Figure 21. HF Laser Pulse Amplitude, and LSD Wave Front Position, Plotted On the Same Time Scale

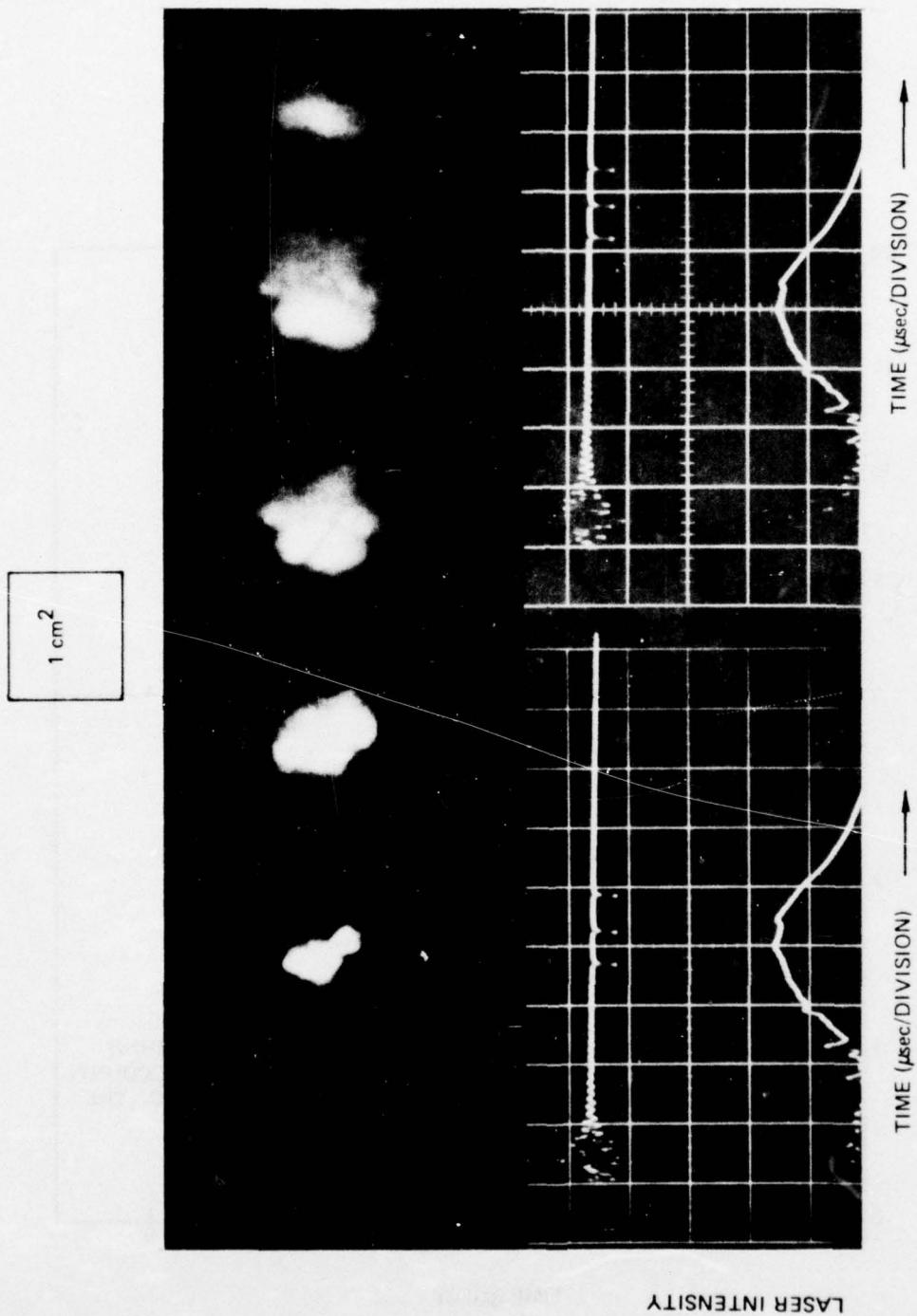


Figure 22. Six Framing Camera Images Taken at 0.5 μsec Intervals, Using Two Separate Laser Shots. The Plasma is Viewed Along the Beam Direction to Show Radial Development of LSD Waves. Oscillograms Show Framing Camera Image Times Relative to Laser Pulse Time Profile.

2. Spectroscopic Studies of Laser-Supported Absorption Waves at
2.8 Microns

In order to study some of the features of laser-supported detonation (LSD) waves as described previously a limited series of time-integrated emission spectra were recorded with a Hilger-Watts quartz spectrograph in a way similar to that used in previous experiments using a pulsed CO₂ laser (Refs. 24, 25). In addition, a near-normal incidence, 1 - meter concave-grating monochromator (McPherson model 225) was also used to determine the temporal behavior of selected spectral lines.

Figure 23 shows three sections of the spectra observed at 4 mm in front of an Al plate target. With laser pulses of 43 J and 34 J (total target energy), the spectrum is dominated by N⁺ and O⁺ lines superimposed on a strong continuum. These lines are more broadened by the Stark Effect than in similar spectra generated by CO₂ radiation (Ref. 25). In contrast to the air species, atomic lines from Al are narrow and weak. At 21 J, Al lines are the only emission feature recorded which indicates a threshold for the air breakdown. Another shot at 11 J did not produce enough light to be recorded.

In addition to the line-spectra which are very prominent in the spectra of laser-supported absorption (LSA) waves, a large amount of continuum radiation is also emitted. A wavelength near 5450 Å is in such a range that no nearby lines are found. With a quartz lens focussed at distances z in front of the target surface, light emitted within a thin slice of space at z can be imaged onto the entrance slit of the monochromator. Figure 24 shows some typical traces of the continuum observed at several distances. When the quartz lens is removed, the solid angle subtended by the monochromator is wide enough to monitor the entire spark including z=0. A laser pulse shape detected by a liquid-N₂ cooled Au-Ge detector is also shown in figure 24. The oscilloscope sweeps were synchronously triggered by the current signal of the Xe flashlamp. The arrows indicate the onsets of light emission.

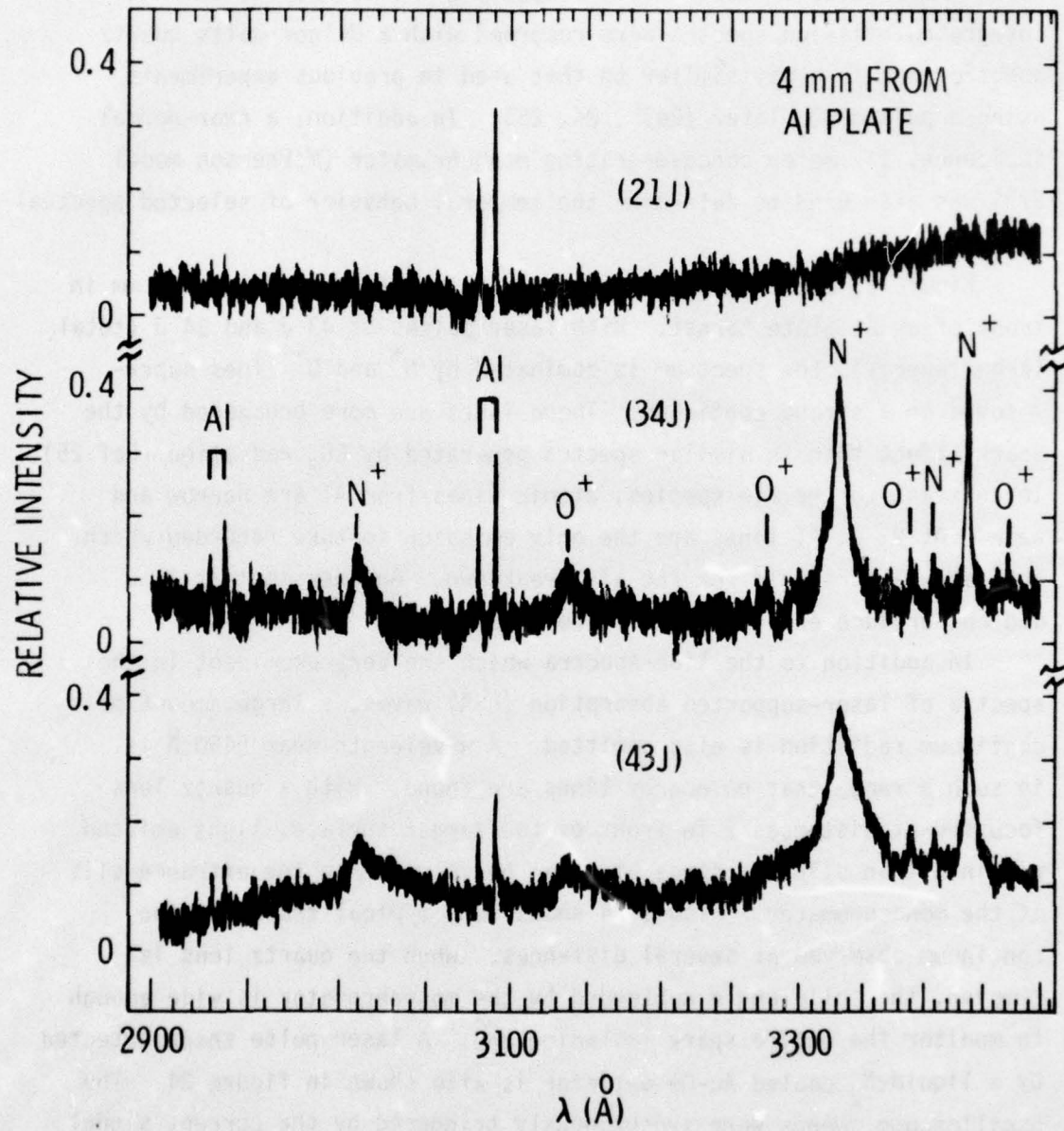


Figure 23. Sections of the Emission Spectra Observed at 4mm in Front of an Al-plate Target. The HF Laser Total Target Energy Is Indicated in the Parentheses.

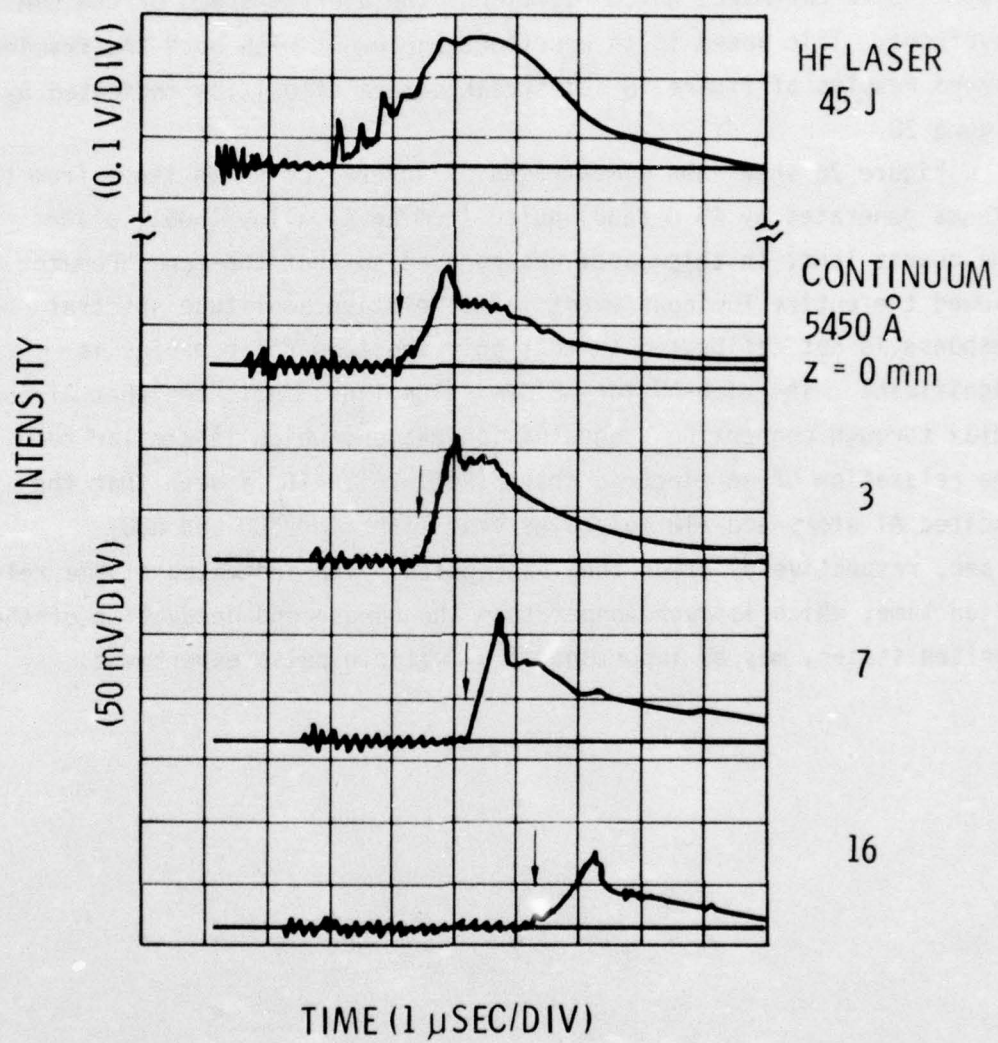


Figure 24. The LSA V-wave Continuum Emission Observed at Several Distances in Front of the Target. The Arrows Designate the Onset of Light. A Laser Pulse Shape Is Included for Comparison.

The correlation of distance and time is summarized in figure 25. The possible errors in the experiments are indicated by the crosses. It is seen that the datum points may be fitted by a straight line of slope = $0.72 \text{ cm}/\mu\text{sec}$, which represents the average speed of the LSA wavefront. This speed is in excellent agreement with both the framing camera results of figure 18 and streak camera velocities indicated by figure 20.

Figure 26 shows the time-traces of several emission lines from the plasma generated by 45 J ($\pm 3J$) pulse from an Al alloy (6061) plate. The quartz lens, in this case, was removed so that the monochromator viewed the entire luminous event. The relative amplitude spectral response is not calibrated so that only the temporal behavior is significant. The time-history of emission lines indicates that Al ions relax through connecting stages of ionization, which is similar to the relaxation of an electric spark (Ref. 26). It is seen that the excited Al atoms and Al₂O molecules emit light for 600 and 800 μsec , respectively, after the laser pulse. The indicated plasma relaxation time, which is much longer than the nanosecond decay time of the excited states, may be important in a multiple-pulse experiment.

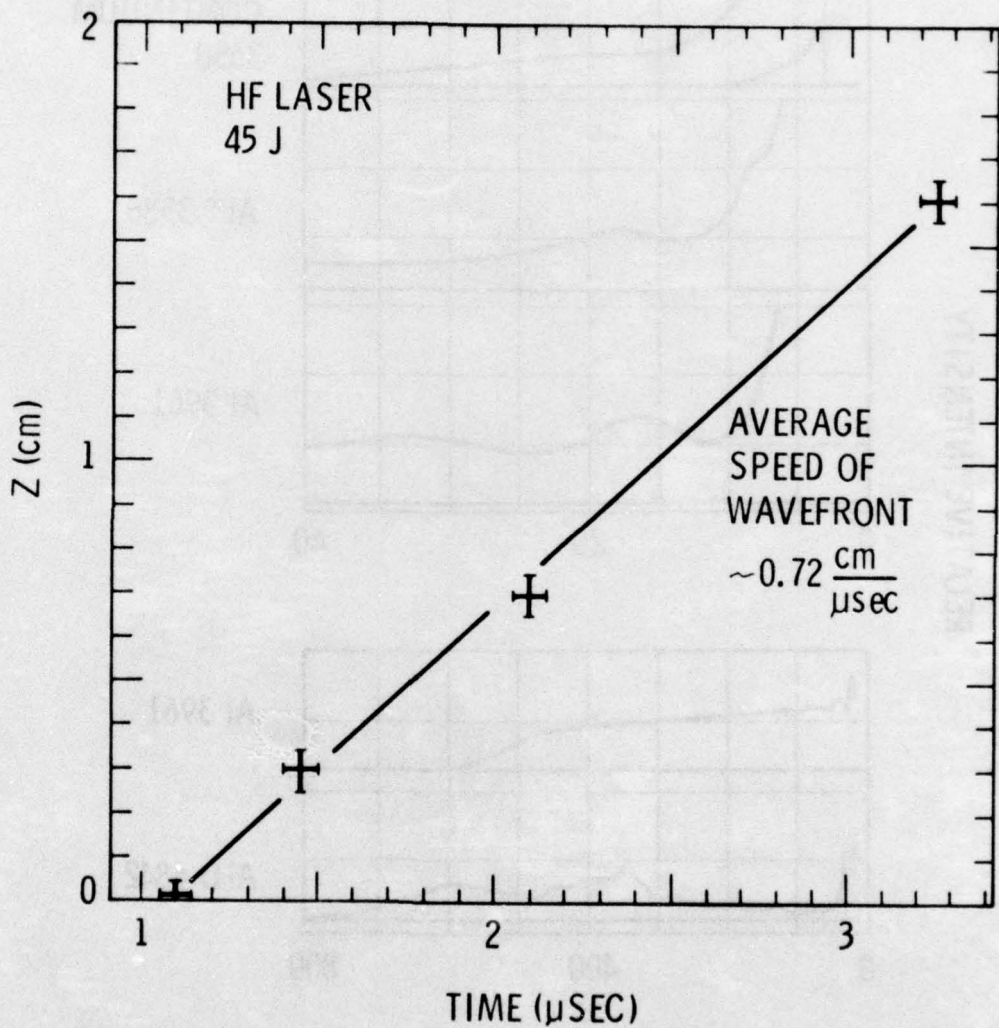


Figure 25. A Correlation of the Distance and Time for the LSA Wavefront.
An Average Speed is Obtained From the Slope of a Straight-Line Fit.

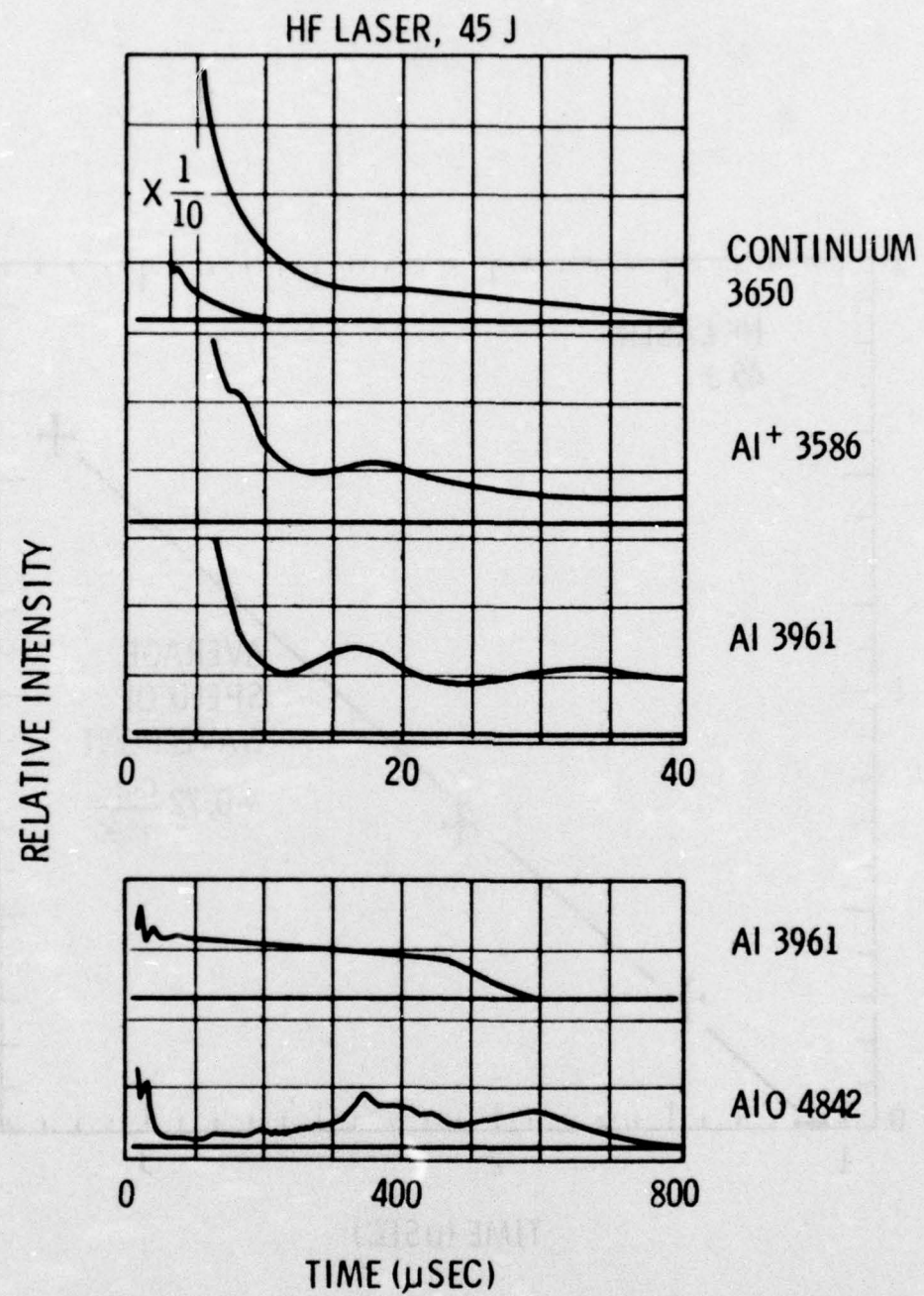


Figure 26. Temporal Behavior of 4 Kinds of Emission Lines From the Plasma Produced by a 45-J Pulse from an Al-Plate

3. IGNITION THRESHOLDS OF LSA WAVES PRODUCED BY HF LASER RADIATION

Apart from the propagation and the characteristics of well-established LSD and LSA waves resulting when a pulsed laser beam interacts at a target surface, the ignition phenomenon itself is of considerable interest. A variety of measurements has been reported giving thresholds for such ignition at various surfaces, particularly for the 10.6 micron radiation from CO₂ lasers (Ref. 1). Ambiguities in the definition of these thresholds have previously been discussed (Ref. 28) and any definition must be reduced to a statement of what experimental result is to be interpreted as the onset of an LSA wave.

Conventional parameters used to report LSA ignition thresholds are total laser pulse fluence e_t (in J/cm²) and peak laser pulse irradiance q_p (in W/cm²). A deficiency in this specification arises from the fact that however threshold is defined, it is observed to occur at various times during the incident laser pulse. Two problems are then apparent with the conventional specification. First, threshold typically occurs earlier in time than the peak of the laser intensity time profile (Refs. 24, 28). This means that the peak irradiance, q_p , to be associated with a given threshold is a strong function of the laser pulse profile being used, particularly when the threshold occurs very early in the pulse, since a peak in laser intensity cannot directly affect the onset of a threshold which occurred earlier in time. Secondly, measurements presented here as well as elsewhere show that early and late occurrence of threshold within the laser pulse are associated with very different values of e_t and q_p ; higher e_t and q_p move the threshold to earlier times within the laser pulse. The values of e_t and q_p to be associated with a given threshold are uniquely determined only if the time of threshold occurrence within the laser pulse is specified.

For the present data, quantities given in addition to e_t and q_p for each threshold are the integrated fluence to ignition e_i (in J/cm²) and irradiance at the time of ignition q_i (in W/cm²). The maximum irradiance achieved up to threshold time t_a is q_p if ignition time t_i

is greater than the laser peak time t_p , and $q_a = q_i$ if $t_i < t_p$. The measured fraction f_i of laser pulse energy occurring before ignition is also listed.

We here present data on LSA wave ignition thresholds as derived from two definitions: (1) plasma luminosity as observed by streak photography, and (2) cutoff of the incident laser radiation transmitted through a pinhole in the target. Most of the present results derive from the second method. A luminosity threshold is measured by observing streak camera data (such as that of figure 20) near the lowest laser energy for which a luminous front is observed to develop toward the incoming laser beam. In this case the time of first observable luminosity is designated the ignition time t_i . A pinhole transmission threshold is measured by simultaneously recording the full laser pulse and the pulse transmitted through a 0.4 mm target pinhole, as illustrated in figure 27. The two traces are from two similar Ge(Au) detectors; one records the total laser pulse as sampled by a CaF_2 wedge, and the other observes radiation through the pinhole. Throughout these measurements, a new target was used for each laser shot. The time at which the transmitted intensity falls to 50% of the value expected from the complete pulse is designated t_i , and the fraction of total pulse energy (or fluence) occurring before t_i is f_i .

Results of threshold measurements are given in Tables 3 - 6. These tables are all arranged with similar headings. The "nominal attenuator setting" refers to the expected fractional transmission (by area) of the sector attenuator discussed in II.9 "Energy into spot" is the energy within the central high-intensity zone of the spatial profile discussed in II.5 and can be seen to be nearly proportional to the attenuator settings. The remaining quantities in the tables have been discussed above. The data presented in the tables are the results of single measurements on clean targets.

Table 3 is a direct comparison of 2.8-micron luminosity thresholds on aluminum for two target spots differing by about a factor of 10 in area. The target spots were produced with collecting-mirrors

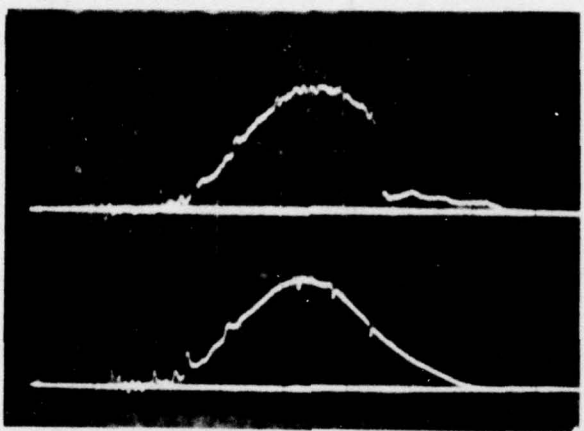


Figure 27. Time Profile for HF Laser Pulse Transmitted Through a Stainless 321 Target Pinhole (Upper) Compared to the Complete Laser Pulse (Lower). For This Case Pinhole Transmission was Cut Off When the Integrated Fluence Reached 82% of the 46-J/cm^2 Total.

TABLE 3
LUMINOSITY THRESHOLDS FOR IGNITION OF LSA WAVES ON ALUMINUM

Spot Diam. (cm)	Nominal Atten. Setting (% transm.)	e_t Energy into Spot (J)	q_p Total Pulse fluence (J/cm ²)	f_i Peak Irradiance (MW/cm ²)	e_i Fluence to Ignition (J/cm ²)	q_i Irradiance at Ignition (MW/cm ²)
0.4	6%	3.7	28	10	50%	14
1.3	100%	63	48	19	50%	24

A 2.8 MICRON HF LASER PULSE WAS INCIDENT ON ALUMINUM 6061 FOR TWO FOCAL SPOT SIZES. ALL THRESHOLD DATA ARE FOR PREVIOUSLY UNEXPOSED TARGETS.

TABLE 4
LARGE SPOT PINHOLE TRANSMISSION THRESHOLDS FOR IGNITION OF LASER
WAVES ON THREE METALS

Material	Energy into Spot (J)	e_t Total Pulse Fluence (J/cm ²)	q_p Peak Irradiance (MW/cm ²)	f_i % to Ignition	e_i Fluence to Ignition (5)% (J/cm ²)	q_i Irradiance at Ignition (MW/cm ²)
SS 321	61	46	24	82%	38	14
Al 6061	67	50	26	77%	39	19
Ti	61	46	28	42%	19	26

HF LASER RADIATION FOCAL SPOT DIAMETER OF 1.3 CM.

TABLE 5
SMALL SPOT PINHOLE TRANSMISSION THRESHOLDS FOR IGNITION
OF LSA WAVES ON THREE METALS

Material	e_t Energy into Spot (J)	q_p Total Pulse Fluence (J/cm ²)	f_i % to Ignition	e_i Fluence to Ignition (J/cm ²)	q_i Irradiance at Ignition (MW/cm ²)
Al 6061	35	177	55	.5	24
	16.5	84	26	12	18
	8.7	44	14	14	14
SS 321	4.3	22	7	>100%	-
	34	173	54	7	25
Titanium	8.1	41	13	12	13
	17	84	26	12	19
	8.7	44	14	10	13

THE ELLIPTICAL FOCAL SPOT HAD DIMENSIONS 0.4 CM X 0.6 CM OR NOMINAL DIAMETER OF 0.5 CM.

TABLE 6
LSA IGNITION THRESHOLDS FOR THREE NONMETALS

Material	Energy Into Spot (J)	e_t Total Pulse Fluence (J/cm ²)	q_p Peak Irradiance (MW/cm ²)	f_i % to Ignition	e_i Fluence to Ignition (J/cm ²)	q_i Irradiance at Ignition (MW/cm ²)
Lucite	33	169	53	30%	51	51
	28	144	45	44%	65	45
Lexan	16	80	25	58%	46	25
	34	170	53	18%	31	47
	16	81	25	56%	46	25
Teflon	16	81	25	53%	43	25
	2.0	10	3.2	>100%	-	0
	28	144	45	41%	59	45
	12	62	19	>100%	-	-

PINHOLE OR TARGET TRANSMISSION TECHNIQUES USED TO MEASURE IGNITION OF LSA WAVES BY HF LASER RADIATION. THE ELLIPTICAL FOCAL SPOT HAS DIMENSIONS 0.4 CM X 0.6 CM OR NOMINAL DIAMETER OF 0.5 CM.

of focal lengths 123.2 cm and 37.5 cm using a symmetric eight-lamp laser configuration so that the relative spatial profile of figure 9 applies to both spot sizes. Threshold occurred near the laser pulse peak in both cases, so $q_i \approx q_p$. The indicated thresholds show a higher fluence (and peak intensity) for the larger spot diameter. This behavior is contradictory to previous experience since small spot thresholds are usually larger than large spot thresholds.

Table 4 is a comparison of pinhole transmission thresholds for aluminum, stainless steel, and titanium, under the large spot conditions of Table 3, with no beam attenuation. The stainless steel data of Table 4 are those of figure 27. Using the energy fluence to threshold, e_i , as a parameter, we see that the titanium threshold is about half that of aluminum, and the stainless steel threshold is equal to that of aluminum. The aluminum value e_i (transmission) = 39 J/cm^2 may be compared for the same spot diameter to e_i (luminosity) = 24 J/cm^2 from Table 3. Threshold differences have been previously observed at CO_2 wavelength between luminosity and plasma-transmission thresholds (Ref. 26). At 10.6 micron, luminosity thresholds were generally larger than thresholds obtained by plasma transmission measurements. This lowering of the luminosity threshold compared to the transmission threshold is probably related to the shorter 2.8 micron wavelength. Since plasma absorption coefficients increase as the square of wavelength (a factor of 14.3), one expects the plasma cutoff condition to be more difficult at short wavelengths. From Table 4 the highest irradiance before ignition q_a was 24 MW/cm^2 for stainless steel and 26 MW/cm^2 for aluminum and titanium.

Tables 3 and 4 contain data taken using the uniform and symmetric focal spots of an eight-lamp laser installation. Tables 5 and 6 give data taken using four lamps with an elliptical focal spot, as discussed in II.5, having dimensions 0.4 cm x 0.6 cm. or a nominal diameter of 0.5 cm. Table 5 shows small-spot thresholds for the same metals as Table 4. Here we show examples, for each target, of measurements with laser pulses of decreasing magnitudes, resulting in a progression of the threshold event in time to various points within the total pulse

length, and hence to various fractions f_i of the total pulse energy. This is best seen in the aluminum data, which include four pulse energies.

It is clear that a single threshold parameter which is independent of the details of the laser pulse time profile -- a function of the material and the wavelength only -- would be extremely useful. A previous study of breakdown time on aluminum targets as a function of CO₂ laser pulse peak power density led to the conclusion (Ref. 24) that "energy deposition prior to breakdown" was a constant, but that the power density (irradiance) achieved up to breakdown time was not a constant. In our case, this would imply a constant e_i . In the aluminum data of Table 5, however, as pulse irradiance is lowered, the time required for ignition increases more than that required for constant integrated energy, and e_i is observed to increase by a factor of 3 as ignition times increase. At this point neither e_i nor peak irradiance achieved up to ignition time q_a appear to be satisfactory invariants in our threshold measurements.

The anomalous spot size effect mentioned previously can be seen again by observing that the largest aluminum e_i of Table 5 (for spot diameter $d_s = 0.5$ cm) is 14 J/cm² while the aluminum e_i of Table 4 for $d_s = 1.3$ cm) is 39 J/cm². A similar comparison of e_i for stainless steel and for titanium between Tables 5 and 6 can be made and one finds that the larger spot diameter requires larger e_i for ignition.

Table 6 gives thresholds for three non metals. For these materials the cutoff illustrated by figure 27 occurred over a longer time than for the metallic samples, resulting in somewhat increased uncertainty in the value of f_i and hence e_i . The lucite sample pinholes were similar to those of the metal samples. For the lexan and teflon targets, however, it was observed that, below threshold, the laser pulse was transmitted through the sample without shape distortion and with such intensity that target pinholes were not needed. These targets nevertheless displayed transmission cutoff by the plasma formed at LSA ignition.

In order to make some comparison with previous CO₂-wavelength threshold results, selected e_t and q_p are taken from Tables 5 and 6 and tabulated in Tables 7 and 8 along with 10.6 micron results (Ref. 28) As discussed above, such a comparison is indirect because of the threshold dependence on laser pulse shape. Those results (Ref. 28) were for a nominal pulse width of 20 μ sec compared to the present HF pulse width of about 4 μ sec. It is nevertheless of interest to tabulate the lowest pulse energy requirements for threshold for this particular HF laser and this particular CO₂ laser. For each target material, the e_t and q_p selected from the present 2.8 micron work corresponds to the lowest-energy pulse for which threshold was observed, since a similar procedure produced the corresponding 10.6 micron data. Table 7 indicates that similar peak irradiances are required for LSA wave ignition for both HF and CO₂ wavelengths. Table 8, however, shows that the required HF total pulse fluence is lower than the CO₂ total pulse fluence for every material listed; a factor of 4 difference is observed for titanium. This effect cannot be attributed to wavelength, since a difference is expected in e_t, in the direction observed, because threshold typically occurred relatively earlier in the CO₂ laser pulse than in the HF laser pulse; the CO₂ pulse was also much longer. In addition, the 10.6 micron experiments were performed with a focal area which was four times smaller than the 2.8 micron wavelength experiments.

4. IMPULSE MEASUREMENTS WITH HF LASER RADIATION

Six materials were examined for the impulse loads applied by HF laser beam interactions. These materials were three metals: 6061 aluminum, titanium, and 304 stainless steel; and three insulators: teflon, lexan, and lucite. The materials were prepared in the form of disks of diameters 0.79 cm, 0.95 cm, 1.27 cm, and 2.59 cm. All of these were weighed and their weights added to the weight of the adapted moving element of the Trans-Tek Model 100-000 Linear Velocity Transducer (LVT). Impulse could be measured because the total moving mass was known and the peak velocity could be measured from the calibrated voltage output

TABLE 7

COMPARISON OF THRESHOLD VALUES OF LASER PULSE
 PEAK IRRADIANCE q_p FOR 2.8 MICRON AND 10.6
 MICRON RADIATION

Wavelength:	2.8 μ	10.6 μ	10.6 μ
Diagnostic:	Trans	Lum	Reflec
Spot Diam:	0.5 cm	0.25 cm	0.25 cm
Al 6061	14	-	-
Al 7075		25	11
Titanium	14	-	23
Lucite	25	37	-
Lexan	25	-	40
Teflon	45	-	28

THE 10.6 MICRON DATA ARE FROM REFERENCE 28. THE THRESHOLD DIAGNOSTIC PROCEDURES ARE SPECIFIED AS TRANS = PLASMA TRANSMISSION BY PINHOLE OR TARGET TRANSMISSION, LUM = LUMINOSITY VIA IMAGE CONVERTER PHOTOGRAPHY, AND REFLEC = PLASMA TRANSMISSION VIA SPECULAR TARGET REFLECTION. THE VALUES OF q_p ARE GIVEN IN MW/cm².

TABLE 8
COMPARISON OF THRESHOLD VALUES OF LASER PULSE TOTAL
FLUENCE e_t FOR 2.8 MICRON AND 10.6 MICRON RADIAITON

Wavelength:	2.8 μ	10.6 μ	10.6 μ
Diagnostic:	Trans	Lum	Reflec
Spot Diam:	0.5 cm	0.25 cm	0.25 cm
Al 6061	44	-	-
Al 7075	-	176	75
Titanium	44	-	160
Lucite	80	258	-
Lexan	81	-	280
Teflon	144	-	195

THE 10.6 MICRON DATA ARE FROM REFERENCE 28. THE THRESHOLD DIAGNOSTIC PROCEDURES ARE SPECIFIED AS "TRANS" = PLASMA TRANSMISSION BY PINHOLE OR TARGET TRANSMISSION, "LUM" = LUMINOSITY VIA IMAGE CONVERTER PHOTOGRAPHY, AND "REFLEC" = PLASMA TRANSMISSION VIA SPECULAR TARGET REFLECTION. THE VALUES OF e_t ARE GIVEN IN J/cm^2 .

of the LVT. A mechanical impulse setup was used to calibrate the device for 0.60 cm of available travel and the calibration agreed with the manufacturer's typical value. Error is within $\pm 5\%$.

a. Impulse produced on Metal Targets

All of the data collected with metal targets in the HF beam are similar. The focal spot size of the 37.5 cm focal length mirror was approximately (4 x 6 mm) elliptical in shape as discussed above. In figure 28, the I/E values for aluminum disk targets are observed to produce reproducible data (within 15%) at each diameter. The impulse I is in dyne-sec while E is the total incident laser energy, in joules, on the target. The dashed line shows an r^2 relationship fitted at the average I/E at 1.6 cm. As derived by Pirri (Ref. 29) the actual variation of impulse with target radius can show various dependences depending on the ratio of target radius to focal spot radius. This complex behavior results from the dynamics of the spreading laser-produced blast wave over the surface. For a ratio of target area to focal spot area A_t/A_s such that $1 < A_t/A_s < 3$. Pirri's results lead to (approximately)

$$I/E = \left[-1.05 + 6.62 A^{-71} \right] C \quad (25)$$

where C is an underdetermined constant. The form given by equation 25 is restricted to the indicated range of target areas. It is obvious that when the target size becomes very large that impulse generation is independent of r . This impulse increase with target area has also been reported in reference 30.

Figures 29 and 30 show the corresponding impulse production with titanium and stainless steel targets respectively. These targets, which are much more severely melted than is aluminum, again show a nearly identical variation of impulse with target area. These results indicate that target vaporization is a negligible factor in the measured impulse on these targets in atmospheric pressure air.

The energy range in the above measurements was varied only over a narrow range: for aluminum $18 < E < 39$ joules, for titanium $36 < E < 40$ joules, and for stainless steel, $35 < E < 40$ joules.

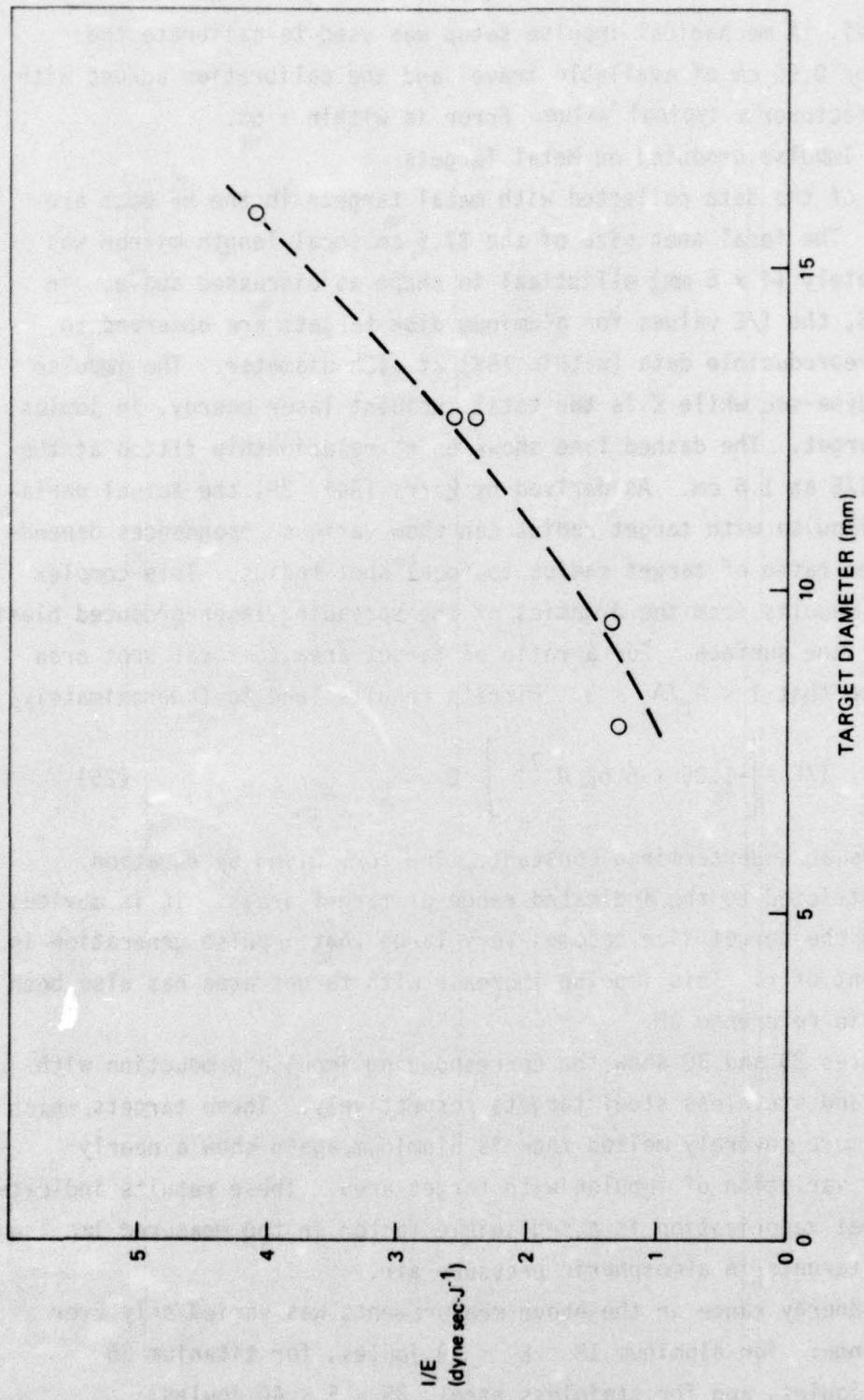


Figure 28. I/E Values Shown as a Function of Target Diameter for Aluminum at 2.8μ

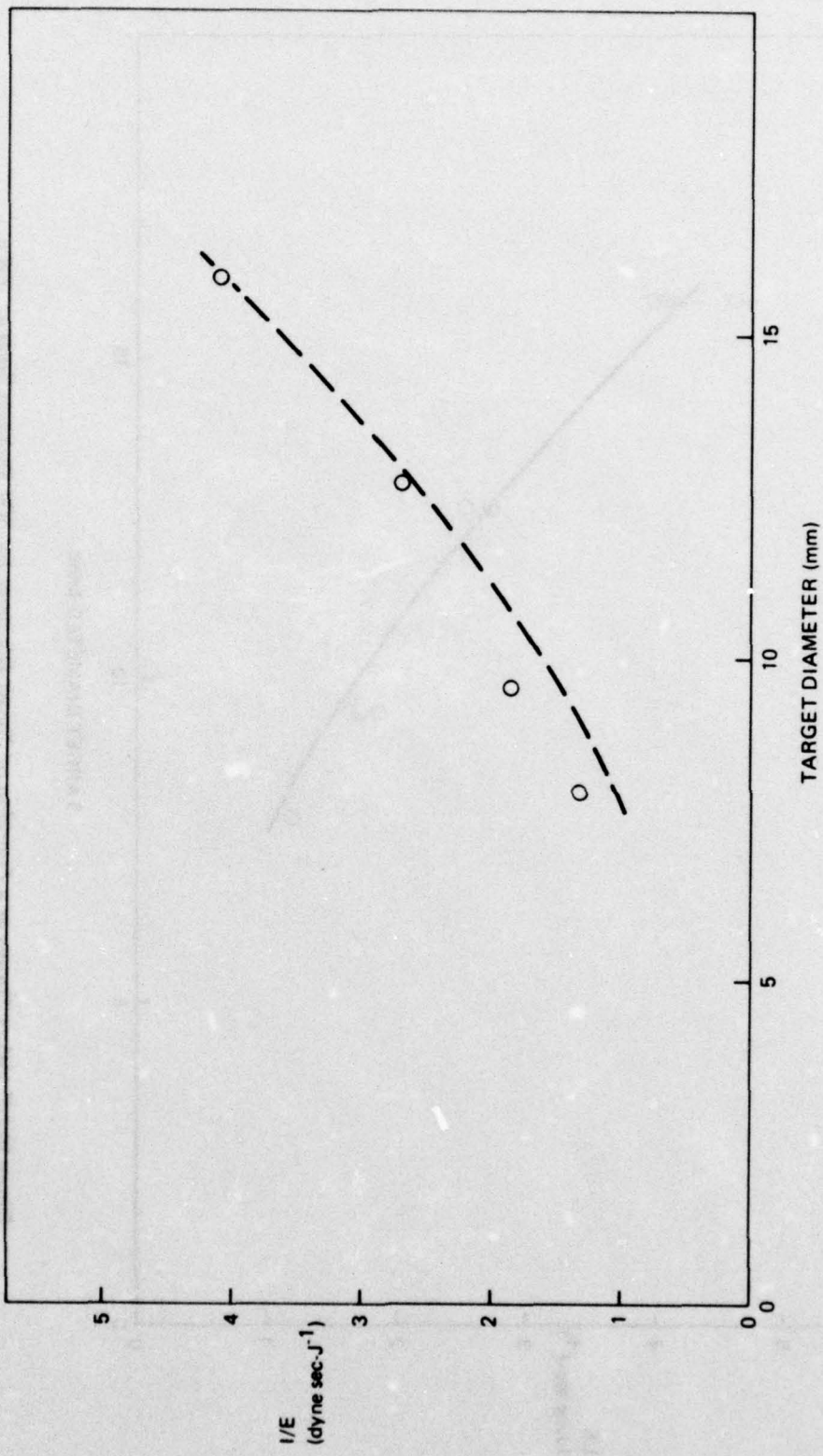


Figure 29. I/E Values Shown as a Function of Target Diameter for Titanium at 2.8μ

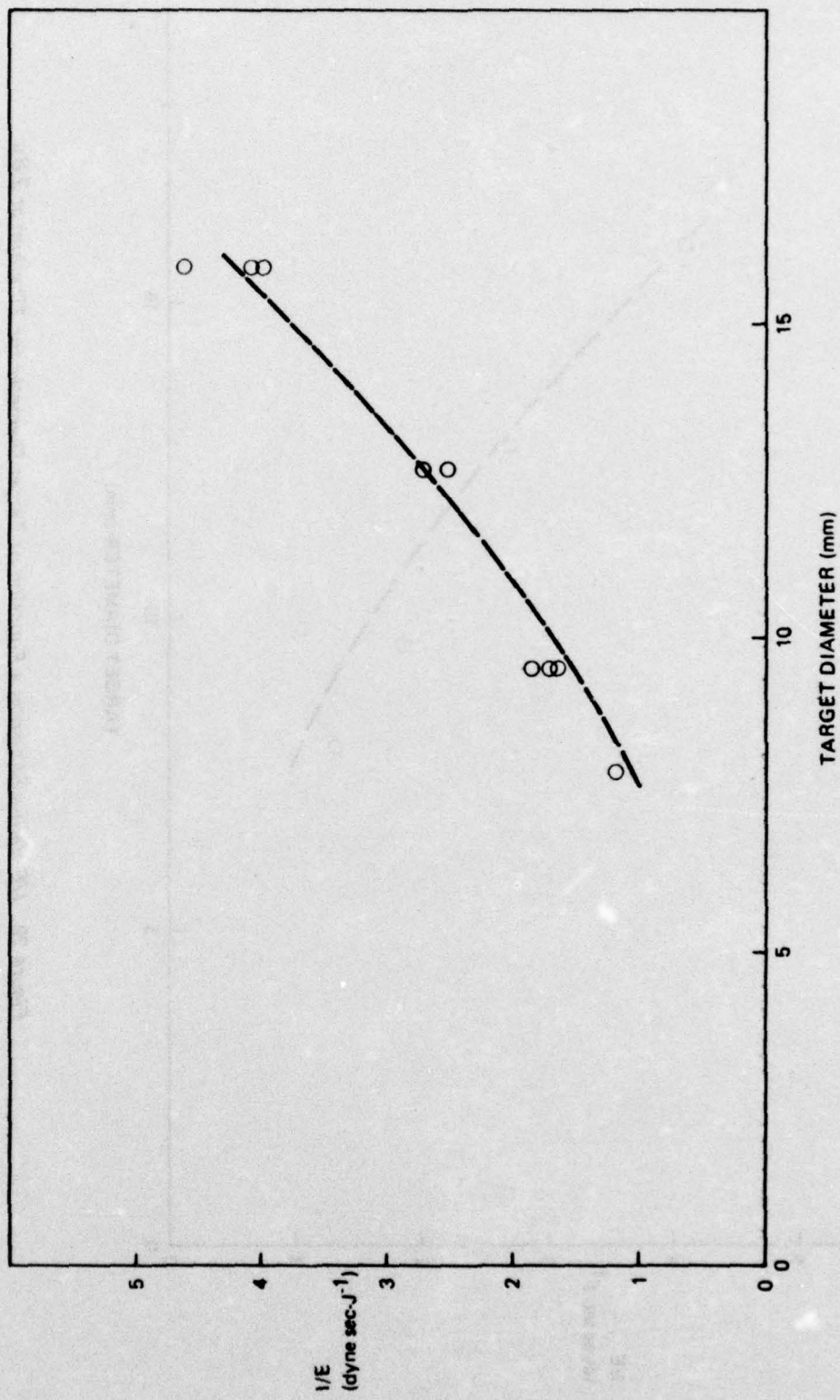


Figure 30. I/E Values Shown as a Function of Target Diameter for 304 Stainless Steel at $2.8\ \mu$

b. Impulse Production With Insulator Targets

Various ablative materials were tested for total impulse production. These included teflon, lexan, and lucite. No impulse was measurable with teflon, however, since it was found to be nearly completely transparent to 2.8 micron wavelength radiation. The only apparent damage to 0.2 cm thick teflon targets was an observed internal series of breakdown pits.

The variation with target diameter of impulse for lexan targets is shown in figure 31. With these ablating targets, an appreciable contribution to the impulse is produced by the vaporizing target material itself. At the high energies used, $20 < E < 37$ joules, however, the LSD wave threshold is considerably exceeded and the dominant impulse-producing mechanism is still the laser-produced air blast wave.

Figure 32 shows the variation with target diameter of impulse on lucite targets. In this case, the laser energy was varied in the range $35 < E < 38$ joules. The observed slight decrease in impulse with target area is believed to result from the near threshold conditions for the production of LSD waves. Further experiments on lucite targets are necessary, however, in order to obtain a clearer understanding of the important phenomenology.

5. THERMAL COUPLING OF PULSED 2.8 MICRON RADIATION TO METAL TARGETS

It is evident that one of the most important aspects of laser effects studies is a determination of the reflectivity of targets as a function of laser intensity. The laser absorptivity is, generally speaking, nearly constant and independent of laser intensity for laser intensities below the plasma-production threshold discussed in section III.3. When laser-supported absorption waves (or plasma conditions) are produced, however, the net absorption coefficient has been observed to greatly increase. Rudder (Ref. 31) has measured the coupling coefficients of 5 and 10.6 micron laser radiation. In all cases, the coupling coefficient has been observed to increase, with reflective targets, when plasma is ignited at the surface. Rudder shows that no enhanced coupling behavior is found (or expected) for materials with an intrinsic absorptivity greater than approximately 25%.

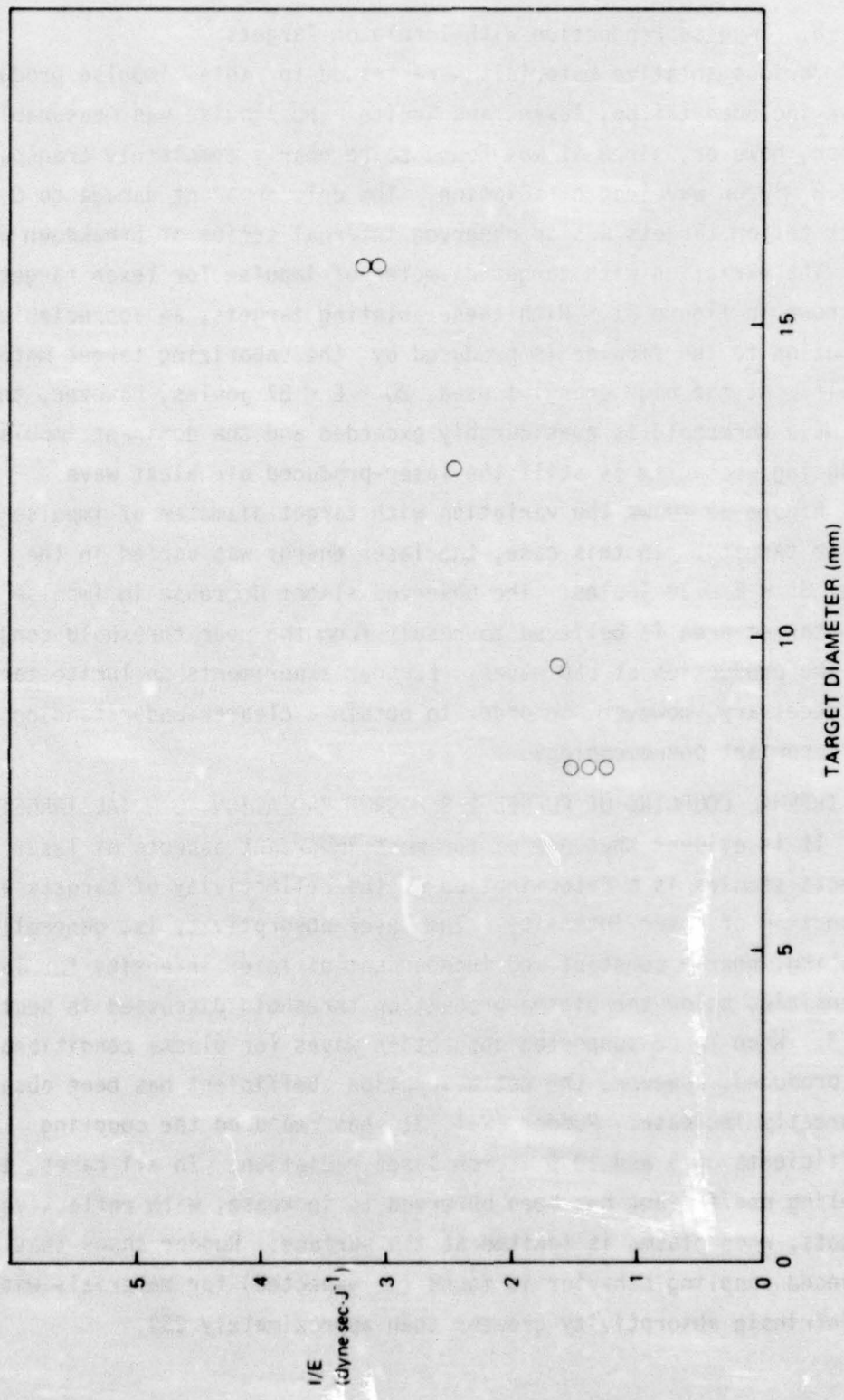


Figure 31. I/E Values Shown as a Function of Target Diameter for Lexan at 2.8 μ

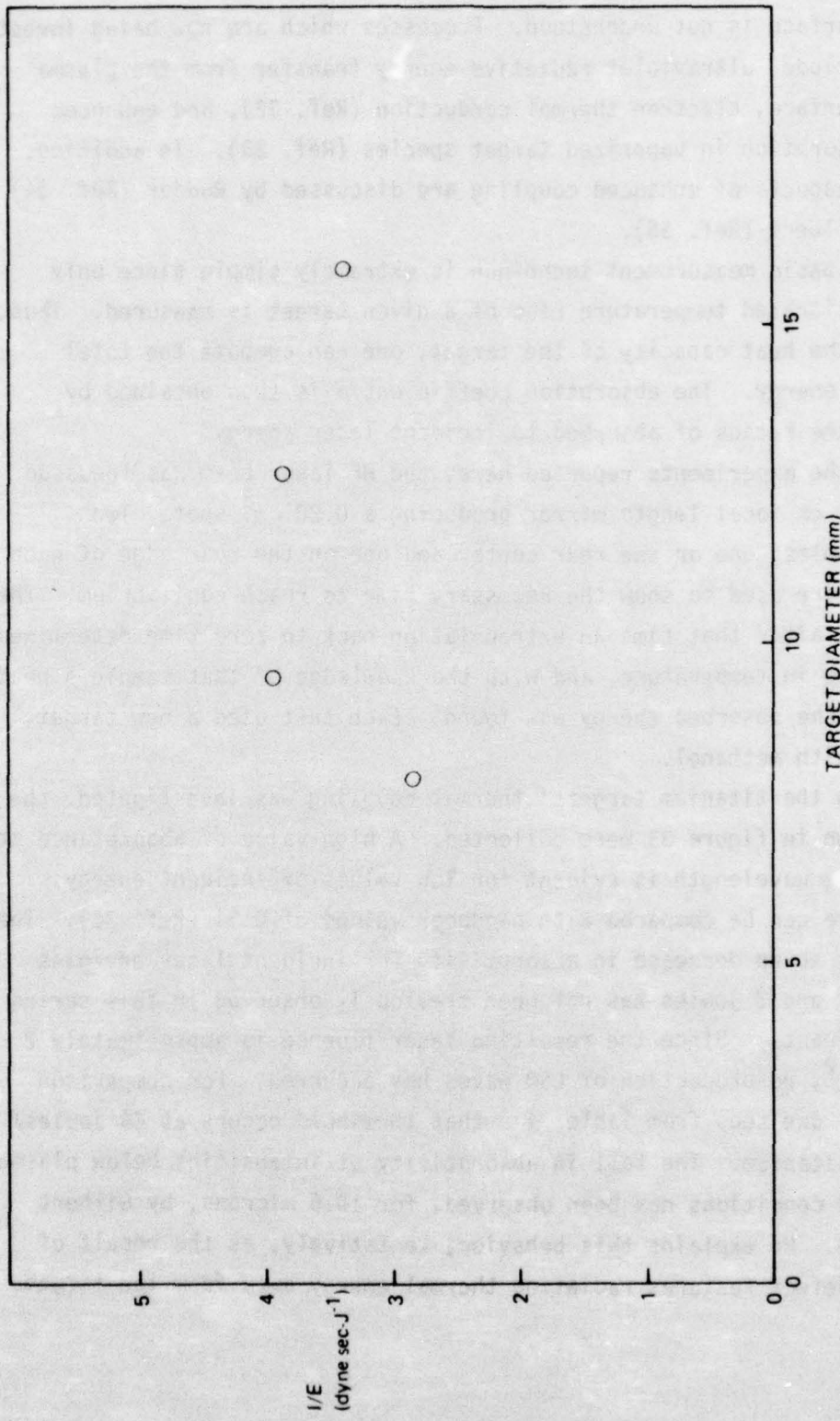


Figure 32. I/E Values Shown as a Function of Target Diameter for Lucite at 2.8μ

At the present time, the exact energy transfer process to the target surface is not understood. Processes which are now being investigated include ultraviolet radiative energy transfer from the plasma to the surface, electron thermal conduction (Ref. 32), and enhanced laser absorption in vaporized target species (Ref. 33). In addition, various aspects of enhanced coupling are discussed by Rudder (Ref. 34) and by Gilbert (Ref. 35).

The basic measurement technique is extremely simple since only the equilibrated temperature rise of a given target is measured. Thus, knowing the heat capacity of the target, one can compute the total absorbed energy. The absorption coefficient α is then obtained by forming the ratios of absorbed to incident laser energy.

In the experiments reported here, the HF laser beam was focussed by a 37.5 cm focal length mirror producing a 0.20 cm^2 spot. Two thermocouples, one on the rear center and one on the rear edge of each sample, were used to show the necessary time to reach equilibrium. Then from data after that time an extrapolation back to zero time determined the change in temperature, and with the knowledge of that sample's heat capacity the absorbed energy was found. Each test used a new target, cleaned with methanol.

When the titanium targets' thermal coupling was investigated, the data shown in figure 33 were collected. A high value of absorptance at this 2.8μ wavelength is evident for low values of incident energy. This curve can be compared with handbook values of 0.34 (Ref. 36). The extremely sharp decrease in absorptivity for incident laser energies between 1 and 2 joules has not been previously observed in this series of experiments. Since the resulting laser fluence is approximately 2 joules/ cm^2 , no production of LSD waves has occurred. For comparison purposes one sees from Table 8 that threshold occurs at 44 joules/ cm^2 for titanium. The fall in absorptivity at intensities below plasma threshold conditions has been observed, for 10.6 microns, by Gilbert (Ref. 35). He explains this behavior, tentatively, as the result of surface defect features radiating thermal energy away from the target surface.

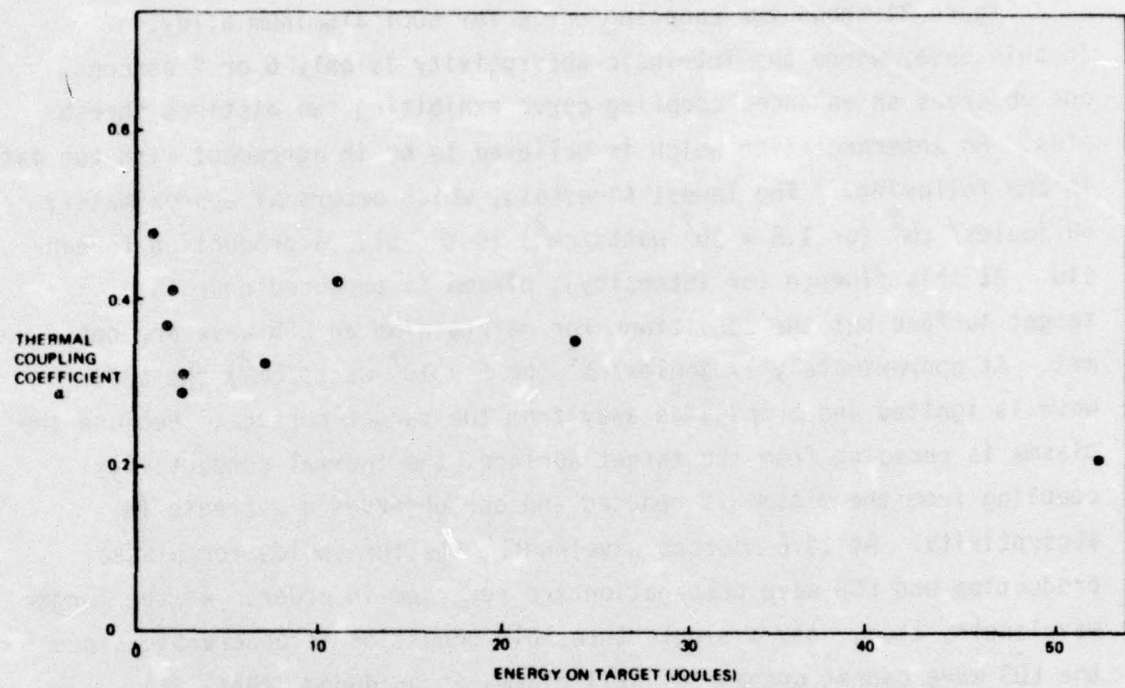


Figure 33. Thermal Coupling Coefficient as a Function of HF Laser Beam Energy for 1.6 CM Diameter Titanium Targets. A New Target was Used for Each Data Point. Beam Spot Area was 0.20 CM².

Figure 34 shows the coupling curve for 6061 aluminum alloy. In this case, where the intrinsic absorptivity is only 6 or 7 percent, one observes an enhanced coupling curve exhibiting two distinct thresholds. An interpretation which is believed to be in agreement with the data is the following. The lowest threshold, which occurs at approximately 50 joules/cm² (or 1.8×10^7 watts/cm²) is the plasma production threshold. At this fluence (or intensity), plasma is produced near the target surface but the conditions for maintaining an LSD wave are not met. At approximately 17 joules/cm² (or 5×10^7 watts/cm²) the LSD wave is ignited and propagates away from the target surface. Because the plasma is receding from the target surface, the thermal conductivity coupling from the plasma is reduced and one observes a decrease in absorptivity. At 10.6 microns wavelength, the thresholds for plasma production and LSD wave propagation are reversed in order. At the longer wavelength, then, only a single threshold condition is observable since the LDS wave cannot propagate until plasma is produced (Ref. 31).

6. INTERFEROMETRIC DIAGNOSTICS OF EFFECTS PRODUCED BY HF LASER RADIATION

Interferometry of laser-supported detonation waves (LSD waves) and the resulting gas dynamic disturbances has previously produced a considerable amount of laser effects information (Ref. 37). These data have shown the propagation of shock waves, vaporization of target material, and have led to estimates of electron densities at the target surface (Ref. 30). In addition, optical diagnostics have value in examining the ignition processes of LSD waves. At the present time, however, the full potential of interferometric diagnostics has yet to be realized.

In the experiments reported herein only a single wavelength interferometer has been utilized. This situation makes it impossible to unambiguously determine the concentrations of both neutrals and ionized species. This arises because the measured index of refraction is a sum of contributions of both electrons and neutral species. A better experimental approach would be to take interferometric data at two laser wavelengths simultaneously. Since the frequency dependence

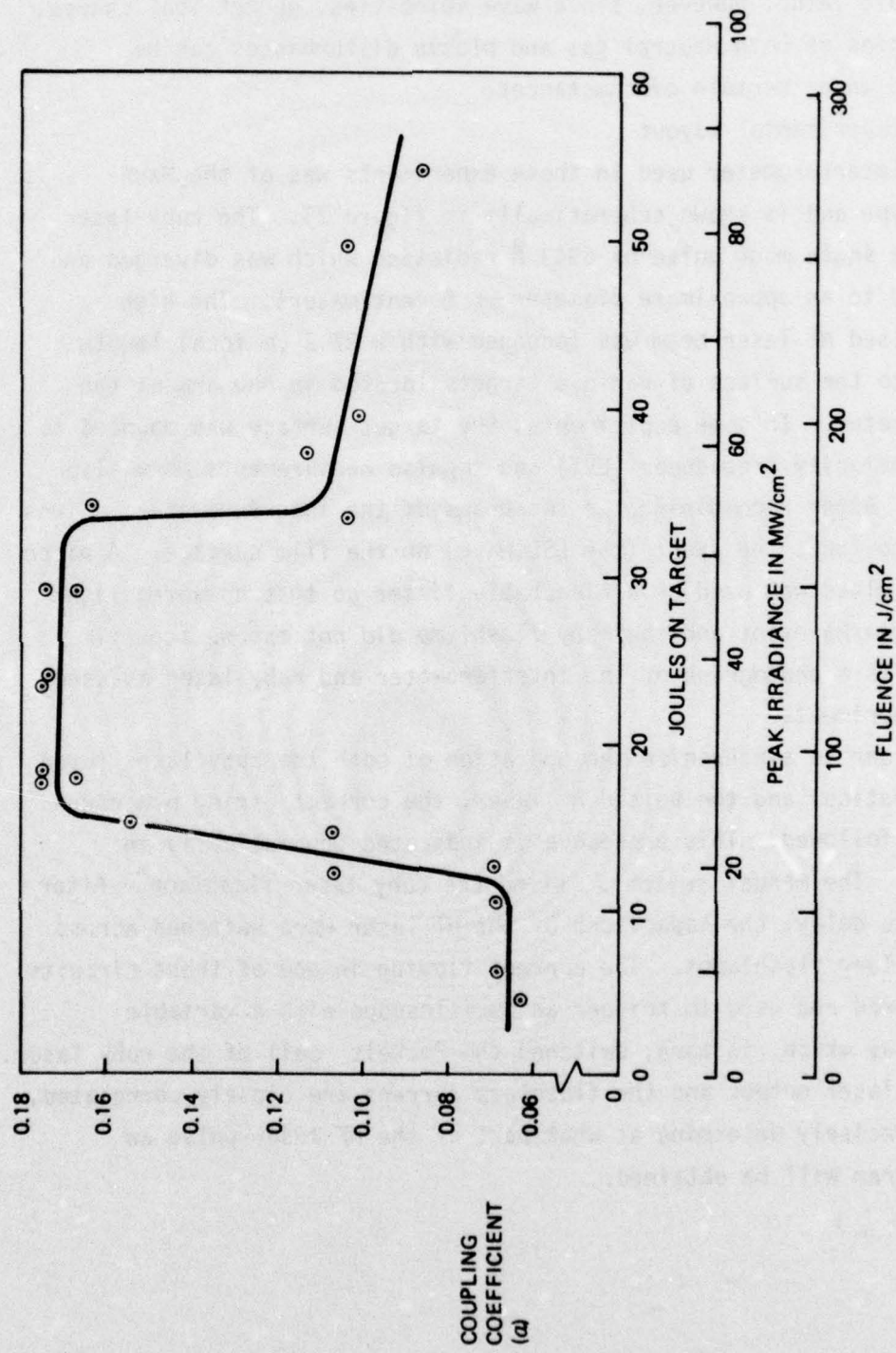


Figure 34. Thermal Coupling Coefficient as a Function of HF Laser Beam Energy for 1.6 cm Diameter Aluminum 6061 Alloy Targets. A New Target Was Used for Each Data Point. The Fluence and Irradiance Scales Assume a Uniform Beam Spot Area of 0.20 cm^2 and a $3.2 \mu \text{ Sec FWHM}$ Laser Pulse.

of the index of refraction of plasmas is different from that of neutrals (or ions); two wavelength interferometry can make a unique determination of densities. The data from single wavelength interferometry do have considerable value, however, since wave velocities, geometrical shapes, and densities of both neutral gas and plasma disturbances can be determined under certain circumstances.

a. Experimental Layout

The interferometer used in these experiments was of the Mach-Zehnder type and is shown schematically in figure 35. The ruby laser produced a single mode pulse of 6943 Å radiation which was diverged and collimated to an approximate diameter of 5 centimeters. The high energy pulsed HF laser beam was focussed with a 37.5 cm focal length mirror onto the surface of various targets located in one arm of the interferometer. In some experiments, the target surface was mounted to a linear velocity transducer (LVT) and impulse measurements were also obtained. After recombining the two beams of the interferometer, a lens was used to focus the event (the LSD wave) on the film surface. A piece of Schott glass was used as a bleachable filter so that unwanted light from the plasma event and the ruby flashlamp did not expose the film. Figure 36 is a photograph of the interferometer and ruby laser as used in the experiments.

In order to synchronize the operation of both the ruby laser (used for diagnostics) and the pulsed HF laser, the correct firing procedure had to be followed. This procedure is indicated schematically in figure 37. The manual switch S fired the ruby laser flashlamp. After a 500 μ sec delay, the capacitors of the HF laser were switched across the 60 cm long flashlamps. The current flowing in one of these circuits was monitored and used to trigger an oscilloscope with a variable output delay which, in turn, switched the Pockels cell of the ruby laser. Since the laser output and the flashlamp current are closely correlated, one can precisely determine at what part of the HF laser pulse an interferogram will be obtained.

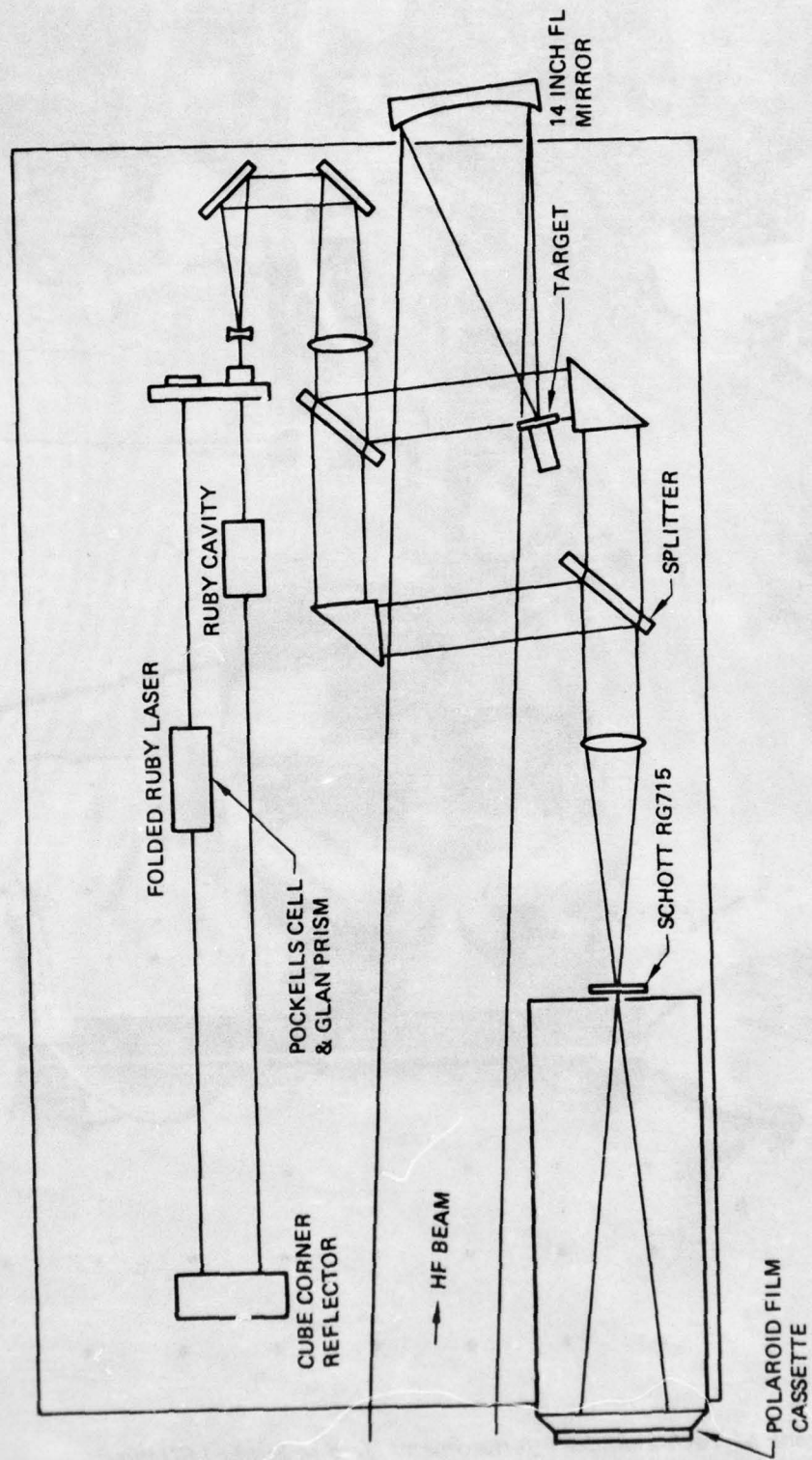


Figure 35 . Schematic Diagram of Ruby Interferometer Set-up

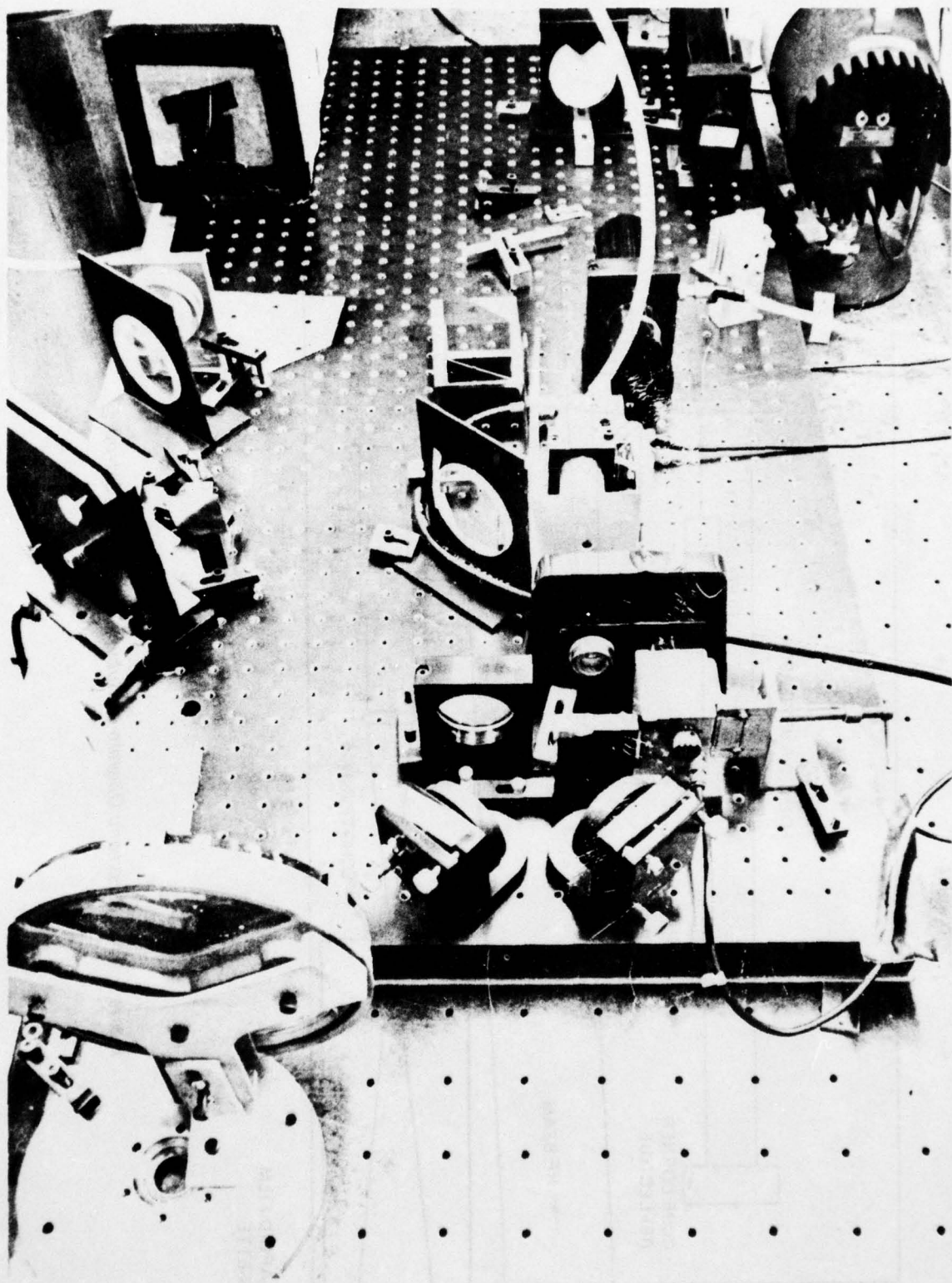


Figure 36. Photograph of Mach-Zehnder Interferometer Used to Study LSD Waves

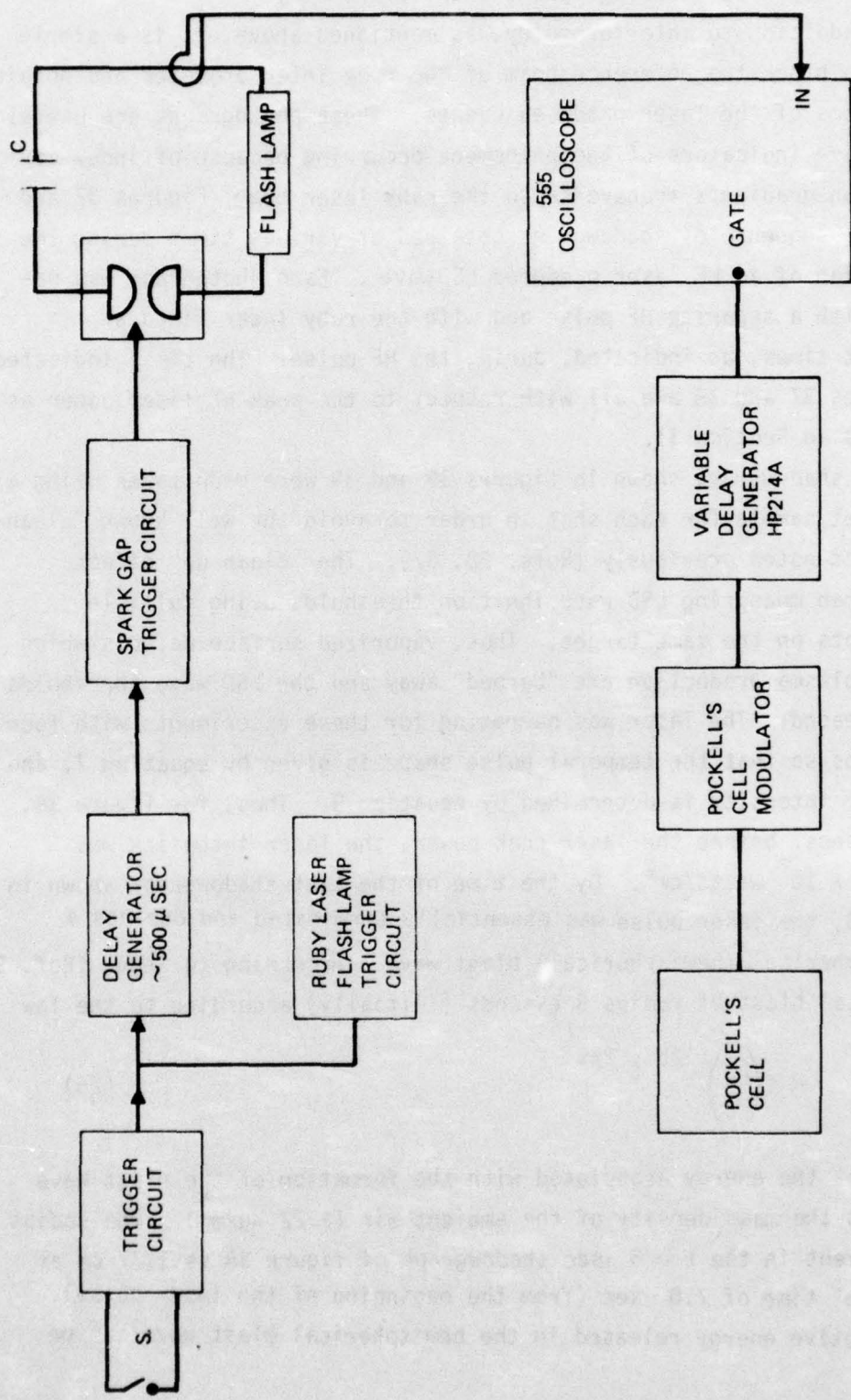


Figure 37. Schematic Diagram of Circuitry Used to Make Interferograms

b. Ruby Laser Shadowgraphs and Interferometry

In addition to interferometry, as mentioned above, it is a simple matter to block the reference beam of the ruby interferometer and obtain shadowgrams of the laser produced events. These photographs are useful qualitative indicators of the phenomena occurring because of index-of-refraction gradients transverse to the ruby laser beam. Figures 37 and 38 show a sequence of shadowgrams obtained at various times during the propagation of an HF laser produced LSDwave. Each photograph was obtained with a separate HF pulse and with the ruby laser fired at different times, as indicated, during the HF pulse. The times indicated in figures 37 and 38 are all with respect to the peak HF laser power as indicated in Section II.

The shadowgrams shown in figures 38 and 39 were each taken using a new target sample for each shot in order to avoid the well known "clean-up" effect noted previously (Refs. 28, 37). The "clean up" effect occurs when measuring LSD wave ignition thresholds using multiple laser shots on the same target. Thus, vaporized surface defects which lead to plasma production are "burned" away and the LSD wave thresholds are increased. The laser was operating for these experiments with four flashlamps so that the temporal pulse shape is given by equation 7, and the laser intensity is determined by equation 9. Thus, for figure 38, at 0.7 μ secs. before the laser peak power, the laser intensity was $q \approx 5.62 \times 10^7$ watts/cm². By the time of the last shadowgraph shown in figure 38, the laser pulse was essentially terminated and one has a nearly spherical (hemispherical) blast wave. According to Sedov (Ref. 38) a spherical blast of radius R expands (initially) according to the law

$$R = \left(\frac{E}{\rho_0} \right)^{1/5} t^{2/5} \quad (26)$$

where E is the energy associated with the formation of the blast wave and ρ_0 is the mass density of the ambient air (1.22 Kg/m^3). The radius of the event in the $t = 5 \mu\text{sec}$ shadowgraph of figure 38 is 1.77 cm at the "true" time of $7.0 \mu\text{sec}$ (from the beginning of the laser pulse). The effective energy released in the hemispherical blast wave can be



$t = 2.0 \mu \text{SEC.}$, $E_{\text{INC}} = 47.9 \text{ JOULES}$

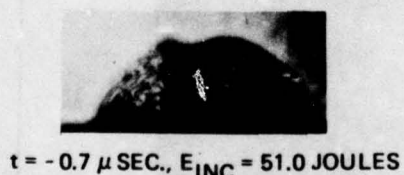


$t = 1 \mu \text{SEC.}$, $E_{\text{INC}} = 46.6 \text{ JOULES}$



$t = 0 \mu \text{SEC.}$, $E_{\text{INC}} = 47.3 \text{ JOULES}$

↑
1 cm
↓



$t = -0.7 \mu \text{SEC.}$, $E_{\text{INC}} = 51.0 \text{ JOULES}$



$t = -1.0 \mu \text{SEC.}$, $E_{\text{INC}} = 46.6 \text{ JOULES}$

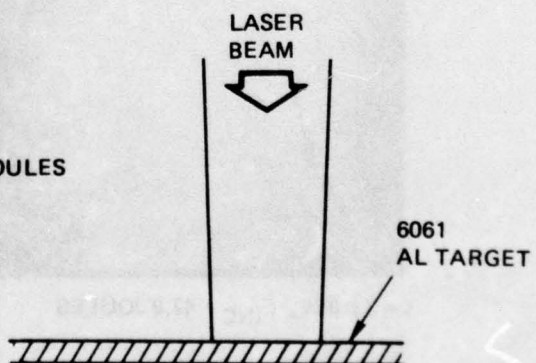
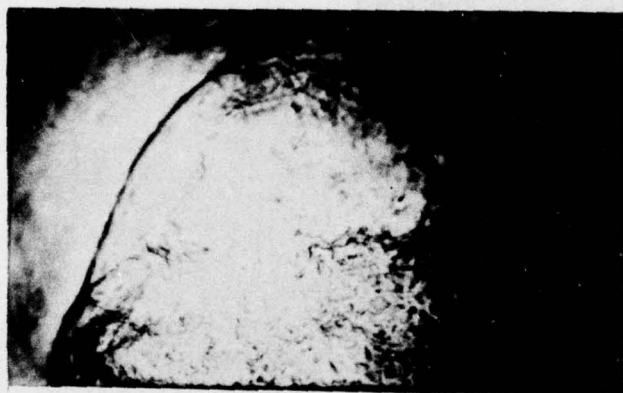


Figure 38. Shadowgrams of LSD Waves Ignited From a Large Target

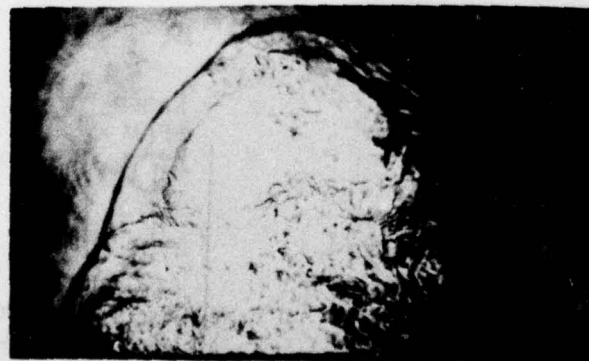


$t = 5 \mu\text{SEC.}$, $E_{\text{INC}} = 46.6 \text{ JOULES}$

↑
1 cm
↓



$t = 4 \mu\text{SEC.}$, $E_{\text{INC}} = 47.9 \text{ JOULES}$



$t = 3 \mu\text{SEC.}$, $E_{\text{INC}} = 47.9 \text{ JOULES}$

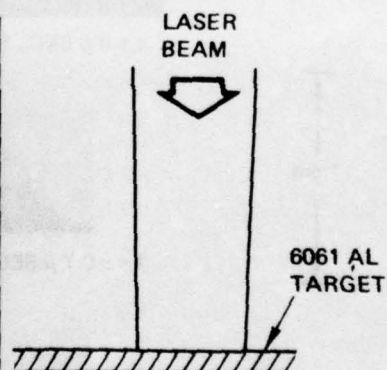


Figure 39. Shadowgrams of LSD Waves

calculated from equation 26 and for this R and t the value of E is 43.3 joules. Since the nearly hemispherical geometry of the blast wave effectively doubles the released energy, the actual blast wave energy is 21.6 joules. This value represents only 0.46 of the initial laser energy incident on the target. The remainder of the laser energy apparently goes into target heating, vaporization, and optical reradiation.

Figures 40 through 42 show a sequence of interferograms taken at various times during the ignition and propagation of laser-supported absorption waves. For each interferogram, a new laser target was used. The interferometer system electronics could be adjusted for variable delays and used to control the time when the interferogram was made. At the earliest times, the LSD waves were moving so rapidly that the approximate 30 nanosecond exposure time of the ruby laser was too long to freeze the fringes. This prevented closely spaced fringes from being resolved. In addition, there is an uncertainty in the magnitude of the fringe shift across the boundary of the blast wave even at the later times shown in this sequence. The shadowgraphs and interferograms shown in figures 38 - 42 were all taken using large flat aluminum alloy (6061) targets and new targets were used for each laser shot.

During the process of making impulse measurements at very high intensities of 2.8 micron radiation, a series of shadowgrams were taken with the linear velocity transducer (LVT) in place and the targets mounted on the LVT. These photographs are shown in figures 43 - 45. In this sequence of shadowgrams only one target was used and, as a consequence, the target "clean-up" phenomenon occurred. The first shadowgram, which was taken 1.2 μ sec before the peak laser power, indicates, by the appearance of two small surface "bubbles", that vaporization is just starting. At a time of 2 μ sec after the peak laser power, one notes that the LSD wave front has moved less than half the distance it would have if fresh targets had been used. This can be seen by comparison with figure 38. This reduced LSD wave magnitude results not only from the increased ignition threshold because of multiple firings on the same spot but also because the target diameter is only about 2.5 times

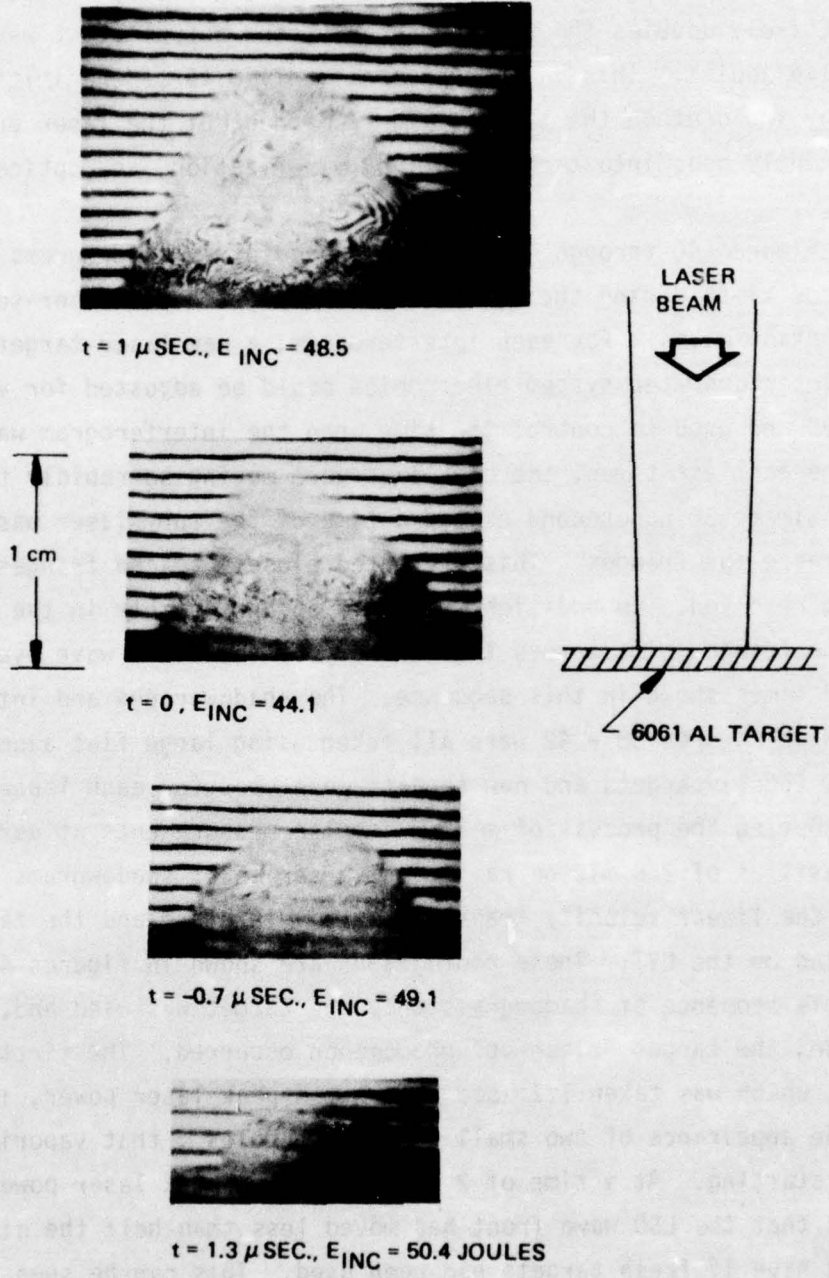
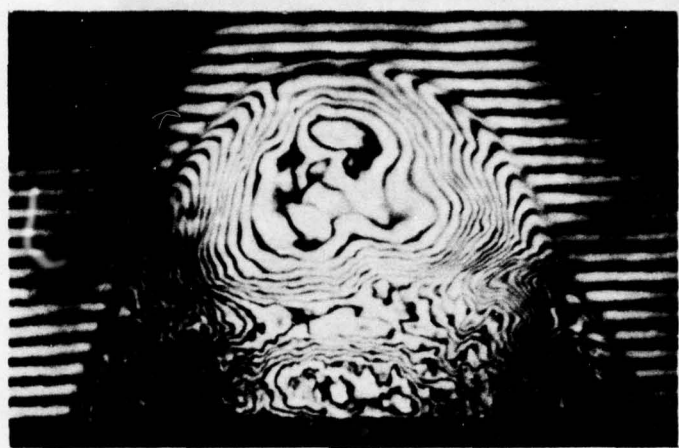
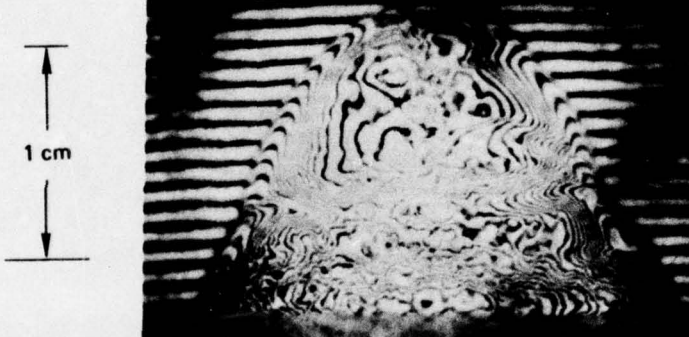


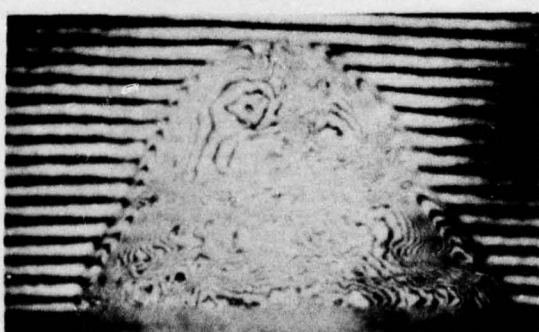
Figure 40. Interferograms of LSD Waves



$t = 4 \mu \text{ SEC.}$, $E_{\text{INC}} = 48.5 \text{ JOULES}$



$t = 3 \mu \text{ SEC.}$, $E_{\text{INC}} = 47.9 \text{ JOULES}$



$t = 2.0 \mu \text{ SEC.}$, $E_{\text{INC}} = 45.4 \text{ JOULES}$

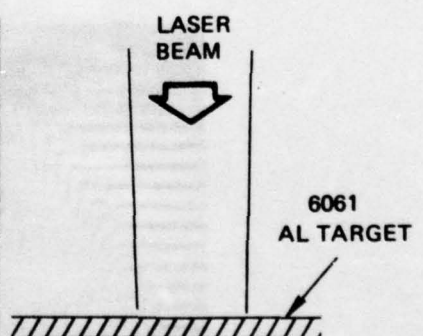
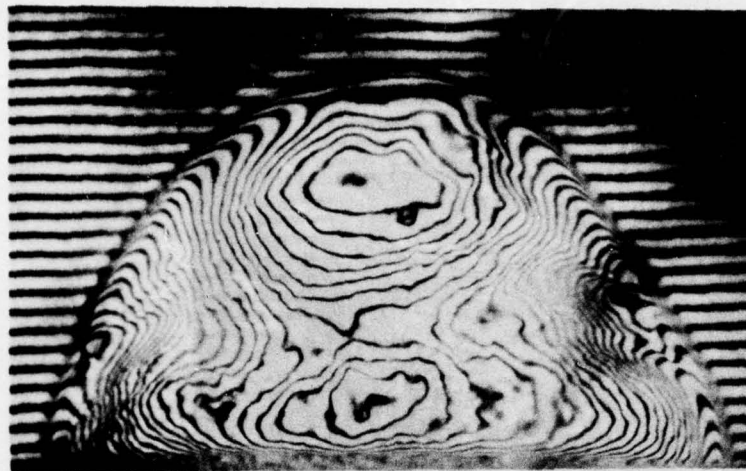
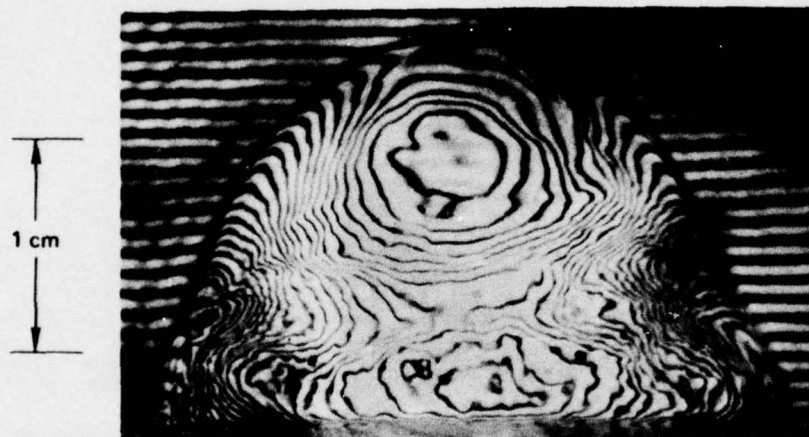


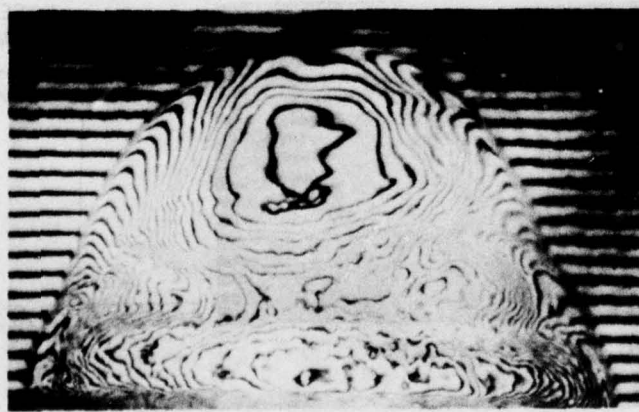
Figure 41 . Interferograms of LSD Waves



$t = 7 \mu\text{SEC.}$, $E_{\text{INC}} = 41.6 \text{ JOULES}$



$t = 6 \mu\text{SEC.}$, $E_{\text{INC}} = 49.1 \text{ JOULES}$



$t = 5 \mu\text{SEC.}$, $E_{\text{INC}} = 47.9 \text{ JOULES}$

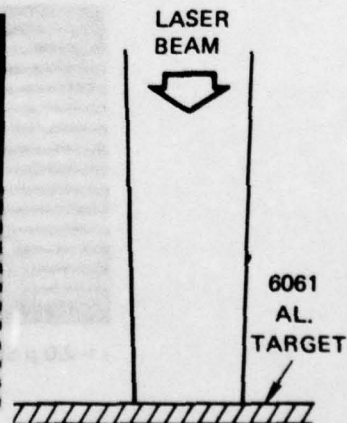
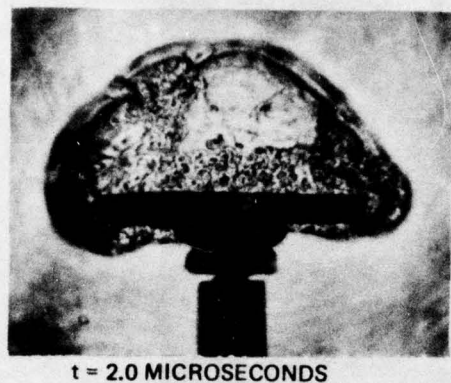


Figure 42. Interferograms of LSD Waves

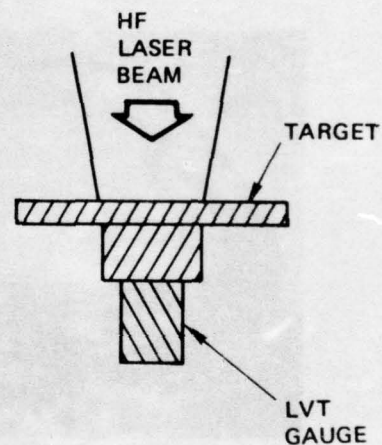


t = 2.0 MICROSECONDS

↑
1 cm
↓



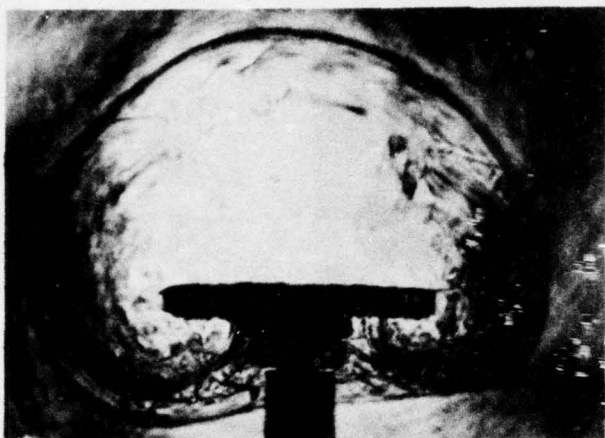
t = 0.6 MICROSECONDS



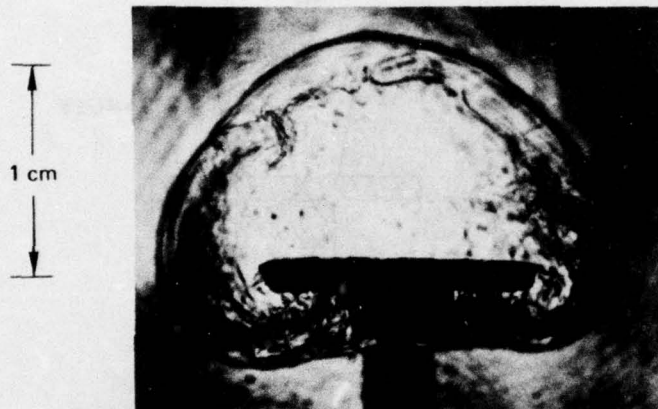
t = - 1.2 MICROSECONDS

Figure 43. Shadowgraphs of Propagating Laser – Supported Detonation Waves.

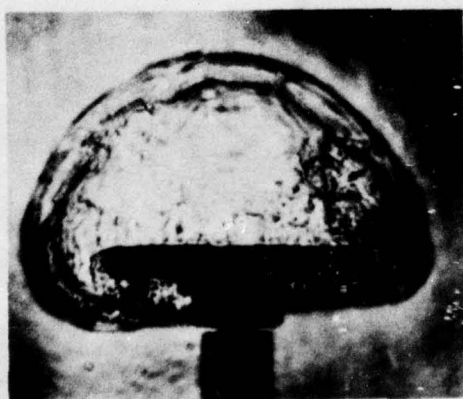
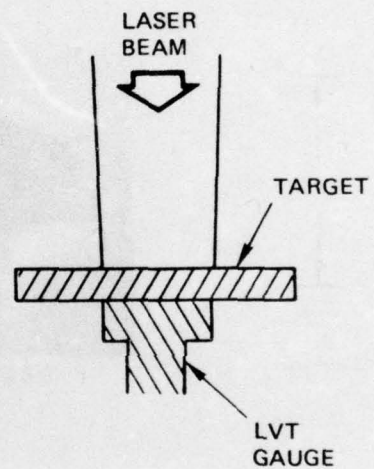
$E_{inc} = 49.8$ Joules Target is 6061 Aluminum



$t = 5.2$ MICROSECONDS, $E_{INC} = 48.5$ JOULES

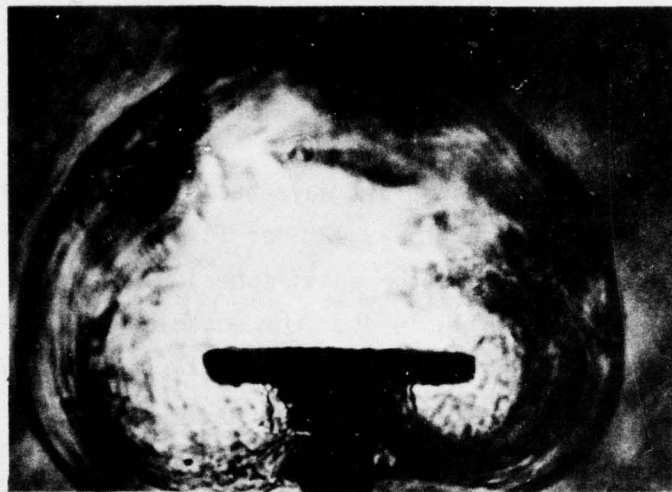


$t = 4$ MICROSECONDS, $E_{INC} = 47.3$ JOULES



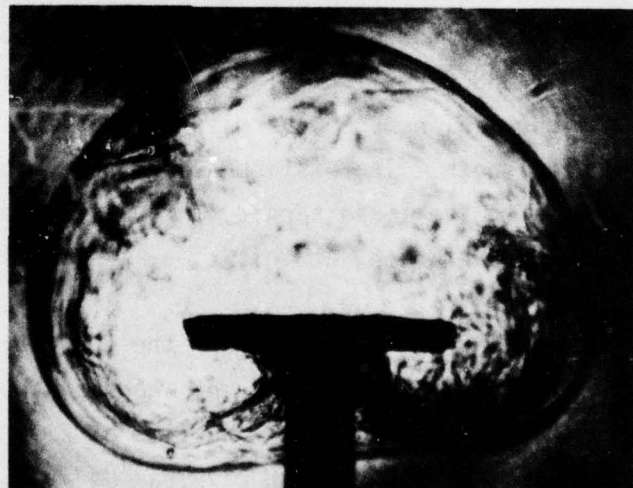
$t = 3$ MICROSECONDS

Figure 44. Shadowgraphs of LSD Waves
Target is 6061 Aluminum



$t = 7.4$ MICROSECONDS, $E_{INC} = 48.1$ JOULES

1 cm



$t = 6.4$ MICROSECONDS, $E_{INC} = 49.1$ JOULES

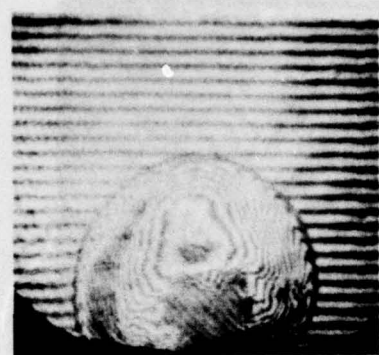
Figure 45. Shadowgraphs of LSD Waves
Target is 6061 Aluminum

the laser spot size. This effect is apparent in figure 43 at 2 μ sec after the peak laser power ($t = 4.02 \mu$ sec after the start of pulse; see equation 7). At this time the laser-produced blast wave has not only reached the edge of the target but has also started to effect the rear surface. Under these conditions, it is evident that the net impulse production by the blast wave over the surface is greatly reduced since the pressure forces are increased on both sides of the target and hence tend to cancel each other.

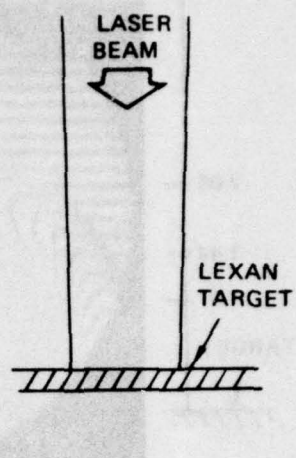
As time progresses the blast wave becomes nearly spherical as can be seen from figure 45 for $t = 9.42 \mu$ sec (or 7.4 μ sec after the peak laser power). At this time the quasi-spherical blast wave radius is approximately 1.47 cm which leads, from equation 26, to the conclusion that only 9.4 joules are contained in the blast wave. This energy represents only 20 percent of the incident laser energy. The exact energy balance between reflection, target heating, and plasma absorption is an unresolved issue at the present time. Because these issues are important for multipulse laser weapons, it is important to do further experimental and theoretical work in this area where target "clean-up" occurs.

Figure 46 shows a comparison between laser-produced events with ablator targets. As was noted in reference 26, it is exceptionally difficult to ignite LSD waves from plexiglas targets with 10.6 micron radiation. In figure 46, no LSD wave was ignited from the plexiglas at 2.8 microns wavelength. The disturbance is the result only of vaporized target material. The lexan target, on the other hand, obviously has produced an LSD wave which, at this time, has developed into a laser-produced blast wave.

Figure 47 shows how the LSD wave near the end of the laser pulse develops into a spherical blast wave event shown by the development as time increases from 5 to 19 μ sec. At the time of 21.0 μ sec, 19 μ sec after the peak laser power, the blast wave radius is 2.59 cm. Equation 26 then indicates that the blast wave energy was 32.2 joules which is 58 percent of the incident laser energy. The blast wave velocity found from equation 26 at 21 μ sec is 4.93×10^4 cm/sec with a corresponding Mach number of 1.43.



$t = 5.1 \mu\text{SEC}$



$t = 5.1 \mu\text{SEC}$

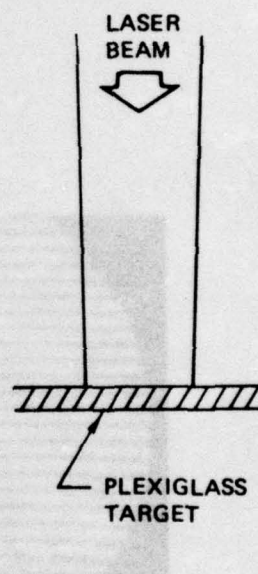


Figure 46. Interferograms of Laser Interaction With Ablators. $E_{\text{inc}} = 48.5$ Joules

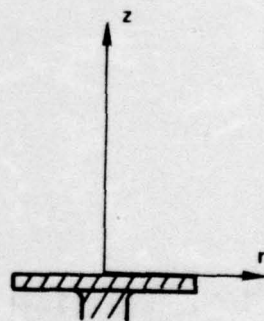
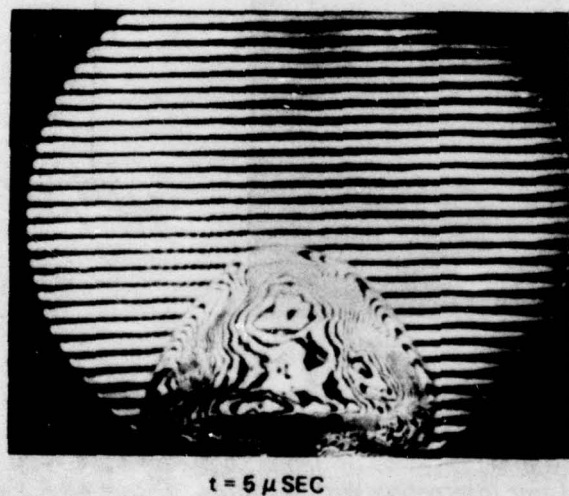
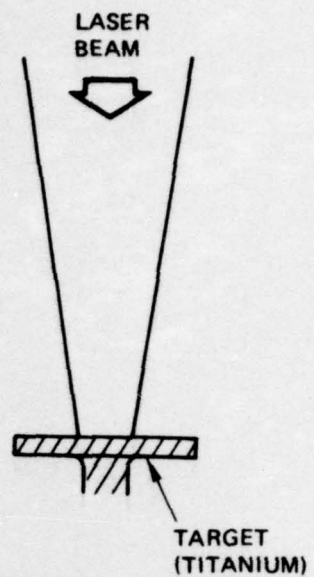
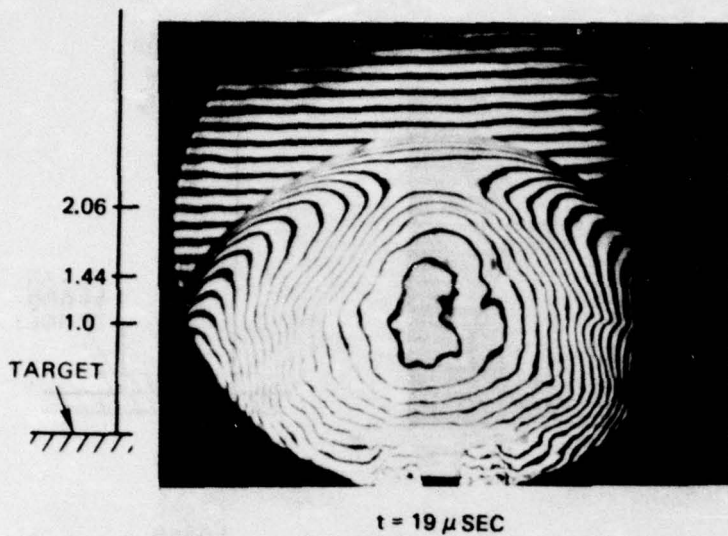


Figure 47. Interferogram of Laser-Produced Blast Wave.

$E_{inc} = 55.4 \text{ Joules}$

From standard shock wave relationships for perfect gases one can determine the gas density discontinuity at the shock front to be (Ref.39).

$$\frac{\rho}{\rho_0} = \frac{(\gamma + 1) M^2}{(\gamma - 1) M^2 + 2} \quad (27)$$

In equation 27, M is the Mach number, γ is the ratio of specific heats, and ρ is the gas density just behind the shock front. For $M = 1.43$ and $\gamma = 1.4$ one obtains

$$\frac{\rho}{\rho_0} = 1.74 \quad (28)$$

c. Interpretation of Interferograms

An analysis of most of the interferograms shown previously has not been accomplished. However, a partial analysis of figure 47 at $t = 21$ microseconds has been completed. Fringe shift data were taken at five axial positions z between 1.44 and 2.06 cm. The fringe shift data as a function of the radial observation distance are given in figure 48.

These data were gathered semiautomatically by projecting an image of the fringe pattern on an electrostatic plate. By "touching" the plate with a pencil the spatial coordinates of the measured fringe were measured and recorded automatically in a mini-computer. At the conclusion of a given traverse across the pattern the collected data are fed into an Abel inversion program (Ref. 37) on the mini-computer and the index of refraction is determined as a function of the radial coordinate. The small negative-going fringe shift near the outer boundary of the blast wave has ambiguities associated with its formation and may be due to refractive effects in the fringe pattern caused by the large density gradient across the shock front.

The index-of-refraction variation as a function of the coordinate r was determined by Abel inversion and is shown in figure 49. The indicated density jump is only about 30% instead of expected 174% as at $T = 19^\circ C$ (Ref. 40). One possible explanation for this large

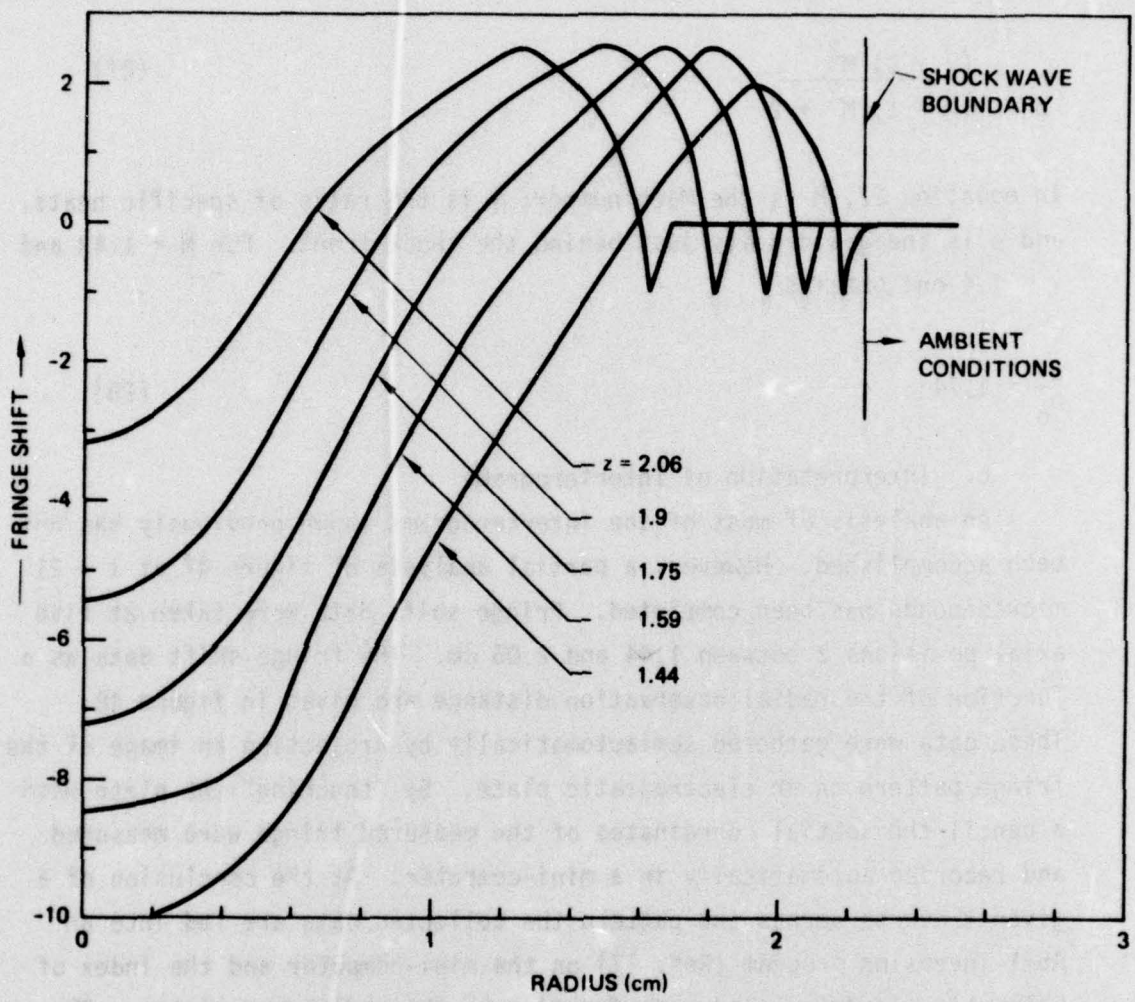


Figure 48. Fringe Shift as a Function of Radius

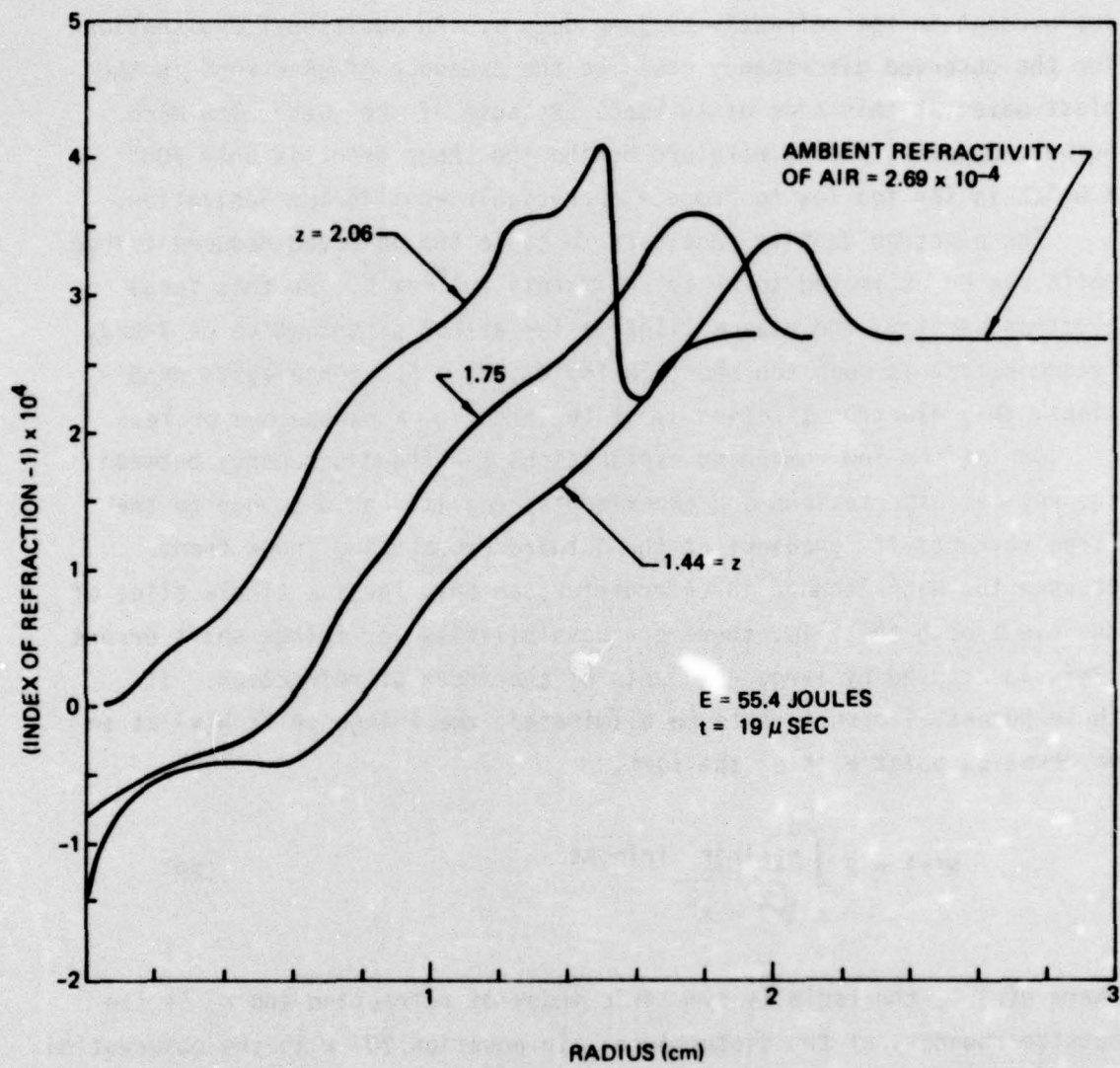


Figure 49. Refractivity of Laser-Produced Blast Wave.

discrepancy could be the initial negative fringe shift indicated in figure 48. To examine this effect a "smoothed" set of fringe shift data was prepared as indicated by figure 50. Unfortunately, very little improvement in the refractivity jump occurs. An additional explanation for the observed discrepancy could be the presence of electrons in the blast waves at this time of 19 μ sec. Because of the rather low Mach number, however, the temperature behind the shock front is only 700° K which is far too low to produce appreciable equilibrium ionization.

The electron density necessary to cause the observed reduced fringe shift can be estimated to be approximately 10^{18} cm^{-3} . At this large electron density, the plasma lifetime for either dissociative or 3-body recombination is much too short (Refs. 41,42). For conceivable conditions, this electron lifetime is of the order of a nanosecond or less.

One of the few remaining explanations for the discrepancy between theoretical expectations and experimental reality could be due to the large refractivity gradient at the outward propagating shock front. Because the Mach-Zehnder interferometer can only focus a single slice of the event onto the film, there are possibilities for fringe shift errors (Ref. 43) caused by large gradients of the index of refraction. If these potential errors could be eliminated, the fringe shift $N(x)$ at an observation point x is of the form,

$$N(x) = 2 \int_{x/\sqrt{r_0^2 - x^2}}^{r_0} \frac{n(r)rdr}{r} \text{ fringes} \quad (29)$$

where $n(r)$ is the radially symmetric index of refraction and r_0 is the outside boundary of the disturbance. In equation 29, x is the observation distance from the axis of symmetry of a radially symmetric event.

The refractivity $n(r)$ near the plasma edge r_0 can always be represented over a limited range of the radial coordinate r by a Taylor series of the form

$$n(r) \approx a + br + cr^2 + \dots \quad (30)$$

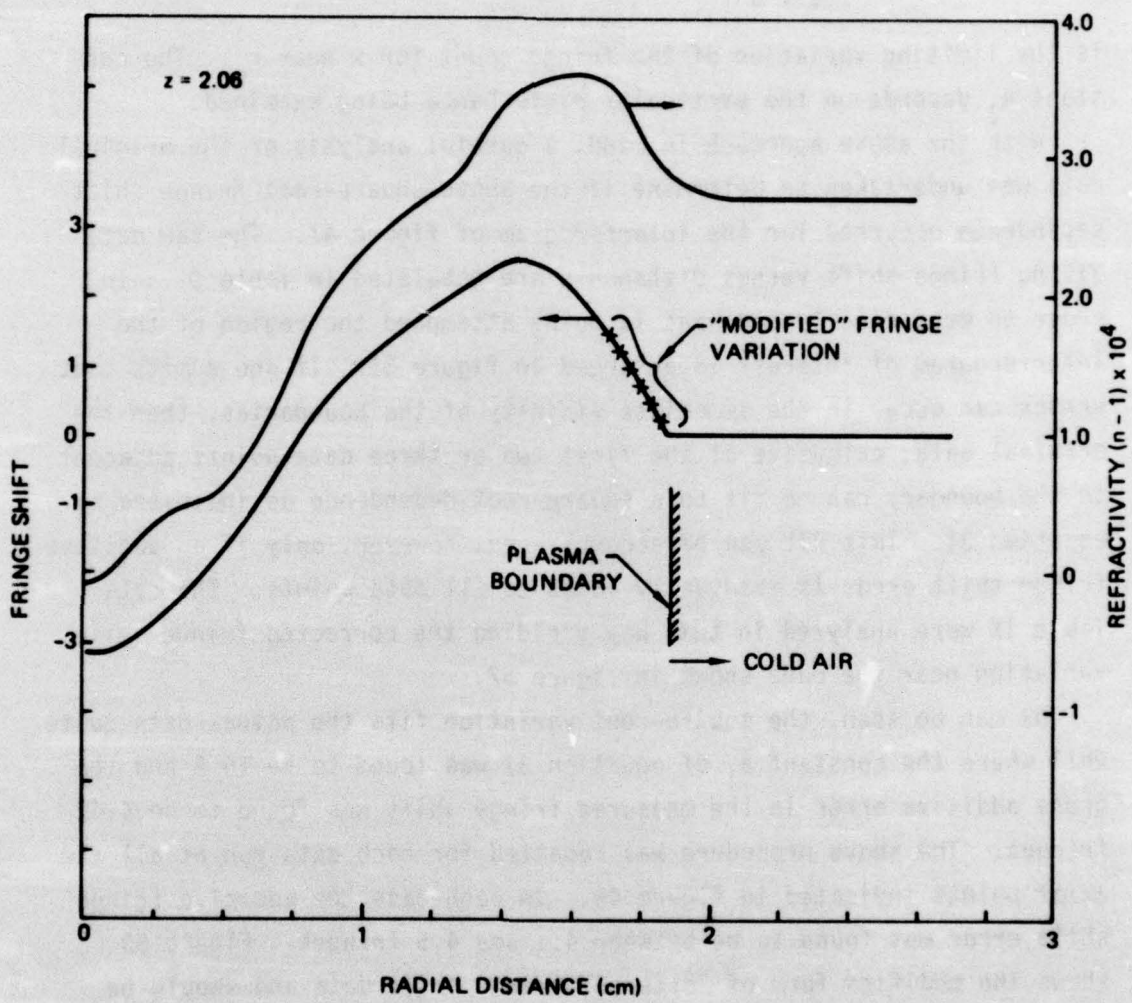


Figure 50. Abel Inversion of Linearly Modified Fringe Data

for $x < r_0$.

In this case, one can determine the limiting variation of $N(x)$ as the observation point x moves from $x = r_0$ to $x < r_0$. One always finds that

$$N(x) = a_1 \sqrt{r_0 - x} \quad (31)$$

is the limiting variation of the fringe count for x near r_0 . The constant a_1 depends on the particular disturbance being examined.

With the above approach in mind, a careful analysis of the original data was undertaken to determine if the above square-root fringe shift dependence occurred for the interferogram of figure 47. The raw data giving fringe shift versus distance x are tabulated in Table 9. In order to more clearly see what is being attempted the region of the interferogram of interest is enlarged in figure 51. If one admits that errors can occur in the immediate vicinity of the boundaries, then the original data, exclusive of the first two or three data points adjacent to the boundary can be fit to a square-root dependence as indicated by equation 31. This fit can be accomplished, however, only if an additive fringe shift error is eventually added to all data points. The data Table IX were analyzed in this way yielding the corrected fringe shift variation near the edge shown in figure 52.

As can be seen, the square-root variation fits the actual data quite well where the constant a_1 of equation 31 was found to be 15.5 and the gross additive error in the measured fringe shift was found to be 4.42 fringes. The above procedure was repeated for each data run at all the axial points indicated in figure 48. In each case the additive fringe shift error was found to be between 4.1 and 4.5 fringes. Figure 53 shows the modified form of "altered" fringe shift data and should be compared to the originally obtained data of Table IX and figure 48.

The Abel inversion of the "raw" data of figure 53 is shown in figure 54. In this case the refractivity jump is close to the expected value of 1.74 given by equation 28. Table 10 compares the actually determined density jumps with this expectation.

TABLE 9

Original Fringe Shift Data as a Function of
Radius. $z = 1.44$ cm.

Fringe Shift	Radius cm.	Fringe Shift	Radius cm.	Fringe Shift	Radius cm.
0	2.238	0.0	1.583	-6.0	0.866
-0.5	2.205	-0.5	1.525	-6.5	0.806
-0.1	2.184	-1.0	1.459	-7.0	0.763
-0.5	2.174	-1.5	1.393	-7.5	0.709
0	2.151	-2.0	1.331	-8.0	0.653
0.5	2.137	-2.5	1.269	-8.5	0.591
1.0	2.114	-3.0	1.201	-9.0	0.510
1.5	2.060	-3.5	1.143	-9.5	0.378
2.0	1.943	-4.0	1.085	-10.0	0.238
1.5	1.791	-4.5	1.012	-10.5	0
1.0	1.717	-5.0	0.961		
0.5	1.647	-5.5	0.917		

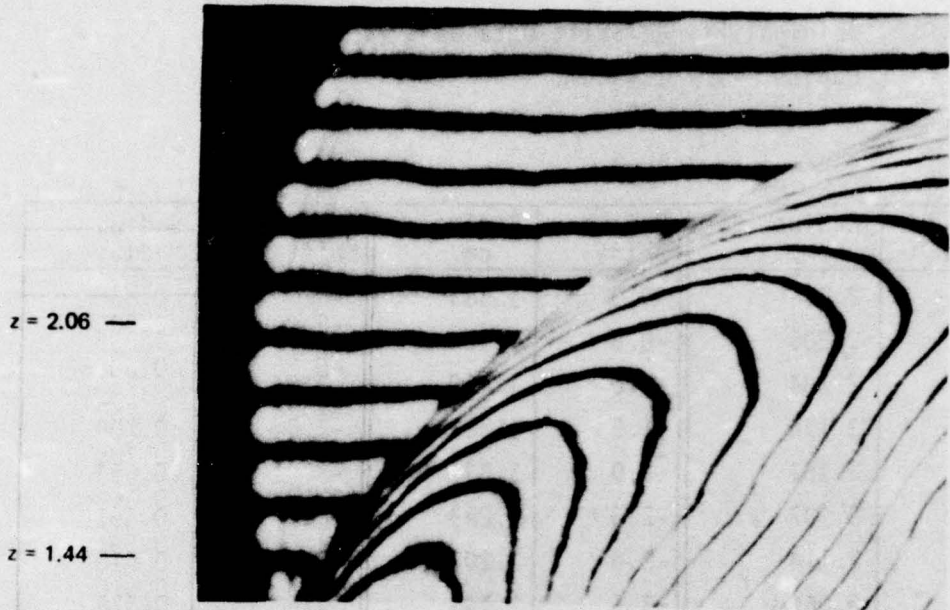


Figure 51. Enlarged View of Boundary Region of Interferogram of Figure 47.

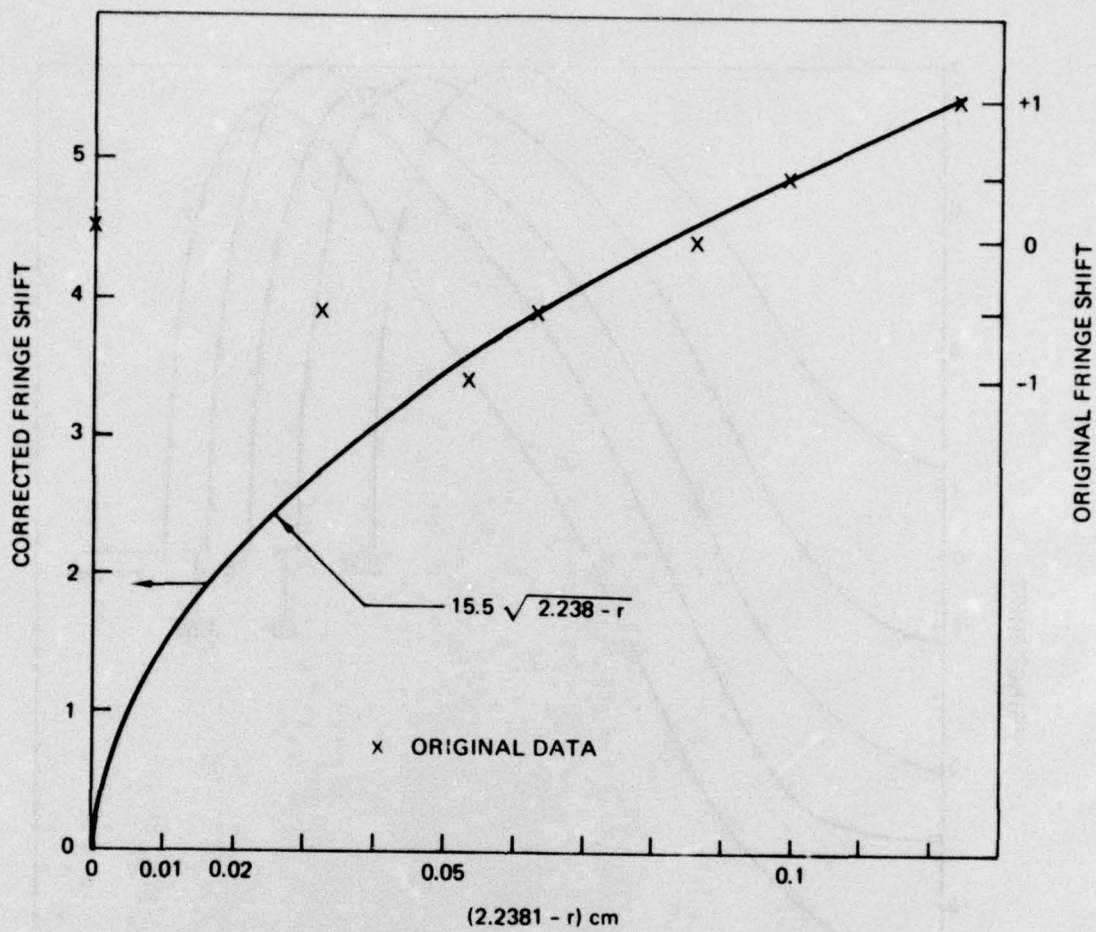


Figure 52. Analytical Fit of Fringe Shift Data to Square Root Dependence. First Two Data Points Excluded. Average Error of Original Data is 4.42 Fringes.

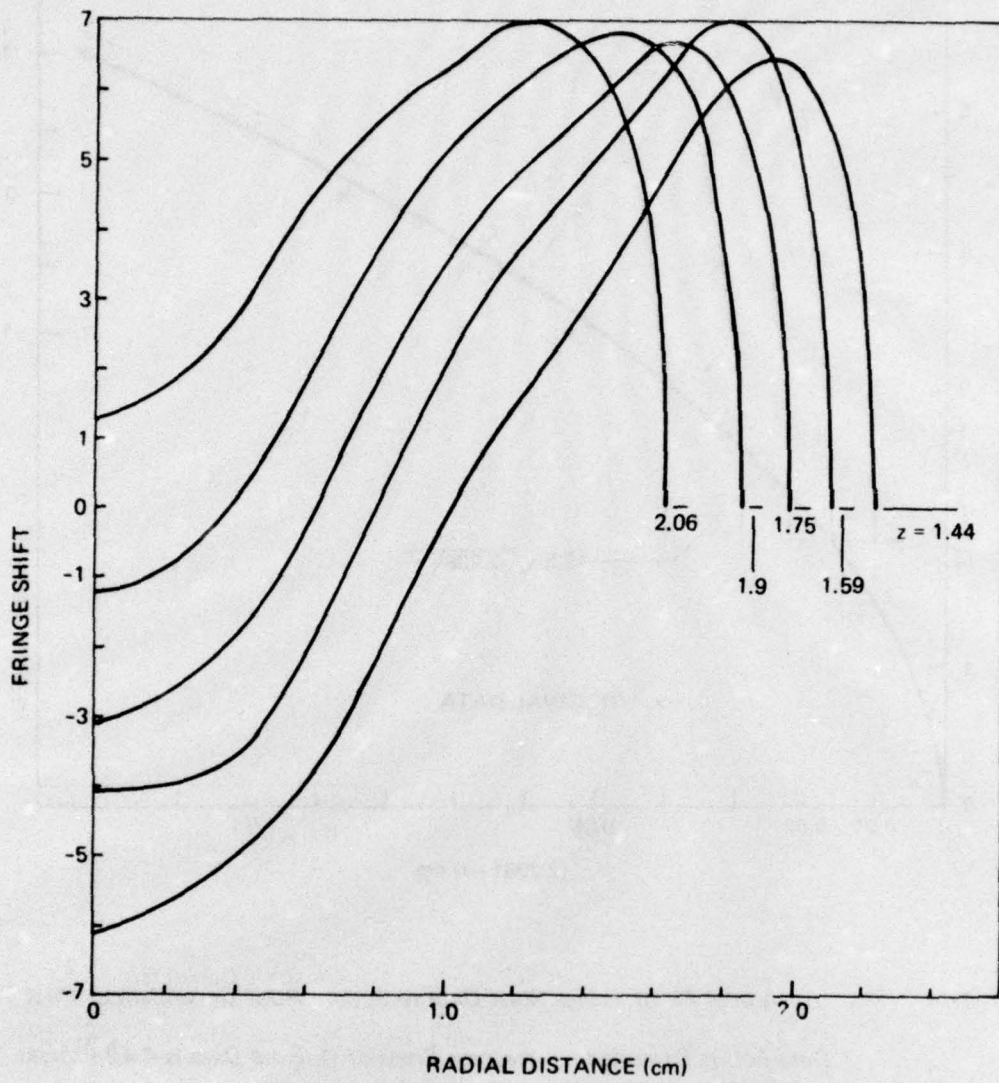


Figure 53. "Square-Root" Modified Fringe Shift Data for HF-LSD Wave

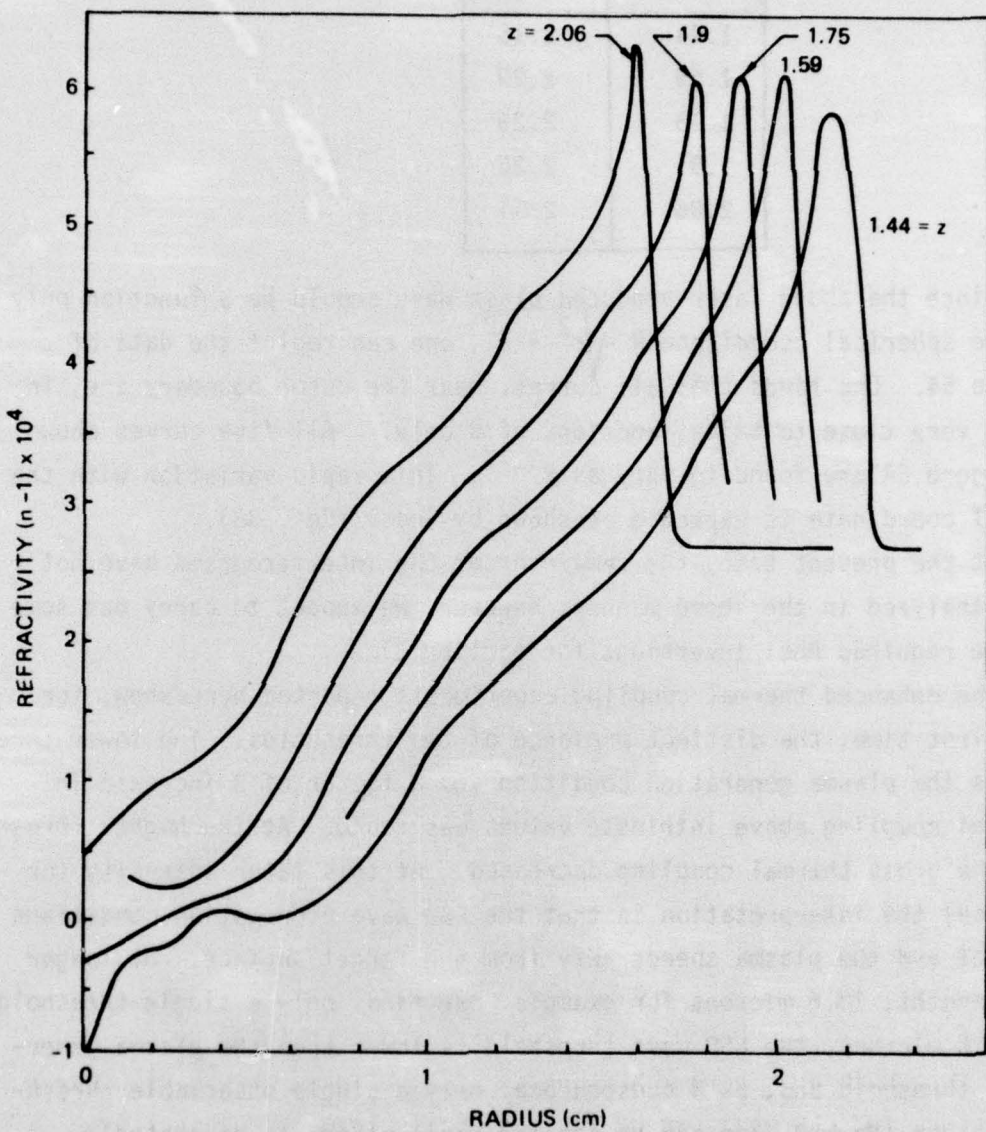


Figure 54 . Computed Density Profiles of Laser Produced Blast Waves

TABLE 10

Z(cm)	$\frac{\rho}{\rho_0}$
1.44	2.16
1.59	2.29
1.75	2.29
1.9	2.26
2.06	2.34

Since the above laser-produced blast wave should be a function only of the spherical coordinate $R = \sqrt{r^2 + z^2}$, one can replot the data of figure 54. One finds that all curves, near the outer boundary are, in fact, very close to being functions of R only. All five curves shown in figure 54 are found to vary as $R^{3.75}$. This rapid variation with the radial coordinate is expected as shown by Sedov (Ref. 38).

At the present time, the remainder of the interferograms have not been analyzed in the above manner; however, we expect to carry out some of the required Abel inversions for earlier times.

The enhanced thermal coupling experiments reported here show, for the first time, the distinct presence of two thresholds. The lower threshold is the plasma generation condition and a factor of 3 increase in thermal coupling above intrinsic values was found. At the higher threshold the gross thermal coupling decreased. At this later intensity (or fluence) the interpretation is that the LSD wave propagation conditions are met and the plasma speeds away from the target surface. At longer wavelengths, 10.6 microns for example, one finds only a single threshold. At 10.6 microns, the LSD wave threshold is lower than the plasma generation threshold and, as a consequence, only a single observable threshold occurs (No LSD wave can be ignited until plasma is generated).

IV SUMMARY

Although the development of the pulsed HF laser described in Section II was not the primary goal in this study, it should be regarded as one of the primary achievements. By the end of 1975, this laser produced over 150 joules of 2.8 micron radiation.

The laser effects studies at this wavelength showed that LSD waves behave according to the detonation theory of Ramsden and Savic (Ref. 21) and Raizer (Ref. 22). In this theory, LSD wave velocities are proportional to the cube root of laser intensity. We have also gathered a small amount of plasma ignition threshold data at 2.8 microns and have concluded that these thresholds are not much different than those for 10.6 microns. These data are not conclusive, however, since only a limited number of experiments were performed. These data were collected using both a transmission technique with a target pinhole and by photographing the plasma luminosity.

The interferometry of these laser-supported absorption waves show how the plasma spreads over the target surface. It is clear that further developments of interferometry techniques would yield additional dividends. This is especially true because of the high velocities of the LSD waves which blur the fringes during the 50 nanosecond exposure times of the ruby laser. In addition, further interpretation of electron density and temperature would be possible if two-wavelength interferometry were employed.

The impulse coupling measurements presented here show that Pirri's LSD wave analysis has a range of validity (Ref. 29). In particular, the impulse was found to increase nearly as the target area. The magnitude of the measured impulse was approximately a factor of 3 less than predicted by Pirri however. This discrepancy could be caused by the real experimental arrangement in which the blast wave pressure disturbance reaches the rear target surface in the experiments reported here.

REFERENCES

1. Whittier, J.S. and Kerber, R. L., "Performance of an HF Chain-Reaction Laser with High Initiation Efficiency," IEEE J. Quantum Electron. QE-10, 844, 1974.
2. Parker, J. V. and Stephens, R. R., "Pulsed HF Chemical Laser with High Electrical Efficiency," Appl. Phys. Lett. 22, 450, 1973.
3. Hofland, R., Lundquist, N. L., Ching, A., and Whittier, J. S., "Electron-Beam-Irradiated Discharges Considered for Initiating High-Pressure Pulsed Chemical Laser," J. Appl. Phys. 45, 2207, 1974.
4. Gerber, R. A., Patterson, E. L., Blair, L.S., and Greiner, N. R., "Multi-Kilojoule HF Laser Using Intense-Electron-Beam Initiation of H₂-F₂ Mixtures," Appl. Phys. Lett. 25, 281, 1974.
5. Chen, H. L., Taylor, R. L., Wilson, J., Lewis, P., and Fyfe, W., "Atmospheric Pressure Pulsed HF Chemical Laser," J. Chem. Phys. 61, 306, 1974.
6. Batovskii, O. M. and Gur'ev, V. I., "Photostimulated Pulsed HF Laser," Sov. J. Quant. Electron. 4, 801, 1974.
7. Nichols, D. B., Wrolstad, K. H., and McClure, J. D., "Time-Resolved Spectroscopy of a Pulsed H₂-F₂ Laser with Well-Defined Initial Conditions," J. Appl. Phys. 45, 5360, 1974.
8. Dolgov-Savel'ev, G. G., Zharov, V.F., Neganov, Y.S. and Chumak, G.M., "Vibrational-Rotational Transitions in an H₂ + F₂ Chemical Laser," Sov. Phys. -JEPT 34, 34, 1972.
9. Greiner, N. R., "Laser Action from Atmospheric-Pressure H₂-F₂ Mixtures Made at 300° K," IEEE J. Quantum Electron. 9, 1123, 1973.
10. Getzinger, R. W., "Stability and Nonexplosive Hydrogen Fluoride Production in Atmospheric-Pressure Hydrogen-Oxygen-Fluorine Mixtures," LA 5659, Los Alamos Scientific Laboratory, Los Alamos, New Mexico, September 1974.
11. Hofland, R., Ching, A., and Lundquist, M.L., "Atmospheric Pressure H₂-F₂ Laser Initiated by Electron-Beam Irradiated Discharge," SAMSO-TR-74-195 (AD 784828), the Aerospace Corporation, El. Segundo, Calif. July 1974.
12. Fortin, R., LaFlamme, A.K., and Rheault, F., "Double-Discharge TEA Laser Beams," Can. J. Phys. 50, 583, 1972.

13. Greiner, N.R., Blair, L.S., and Bird, P.F., "A 0.2-GW Pulsed H₂-F₂ Chemical Laser Initiated by an Electron Beam," IEEE J. Quantum Electron. QE-10, 646, 1974.
14. Aprahamian, R., Wang, J. H.S., Betts, J. A., and Barth, R.W., "Pulsed Electron-Beam-Initiated Chemical Laser Operating on the H₂/F₂ Chain Reaction," Appl. Phys. Lett. 24, 239, 1974.
15. Leeb, W., "Variable Beam Attenuator for the Infrared," Appl. Opt. 13, 17, 1974.
16. Robinson, A.M., and Nohr, M., "Self-Contained Continuously Variable Attenuator for Pulsed CO₂ Laser Radiation," Rev. Sci. Instrum. 45, 1605, 1974.
17. Thorne, J.M., Foree, T.R. and McCall, G.H., "Intensity Filtration of Laser Light," J. Appl. Phys. 45, 3072, 1974.
18. MacPherson, R.W., "Variable Attenuator for REA CO₂ Lasers," Rev. Sci. Instrum. 45, 316, 1974.
19. Braun, W., "A Method to Measure Pulsed Infrared Laser Spectra by Means of Holography," Optical Engineering 14, 208, 1975.
20. McClatchey, R.A. and Selby, J.E.A., "Atmospheric Attenuation of HF and DF Laser Radiation," AFCRL-72-0312, Air Force Cambridge Research Laboratory, Bedford, Mass., May 1972.
21. Ramsden, S.A., and Savic, P., "A Radiative Detonation Model for the Development of a Laser-Induced Spark in Air," Nature 203, 1217, 1964.
22. Raizer, Y.P., "Heating of a Gas by a Powerful Light Pulse," Soviet Physics JETP 21, 1009 (1965).
23. Ready, J.F., Effects of High-Power Laser Radiation, Academic Press, New York, 1971.
24. Walters, C.T., Barnes, R.H., and Beverly, R.W., III., "An Investigation of Mechanisms of Initiation of Laser-Supported Absorption (LSA) Waves," Battelle Columbus Laboratories, Final Report on Contract DAAH01-73-A-0776, 1975.
25. Wei, P.S.P., Hall, R.B., and Maher, W.E., "Study of Laser-Supported Detonation Waves by Time-Resolved Spectroscopy," J. Chem. Phys. 59, 3692, 1973.
26. Hall, R.B., Maher, W.E., and Wei, P.S.P., "An Investigation of Laser-Supported Detonation Waves," Boeing Aerospace Company Final Report on Contract F29601-72-C-0064, AFWL-TR-73-28, 1973.

27. Walters, J.P. "Source Parameters and Excitation in a Spark Discharge," Appl. Spectrosc. 26, 17, 1972.
28. Maher, W.E., Hall, R.B., and Johnson, R.R., "Experimental Study of Ignition and Propagation of Laser-Supported Detonation Waves," J. Appl. Phys. 45, 2138, 1974.
29. Pirri, A.N., "Theory for Momentum Transfer to a Surface with a High-Power Laser," Avco Everett Research Laboratory, Final Report on Contract F04701-72-C-0264, 1973.
30. Kleiman, H., O'Neil, R.W., and Pettingill, L.C., Lincoln Laboratory Optics Research Report 2-1973, 1974.
31. Rudder, R.R., and Augostini, A.L. "Thermal Deposition Experiments with Microsecond Duration CO₂ Laser Radiation, R.R. Rudder, "Further Experimental Observations of the Interaction of Pulsed Five-Micron Radiation with Solid Matter." p.211, Laser Digest-AFWL-TR-75-229, Oct. 1975.
32. Stamm, M.R. and Nielsen, P.E., "Thermal Coupling in Multiply-Pulsed Laser-Target Interactions," Air Force Weapons Laboratory Laser Division Digest, Spring 1974.
33. Jackson, J.P. and Jumper, E.M., "Mechanisms of Enhanced Coupling by a Pulsed Laser," Air Force Weapons Laboratory Laser Division Digest, Summer 1975.
34. Rudder, R.R. and Carlson, R.L., "Material Response to Repetitively Pulsed 10.6 Micron Laser Radiation," Air Force Weapons Laboratory Laser Division Digest, Spring 1974.
35. Gilbert, K.G., and Carlson, R.L. "A Comparative Experimental Study of Material Interaction for Repetitively Pulsed and Continuous Wave CO₂ Lasers," Air Force Weapons Laboratory Report AFWL-TR-72-168, November 1972.
36. Thermophysical Properties of Materials, edited by Toulovkian, Y.S., IFI/Plenum Press, New York, 1970, p. 1015.
37. Maher, W.E. and Hall, R.B., "An Interferometric Investigation of Laser-Supported Absorption Waves," J. Appl. Phys. 45, 761, 1975.
38. Sedov, L.I., Holt, M., and Friedman, M., Similarity and Dimensional Methods in Mechanics, Academic Press, New York, 213, 1959.
39. Landau, L.D. and Lifshitz, E.M., Fluid Mechanics, Pergamon Press, London, 331, 1959.
40. Arecchi, F.T. and Schulz-Dubois, E.O., Laser Handbook, Vol. 2, American Elsevier Publishing Co., New York, 1481, 1972.
41. Hinnov, E., "Measurement of Recombination Rate Coefficient of He⁺⁺," Report Matt-420, Plasma Physics Laboratory, Princeton University, Feb. 1966.

42. Center, R.E., "Electron-ion Recombination Measurements in CO at High Pressure," J. Appl. Phys. 44, 3538, 1973.
43. Medley, S.S., "Laser Interferometry in the Presence of Transverse Plasma Density Gradients," Culham Laboratory Report CLM, 208, 1968.